Investigation of the Flow Field inside a Mass Spectrometer using Particle Image Velocimetry

by
Agapi Davradou

Diploma Thesis

Supervisor: Prof. Dr. Ioannis K. Nikolos

Chania, Greece, 2018

[This page has been intentionally left blank]

TECHNICAL UNIVERSITY OF CRETE
SCHOOL OF PRODUCTION ENGINEERING AND MANAGEMENT

Investigation of the Flow Field inside a Mass Spectrometer using Particle Image Velocimetry

by
Agapi Davradou

Diploma Thesis

Approved on 15/05/2018 by:

…………………………   …………………………   …………………………

Dr. I.K. Nikolos   **Dr. A.I. Delis**   **Dr. M. Konsolakis**
Professor, TUC   Associate Professor, TUC   Associate Professor, TUC

Abstract

The area of low pressure gas dynamics has received significant attention as part of a greater effort to enhance the sensitivity of modern Atmospheric Pressure Ionization Mass Spectrometry (API-MS) systems. In this thesis, an experimental visualization of the under-expanded jet, formed in the fore vacuum region of a mass spectrometer, is realized using the Particle Image Velocimetry (PIV) technique. The investigation of the under-expanded flow field is achieved during a free jet expansion as well as inside Aerolens^{TM}, a novel ion optical device designed to suppress turbulence and laminarize the supersonic flow. Aluminum polydisperse distributions of 10-100 nm, created by a Spark Discharge Source (SDG), are used to seed the flow transferred through a capillary in the low pressure vacuum chamber operated at 20 and 5 mbar respectively. A Scanning Mobility Particle Sizer (SMPS) system was used for the characterization of the spark source. The implementation of a Differential Mobility Analyzer (DMA) for accurate size selection during the PIV experiments was also tested. Fluorescent particles of ~100 nm size, using an Electrospray source, were also employed to test their applicability in such applications. Finally, a Particle Tracking Code available in the literature and developed for data post processing of captured images, was modified to be applied in experimental data obtained at elevated background noise levels, such as those established inside the Aerolens^{TM} or close to the capillary outlet.

Περίληψη (Abstract in Greek)

Ο τομέας της δυναμικής αερίων σε χαμηλή πίεση έχει λάβει σημαντική προσοχή ως μέρος μίας μεγαλύτερης προσπάθειας να ενισχυθεί η ευαισθησία των σύγχρονων συστημάτων φασματομετρίας μάζας με ιονισμό σε ατμοσφαιρική πίεση. Σε αυτή τη διατριβή, η πειραματική απεικόνιση μιας under-expanded δέσμης αερίου, που διαμορφώνεται στην περιοχή του πρώτου θαλάμου κενού ενός φασματομέτρου μάζας, επιτυγχάνεται κάνοντας χρήση της τεχνικής Particle Image Velocimetry (PIV). Η διερεύνηση του under-expanded πεδίου ροής επιτυγχάνεται σε ελεύθερη εκτόξευση της δέσμης αερίου, καθώς και στο εσωτερικό του Aerolens^{TM}, μία καινοτόμα οπτική συσκευή ιόντων, σχεδιασμένη για να καταστέλλει την τύρβη και να στρωματοποιεί την υπερηχητική ροή. Polydisperse κατανομές αργιλίου μεταξύ $10 - 100$ nm παράγονται με τη μέθοδο της ηλεκτρικής εκκένωσης και χρησιμοποιούνται για να εισαχθούν στη ροή που μεταφέρεται μέσω ενός τριχοειδούς σωλήνα στο θάλαμο κενού, που λειτουργεί στα 20 και 5 mbar αντίστοιχα. Ένα σύστημα Scanning Mobility Particle Sizer (SMPS) χρησιμοποιήθηκε για το χαρακτηρισμό της πηγής ηλεκτρικής εκκένωσης και επιπλέον δοκιμάστηκε η χρήση ενός Differential Mobility Analyzer (DMA) για την ακριβή επιλογή μεγέθους σωματιδίων κατά τη διάρκεια των PIV πειραμάτων. Φθορίζοντα σωματίδια μεγέθους ~100 nm από μία πηγή ηλεκτροψεκασμού χρησιμοποιήθηκαν, προκειμένου να ελεγχθεί η δυνατότητα εφαρμογής τους σε τέτοιου είδους πειράματα. Ένας κώδικας εντοπισμού σωματιδίου (Particle Tracking) που είναι διαθέσιμος στη βιβλιογραφία και αναπτύχθηκε για την μετέπειτα επεξεργασία των ληφθέντων εικόνων, τροποποιήθηκε προκειμένου να εφαρμοστεί σε πειραματικά δεδομένα, που λαμβάνονται σε περιβάλλοντα με αυξημένα επίπεδα θορύβου, όπως εκείνα στο εσωτερικό του Aerolens^{TM} ή κοντά στην έξοδο του τριχοειδούς σωλήνα.

Dedicated to my parents…

Acknowledgements

[This page has been intentionally left blank]

Contents

Nomenclature

List of Figures

List of Tables

Chapter 1:

Introduction to Mass Spectrometry

Mass spectrometry (MS) is the best tool today for the identification of unknown compounds, the quantitative determination of known ones and the elucidation of their chemical structure by measuring their mass to charge ratio (m/z).

Every typical mass spectrometer consists of an ion source, mass analyzer and an ion detector (Figure 1.1). In a typical procedure, a sample in solid, liquid or gas state is loaded into the mass spectrometer. Then the sample is ionized inside the ionization source and then the ions are transported to the mass analyzer, where they are subjected to an electric or magnetic field. The deflection of the ions will be proportional to their mass-to-charge ratio (m/z), meaning that ions of the same mass-to-charge ratio will undergo the same deflection. The ions that have been successfully deflected are then driven to the ion detector. The signal from the detector is then processed and plotted by a computer, thus resulting into a mass spectrum of the sample.
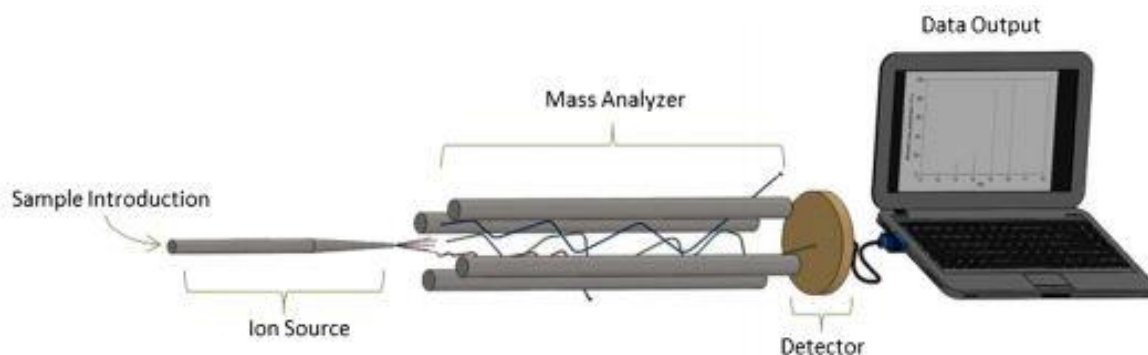
Figure 1.1: Basic components of a mass spectrometer [1].

Mass spectrometers exist for over a century [2] but they hadn't gained much attention till the introduction of the soft ionization techniques, which, in contrast to the initial ones of hard ionization, reduced remarkably the ion fragmentation and led to spectra with fewer peaks.

Nowadays, its extreme sensitivity and its limits of detection have made mass spectrometry a valuable key in many analytical applications. Such applications include for example the field of proteomics, in which MS has become an indispensable tool for the study of proteins and their structural characterization [3], [4]. Mass spectrometry has been widely used also in environmental applications for e.g. identifying pollutants in wastewaters [5], in space exploration [6] as well as in forensic analysis, such as for explosives detection [7], improvement of fingerprint [8] and ink [9] analysis and anti-doping control [10].

Till the end of mid '70s all the conventional ionization sources were integrated inside mass spectrometers and thus operated at high vacuum. However, in 1973 the technique of Atmospheric Pressure Ionization (API) was introduced [11], which led to the development of many atmospheric pressure ionization sources, such as Electrospray Ionization (ESI) [51], Atmospheric Pressure Matrix-Assisted Laser Desorption/Ionization (AP-MALDI) [12], Atmospheric Pressure Photoionization Ionization (APPI) [13] and Atmospheric Pressure Chemical Ionization (APCI). Such sources allow the sample ionization in atmospheric pressure and, then, its transfer to the fore vacuum of the mass spectrometer, thus extending the range of analyses that can be studied by mass spectrometry.

One classification of the mass analyzers, among many others, could be done depending on their transmission of ions. Scanning analyzers, such as sector instruments and quadrupole mass analyzers [14], distribute the ions of different masses separately over time, in contrast to other analyzers, such as the Time Of Flight (TOF) mass analyzer [15], [16], the ion trap [17] and the Orbitrap [18], which transmit all the ions simultaneously.

As Koppenaal et al. has mentioned in his review [19] "in MS, detectors are the "eyes" of the instrument". A basic classification of the detectors can be made depending on their ability to count either a single mass at a time (point ion detectors) thus measuring the ion abundances sequentially or multiple masses (array collectors), measuring them all simultaneously. The most commonly used detectors for decades are the Faraday detector and the Electron Multiplier (EM) detector.

Measurement in mass spectrometry can only be performed for ionized species, while detection is performed at low pressure. Therefore, the ions must be transferred through consecutive vacuum compartments operated at progressively reduced pressures, from 1 bar where ionization takes place, to high vacuum where detection is achieved.

The design of atmospheric pressure interfaces is crucial for achieving low limits of detection and enhance the overall sensitivity of modern instruments. Ions are generated in most cases in nitrogen and sampled into vacuum using skimmers or capillary inlets.

The strong pressure gradients established in the vacuum interfaces are poorly understood, as they involve complex under-expanded flows developed inside ion optical systems. Thus, a better understanding of the gas dynamics at these conditions is crucial not only for the development of mass spectrometers with enhanced sensitivity, but also for the improvement of the existing CFD tools, used to simulate the flow behavior at specific conditions.

The characteristics of Aerolens^{TM}, a novel device meant to suppress the ion diffusion and laminarize the flow [20], [21], [22], [23] are further explored, as it is used to transfer the flow from the first vacuum compartment to the next.

Chapter 2:

Atmospheric Pressure Interfaces in Mass Spectrometry

All mass spectrometers operate at high vacuum (low pressure) in order to avoid the collisions of the sample ions with gas molecules or other contaminating non-sample ions. The non-free movement of the ions could result in a trajectory or charge deviation and in a mass spectrum of increased complexity.

In order for the atmospheric pressure ionization sources to be implemented in MS applications, an atmospheric pressure interface is necessary to sample the ions from atmospheric pressure, at which the ionization takes place, to the high vacuum of the mass analyzer. In a typical configuration, due to the large pressure difference between the ion source and the mass analyzer, intermediate vacuum compartments of gradually reducing pressure are used in-between and ions are transported through skimmers to each one of them, as depicted in Figure 2.1. The skimmers must be wide enough to enhance the ion concentration but small enough to maintain the desirable vacuum conditions.
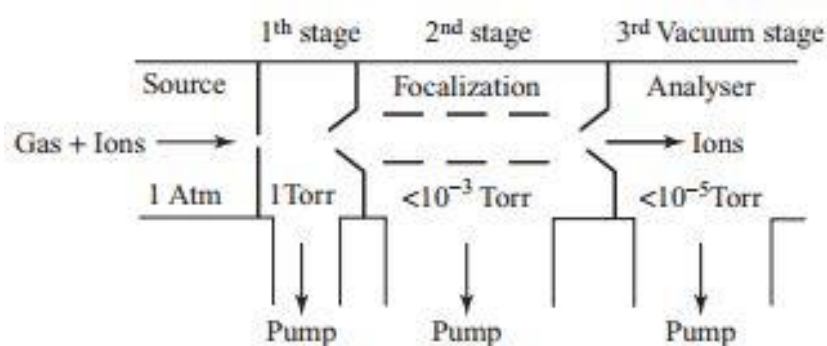
Figure 2.1: A three-stage atmospheric pressure interface [24].

Since the demonstration of the ESI source in 1984 (Figure 2.2), great progress on the efficiency of ion acceptance has been achieved and, thus, these interfaces have evolved considerably. Firstly, the simple skimmer lenses have been replaced by RF ion guides, such

as quadrapoles [14], then followed the use of multipoles of higher order [25], which have been finally replaced by the ion funnel [26] and ultimately with jet confining elements, such as the Aerolens^{TM} [23].
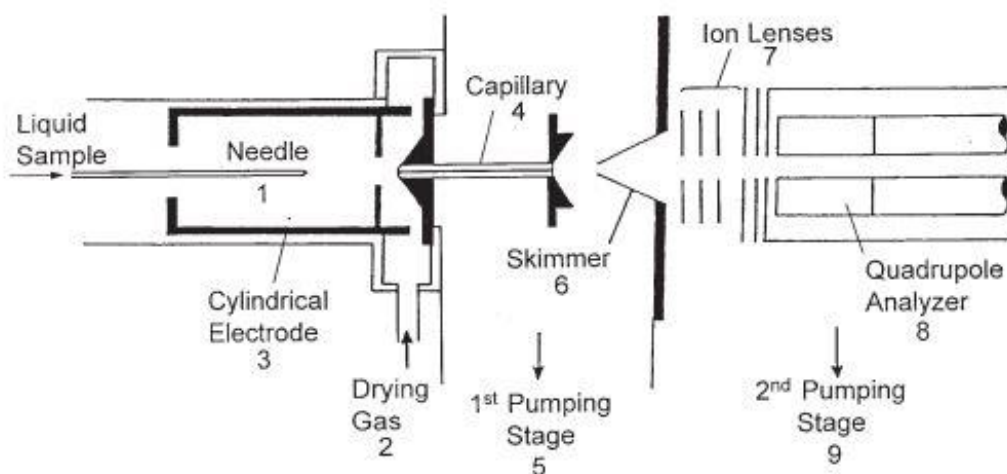
Figure 2.2: Configuration of the second electrospray mass spectrometer built by J.B. Fenn [27].

The amount of usable ion current entering the mass analyzer is enhanced by using ion optical systems, which they focus and transmit ion beams effectively. For the improvement of the design of ion optics there are two main regions that are of a great interest, as they involve complex under-expanded flows.

The first region of interest is the transfer of ions from atmospheric pressure to the pressure of the first vacuum chamber, ranging from 30 mbar to 1 mbar, which in many cases is achieved by using a capillary. The expanding jet is then captured by ion optics in order to focus the ions of the jet and efficiently transfer them to the next vacuum compartment through a small orifice. The ion funnel interface [28] has been effectively used in such intermediate pressures the last past years (Figure 2.3). The ion funnel consists of multiple ring electrodes of decreasing inner diameter to which both DC and RF electric fields are applied, as shown in Figure 2.3.
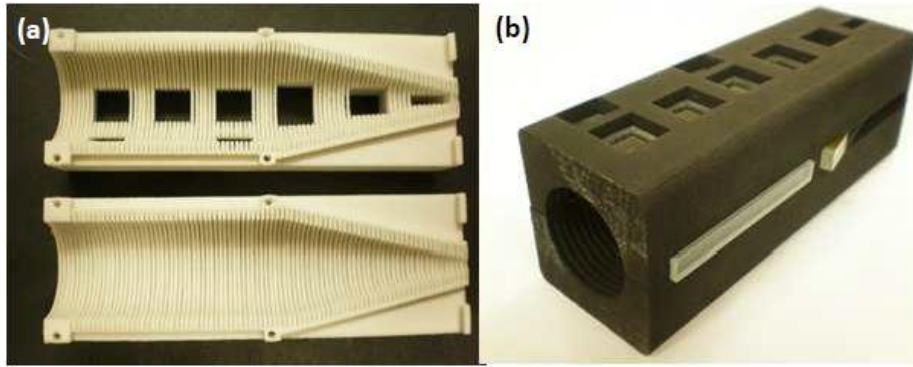
Figure 2.3: 3D printed Ion Funnel Interface [26].

The Aerolens™ optics work also very efficiently at intermediate pressure and are designed to suppress turbulence and control the extent of ion diffusion. Laminarization of the supersonic jet in API interfaces enhances ion transmission and extends the operating pressure range of conventional ion funnel optics. Enlarged inlet openings can be employed, leading to improved sampling efficiency.
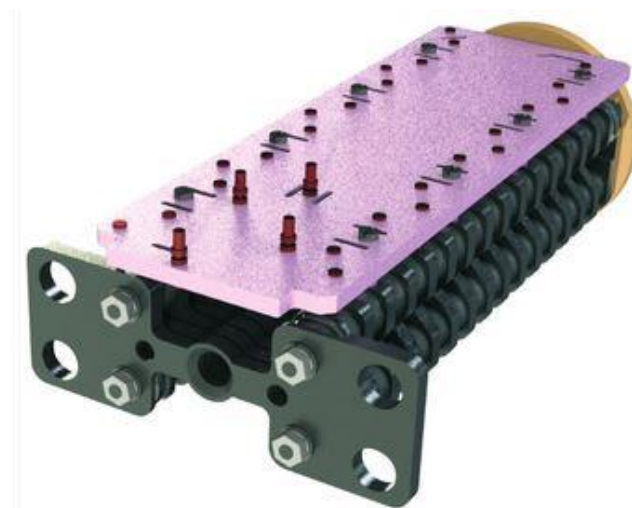
Figure 2.4: Design of Aerolens™. [29].

DC and RF fields are, similarly to the Ion Funnel, applied here to affect the ion motion and provide radial compression (Figure 2.5).
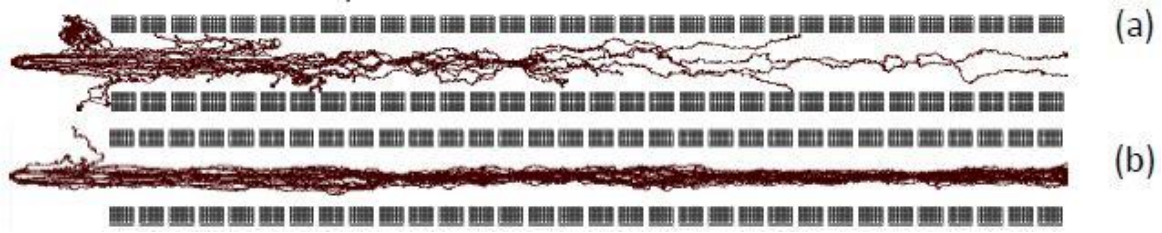
Figure 2.5: Ion trajectories at 20mbar inside Aerolens[TM] (a) in the absence of electrical field and (b) by applying a RF field at 2MHz, 300V_{p-p} [22].

Especially for PTV applications, Aerolens[TM] is not employed in the form of a PCB stack, but a glass channel with equivalent dimensions is used instead, in order to allow for optical access throughout its entire length [20]. The walls of the glass channel achieve the flow laminarization and prevent the ion diffusion as shown in Figure 2.6.
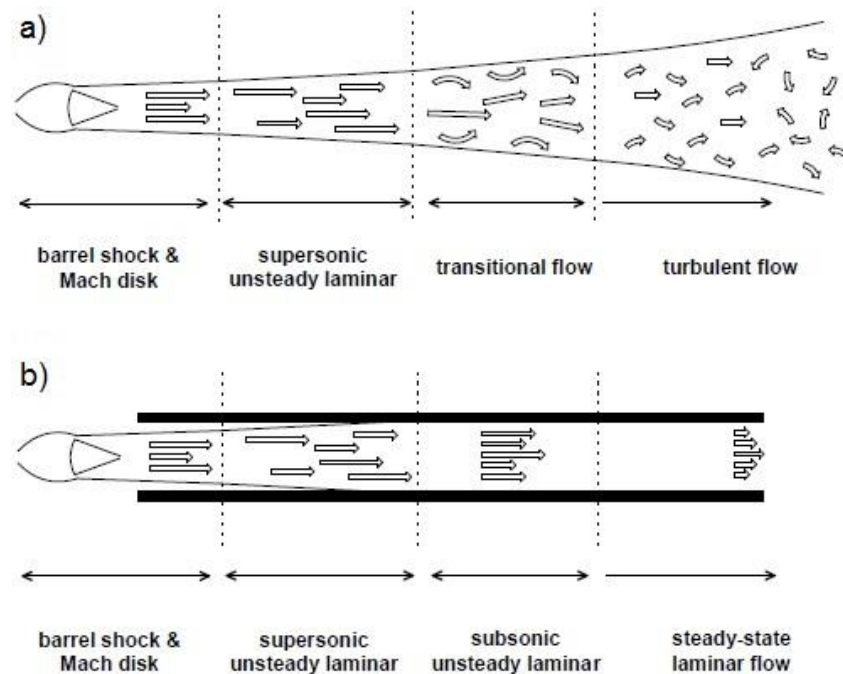
Figure 2.6: Under-expanded Jet. (a) Free Jet Shear Layer vs (b) Aerolens[TM] wall boundary [23].

The second pressure reduction stage is the transfer of ions from the first chamber to the second chamber, with its pressure ranging from 1 mbar to 10^{-2} mbar. At this stage, RF multipole ion guides are used to create a collimated ion beam and transfer it to the next vacuum stage. The name of the ion guide depends on the number of its poles, e.g. quadrapole for 4 poles, hexapole for 6 poles, octupole for 8 poles, etc. The cylindrical (or

ideally hyperbolic) rods are positioned perfectly parallel to each other and a radio frequency (RF) voltage is applied to each opposing pair of rods to prevent the ion diffusion.

2.1 Free Jet Expansion

Under-expanded jets had gained the attention of many famous scientists more than a century ago [30], [31], [32], [33], due to their involvement in many practical applications, such as the exhaust of aircrafts and rockets or the accidental leakage of high pressure storage vessels.

A flow becomes under-expanded when the pressure at the nozzle's or capillary's exit is sufficiently higher than the ambient pressure and a subsequent expansion takes place as a result of the flow's effort to meet the necessary boundary conditions imposed by the background pressure. The ratio of the static pressure on the capillary's or nozzle's exit, P_e, to the ambient pressure in the atmosphere or in a vacuum chamber, P_a is termed Jet Pressure Ratio (JPR) (Figure 2.7):

$$JPR = \frac{P_e}{P_a} \tag{1.1}$$
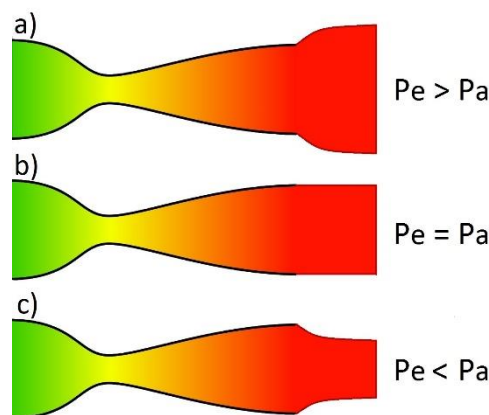
Figure 2.7: Flow behavior in a de Laval Nozzle, also known as converging-diverging Nozzle, which is used in most rocket engines. The nozzle can be a) under-expanded, b) ambient (optimum) or c) over-expanded [34].

The structure of under-expanded jets is very complicated, due to the fact that it combines both supersonic and subsonic regions, as it will be described further downstream. A flow

8

is characterized as supersonic when its speed surpasses the sonic speed, which is defined as the ratio of the translational velocity to the local speed of sound. This ratio is represented by a dimensionless quantity, the Mach number, which was named in honor of Ernst Mach, who, in cooperation with P. Salcher, published the very first photograph of a supersonic bullet in Vienna in 1887 [30] (Figure 2.8).

The Mach number for sonic speeds equals the quantity (M = 1) and is given as:

$$M = \frac{u}{c} \tag{1.2}$$

In the field of fluid dynamics a flow is considered supersonic when M > 1 and when the jet's speed is lower than the sonic speed (M < 1) the flow is called subsonic.
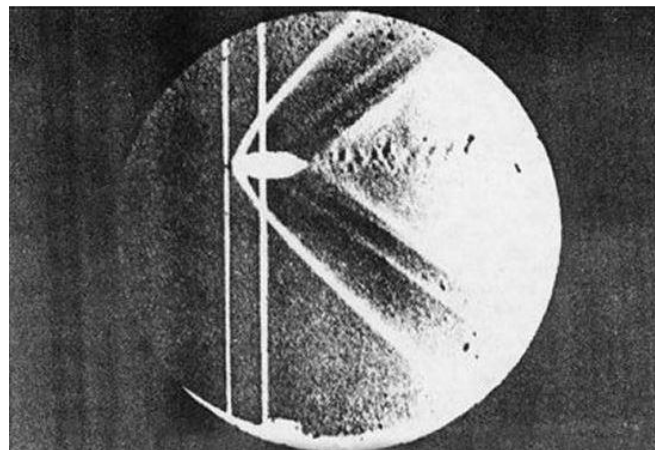
Figure 2.8: Formation of shockwaves by a bullet in supersonic flight [35].

Just after the jet flow exits the aperture a sudden increase in its diameter and a drop in density take place. Expansion waves emanating from the nozzle's lips and produced due to the medium's density reduction constitute the origin of the shock waves and help the flow accelerate to supersonic speeds corresponding to M>1. When a shock wave is reflected over a straight surface two wave configurations are possible: either a regular reflection (RR) or a Mach reflection (MR), depending on the pressure difference. The first one consists of two shock waves, the incident shock and the reflected shock in contrast to the latter, which consists of an additional shock wave, a normal shock. The expansion waves are reflected at the jet's boundary and transformed to compression waves, whose coalescence result in the reduction of jet's cross-sectional area. The accumulation of expansion and compression waves leads to the development of the intercepting (barrel) shock [36].

When the intercepting shock reaches the jet's axis it undergoes reflection resulting in a reflected shock, which can similarly reflect at the jet boundary forming a second generation of compression waves repeating the process.

If the pressure difference between the nozzle exit and the background is high (JPR>3.5 [37], [38]), the intercepting shock undergoes a Mach reflection (MR), yielding to an additional strong shock normal to the direction of the flow, the Mach disk. Just downstream from the Mach disk an area of subsonic flow with a great ignorance for the external conditions is present, called "silent zone" or "zone of silence". A recirculation zone behind the Mach disk had been observed in CFD calculations [39], but this theory was recently ruled out as both experimental [40] and numerical [41] studies proved that no reverse flow exists at that point.

The point where the intercepting shock, Mach disk and reflected shock are met is known as the triple point. As it can also be observed in Figure 2.9(a), the jet's velocity is supersonic inside the barrel shock (M >> 1) and on the shear layer (M > 1) and subsonic just after the Mach disk (M < 1). The high velocity boundaries are high density regions surrounding the core of the jet and carry most of the mass flow around the Mach disk. Krothapalli et al. [42] experimentally investigated the existence of streamwise vortices using shadowgraph photographs. These vortices are developed between the intercepting shock and the jet's boundary, where the flow is supersonic and are strong enough to enhance the entrainment of the external ambient fluid with the jet's fluid.
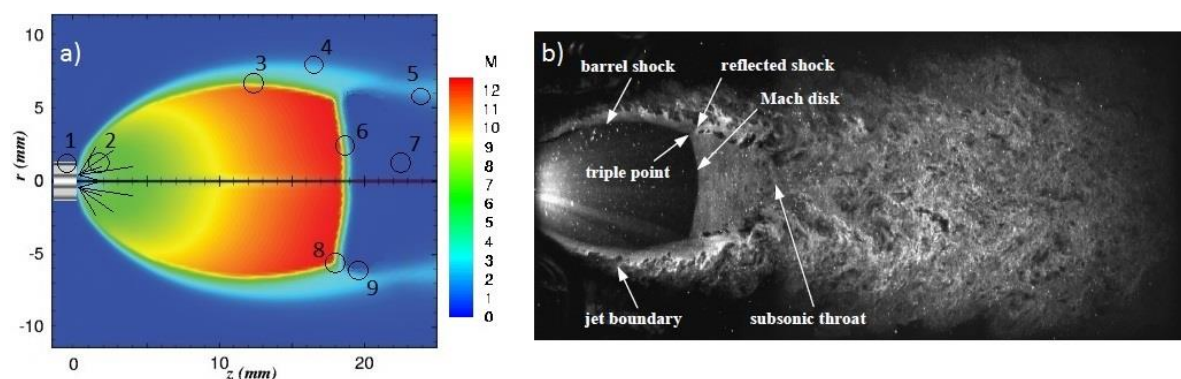
Figure 2.9: Characteristics and of an under-expanded jet under continuum (steady state) conditions. a) 1. Sonic nozzle; 2. Expansion waves; 3. Intercepting (barrel) shock; 4. Outer shear layer (jet's boundary); 5. Inner shear layer; 6. Mach disk; 7. Silent zone; 8. Triple point; 9. Reflected shock; [43]. b) PIV image of a hot-gas jet [44].

The investigation of the characteristics of the under-expanded flow commenced by Love et al. in 1955 who studied theoretically and experimentally axisymmetric jets exhausting from sonic and supersonic nozzles [45], [46], [47], [48] in an attempt to better understand the boundary shape and its curvature. For his tests, which were confined to Schlieren observations, 21 steel nozzles of identical external geometry were constructed, with a rounded smoothly faired throat and a polished interior surface from the start of convergence to the exit. Twenty of the nozzles were conically divergent type with exit angles θ_N of $0°$, $5°$, $10°$, $15°$ and $20°$ and exit Mach numbers M_j of 1.50, 2.00, 2.50 and 3.00 and one nozzle was convergent with an exit Mach number M_j of 1 ($\theta_N = 0°$).

Three governing theories then followed for the approximation of Mach disk's position: Adamson et al. [49] assumed that the Mach disk is located at the point where the static pressure behind the Mach disk equals the ambient pressure. Eastman et al. [50] considered that the theory of Adamson et al. could be applied only for the last shock of the series and located the Mach disk at the position where the static pressure downstream the intercepting shock reaches a minimum. The third approach by Bowyer et al. [51] indicated that the Mach disk is a normal shock at the triple point.

Crist et al. [36] presented approximate expression for the Mach number distribution along the centerline and Mach disk location and diameter based on theory of Adamson et al. [49]. He also indicated that the Mach disk's location is dependent on the pressure ratio and is not determined by the ratio of specific heats, condensation, nozzle lip geometry and absolute pressure level. Addy [52] also provided an empirical formula for the prediction of the Mach disk location formed in a jet exiting from a conically convergent sonic. Finally, it was deduced [53] that both relations should be used depending on the jet pressure ratio.

For low pressure ratios the relations of Addy should be used:

$$\frac{D_{MD}}{D_e} = \begin{cases} 0.36\sqrt{JPR-3.9} & \text{for contoured nozzles} \\ 0.31\sqrt{JPR-5} & \text{for conical nozzles and orifices} \end{cases} \quad (1.3)$$

For higher pressure ratios the relations of Crist would give more accurate results:

$$\frac{D_{MD}}{D_e} \rightarrow 0.4-0.6 \quad , if \ JPR \gg 1 \quad (1.4)$$

The centerline property decay rates in the far-field zone of the under-expanded jet became also a subject of attention. Birch et al. [54] investigated the concentration field in the centerline by conducting experiments with high pressure natural gas exiting from a

11

converging nozzle over the pressure range from 2 to 70 bar. The jet's initial expansion was also taken into account by employing a simple scaling factor, the "pseudo-diameter", assuming that the effective diameter is proportional to the square root of the upstream pressure. Later, he improved this scaling factor based on the conservation of both mass and momentum through the expansion zone, in order to express the velocity decay [55]. Ewan et al. [56] also investigated the velocity decay over a range of exit nozzle diameters, exit pressure ratios and jet gases and he compared his experimental data with compressible analytical models developed for fully expanded jets. Yüceil et al. [57] developed a more thorough scaling analysis of Birch's model [54], which included scaling factors for both the jet's diameter and for the gas parameters, such as density and temperature. They assume an adiabatic initial expansion until the pressure equals the ambient pressure, where at that point (termed location 2) the flow conditions are recalculated.

A series of experiments was conducted at NASA Langley Research Center investigating the behavior of free under-expanded jet flows using planar laser-induced fluorescence (PLIF) [37], [58], [38], [59]. Reynolds number (Re_{exit}) was defined in terms of nozzle exit diameter D_e, density ρ_e, velocity V_e and dynamic viscosity μ_e at the nozzle exit, as given by Eq. (1.5):

$$\text{Re}_{exit} = \frac{\rho_e V_e D_e}{\mu_e} \tag{1.5}$$

By assuming inviscid adiabatic flow and Mach number equal to 1 at the exit, the nozzle exit temperature and velocity can be calculated using equations (1.6), (1.7):

$$T_e = \frac{T_o}{1 + \left(\dfrac{\gamma - 1}{2}\right)} \tag{1.6}$$

$$V_e = \sqrt{\gamma R T_e} \tag{1.7}$$

where T_0 and V_0 are the measured gas temperature and velocity in the plenum, upstream of the nozzle and γ is the ratio of specific heats of the gas ($\gamma = 1.4$ for nitrogen). The dynamic viscosity μ_e is given by Eq. (1.8):

$$\mu_e = \mu_{ref} \left(\frac{T_e}{T_{ref}} \right)^n \tag{1.8}$$

An empirical value of n is given in [60], where $T_{ref} = 273K$ and $\mu_{ref} = 1.663 \cdot 10^{-5}$ Pa·s. The realization that the distance to turbulence is not only a function of Reynolds number, but of JPR as well, made them use the scaling laws of Yüceil et al. [57] to create a rescaled Reynolds number that includes the JPR effect. The expression is presented in Eq. (1.9):

$$unit\ \mathrm{Re}_2 = \frac{\rho_2 v_2}{\mu_2} = \frac{\mathrm{Re}_{exit}}{De} \cdot \frac{2\gamma \left(\gamma M_e^2 JPR + JPR - 1 \right) \left(2\gamma^2 M_e^2 JPR^2 \right)^n}{\left[2\gamma M_e^2 JPR \left(\gamma + JPR - 1 \right) - \left(\gamma - 1 \right) \left(JPR - 1 \right)^2 \right]^{n+1}} \tag{1.9}$$

where M_e is the actual Mach number at the nozzle exit and $n = 0.67$ is given empirically for nitrogen in [60].

The effect of JPR on the jet flow was investigated and a different behavior was observed for JPR values lower than 3.5. In Figure 2.10 the incident shock, the Mach disk and the shear layer are clearly represented in the first three PLIF images, where the JPR is higher. These characteristics are slightly visible on the fourth picture with a JPR value of 5, where a diamond pattern starts exhibiting instead. In the last image no Mach disk or barrel shock is present anymore and the flow is consisted of the diamond pattern. It is also visible that the higher the value of JPR is, the bigger the Mach disk's geometry will be.
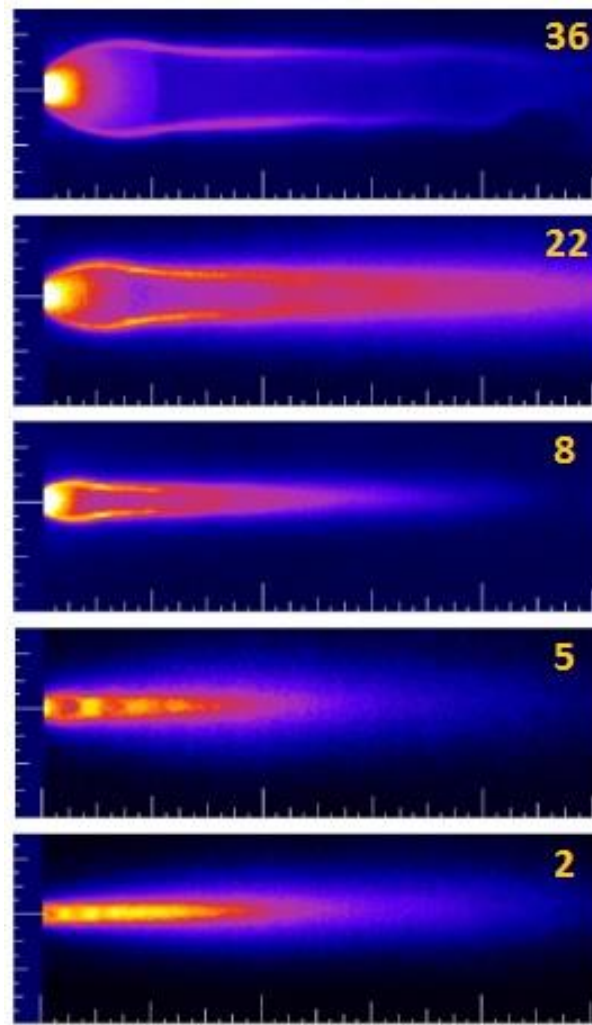
Figure 2.10: Under-expanded jet for JPR values of 36, 22, 8, 5 and 2 respectively [37].

With the use of standard deviation maps the shock intersections, shear layers and locations of local jet maximum diameter were identified as regions of instability. As Kothropalli et al. [42] had also previously indicated, the instabilities first develop in the shear layer and extend till the jet's core.

The main structures of an under-expanded jet at low and high JPRs for sonic and supersonic nozzles respectively are presented in Figure 2.11. A capillary is a sonic nozzle, as the flow can reach M=1 but it can never exceed Mach=1 at its exit. The de Laval nozzle however showed previously in Figure 2.7 is a supersonic nozzle, as the flow can exceed the sonic speed, leading to the formation of a longer barrel shock in contrast to sonic nozzles.

	Sonic Nozzle	Supersonic Nozzle
Low JPR	D_e, x_m	D_e, x_m
High JPR	D_e, D_m, x_m	D_e, D_m, x_m
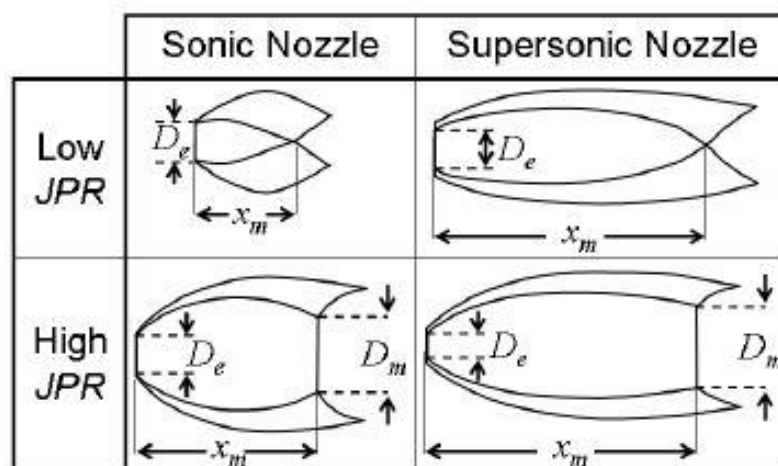
Figure 2.11: Main structures of the barrel shock for an under-expanded jet [59].

2.2 Generation of Nanoparticles

One of the most popular soft ionization techniques used for solid and liquid samples in atmospheric pressure is the Electrospray Ionization (ESI). The idea of ESI was introduced by Malcolm Dole et al. in 1968 [61] but John B. Fenn et al. was the one who managed to publish the first persuasive experimental results in 1984 [62] that lead to the "Electrospray Revolution" [63] and the wide use of ESI in many mass spectrometric applications for over 30 years.

ESI is a technique that applies electrical energy to transfer the ions from solution to gaseous phase. The compound of interest, which in the PIV applications is the tracer particles, is contained within a volatile solvent and is dispersed in aerosol form via electrospray. A capillary is used to lead the aerosol into the first vacuum stage. In many cases the capillary is heated to promote the evaporation (also known as desolvation) of the solvent. In the first vacuum chamber the solvent desolvates from the droplets enhancing progressively their charge till their Rayleigh limit is reached, where at that point the droplets dissociate and the charged ions are liberated.
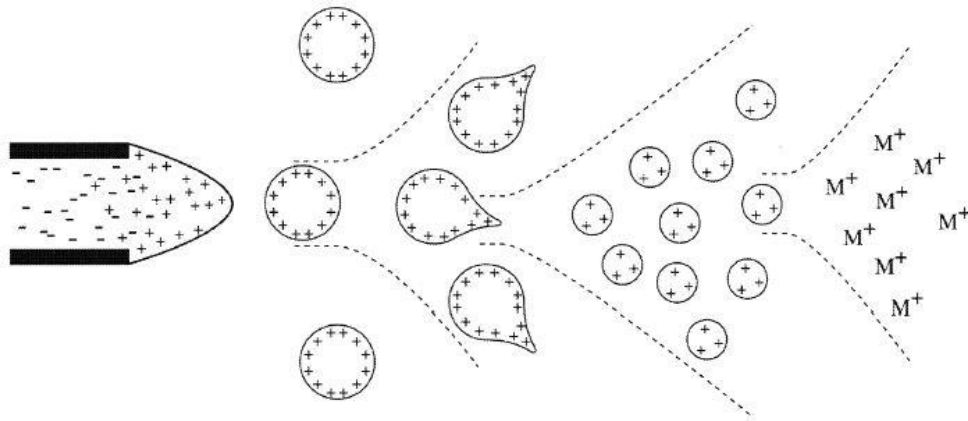
Figure 2.12: Schematic of the ESI function. The solution is presented inside the capillary, then in its aerosol form, when reaching the Rayleigh limit, after decomposition and when ions are freed [64].

Another very popular technique is the generation of nanoparticles using a Spark Discharge Source (SDG). The SDG was introduced in 1979 by H. Altgeld et al. [65] for the continuous production of aerosol, which the 99.9% of it possessed a diameter <1 μm. Later, in 1988 was used by S. Schwyn et al. for the creation of monodisperse carbon aerosol [66]. This gas-phase synthesis seems to be very advantageous when it comes to PIV experiments, as it contributes in particles with high surface purity that lacks liquid solvents.

The design of a spark discharge generator is quite simple. Two elongated electrodes that can be of the same or different material, are kept at a distance of a few mm apart and are connected in parallel with a capacitor. A constant gas flow between the two electrodes is established. As long as the capacitor is being charged by a high voltage power supply, the voltage between the two electrodes is increased until the breakdown voltage is reached. At that moment, a spark discharges across the gap and it evaporates electrode material. This gas-phase material, consisted of ions, neutrals and electrons, is then subjected to rapid cooling by the gas flow downstream leading to coagulation and creation of aerosol. In Figure 2.13 a schematic of a spark discharge ionization source is represented.
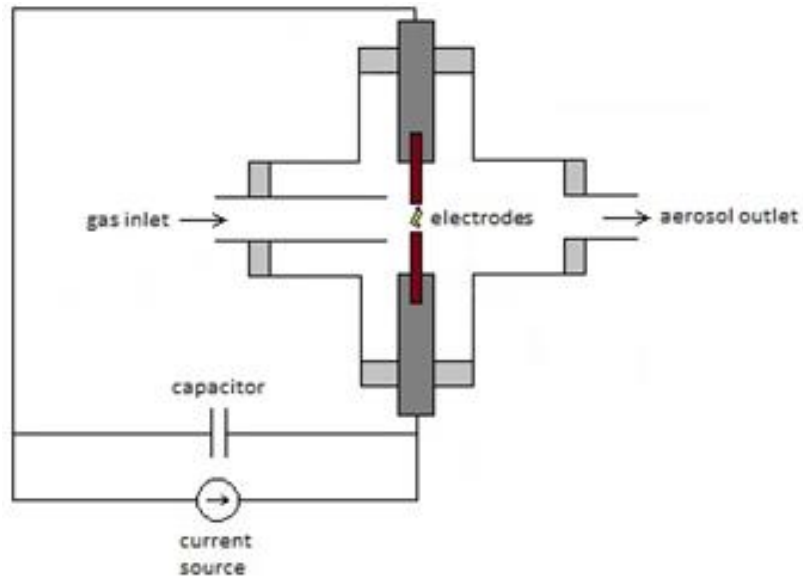
Figure 2.13: The basic components of a Spark Discharge Source [66].

The particle size and concentration can be investigated using a Scanning Mobility Particle Sizer (SMPS) system. A SMPS system is an optical sizing technique for the measurement of aerosol size distribution and concentration, which couples a Differential Mobility Analyzer (DMA) and a Condensation Particle Counter (CPC).

A DMA separates charged particles according to their electrical mobility. This is achieved by first passing the aerosol through the aerosol charge neutralizer, in order the particles to obtain a known charge distribution and then the flow enters the measurement area. There, a fast stream of gas containing ions flows perpendicular to an electric field and therefore ions of different size undergo a different deflection. More specifically, a DMA consists of a center rod, to which a high voltage is applied, an outer grounded tube and the aerosol sample is drawn in-between (Figure 2.14). The voltage difference between the central rod and the outer tube generates an electric field deflecting the charged particles either towards the central rod or the outer tube, depending on their polarity. For a given voltage, the higher electrical mobility a particle has, the sooner will impact the central rod and thus only particles of a certain electrical mobility can pass through the slit at the bottom of the DMA and exit [67].
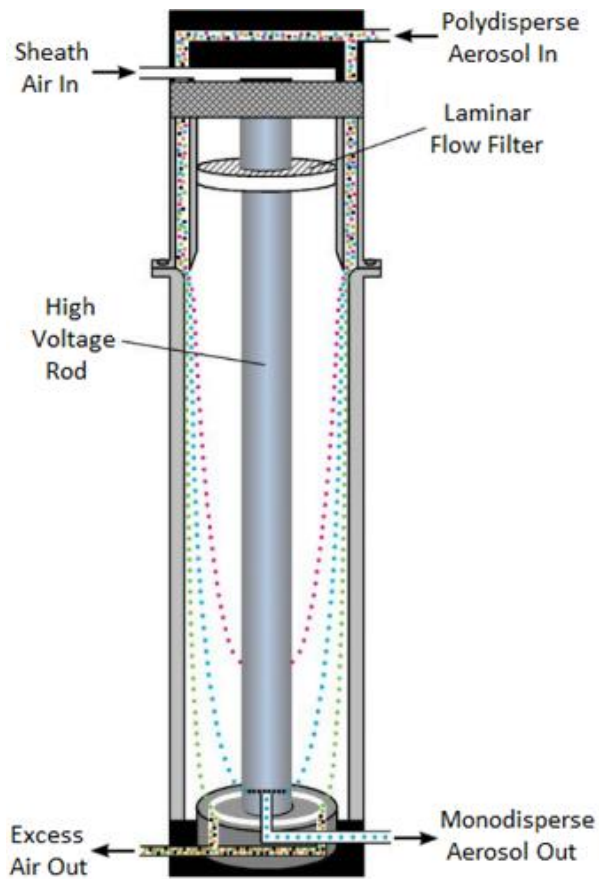
Figure 2.14: Schematic of a Differential Mobility Analyzer [67].

A CPC is an aerosol particle counter, which enlarges the particles by condensation and counters them by an optical light scattering detector. More specifically, a CPC consists of a block of porous material, which is in contact with the working fluid (mostly butanol or water), ensuring that high concentration of vapor is present when heated. The sample passes through the heated block and then enters the conditioner, where the vapor condenses on the particles, thus growing them on size (Figure 2.15). The CPC is equipped with a light source and a photodetector to collect the scattered light, thus detecting and counting the enlarged particles [67].
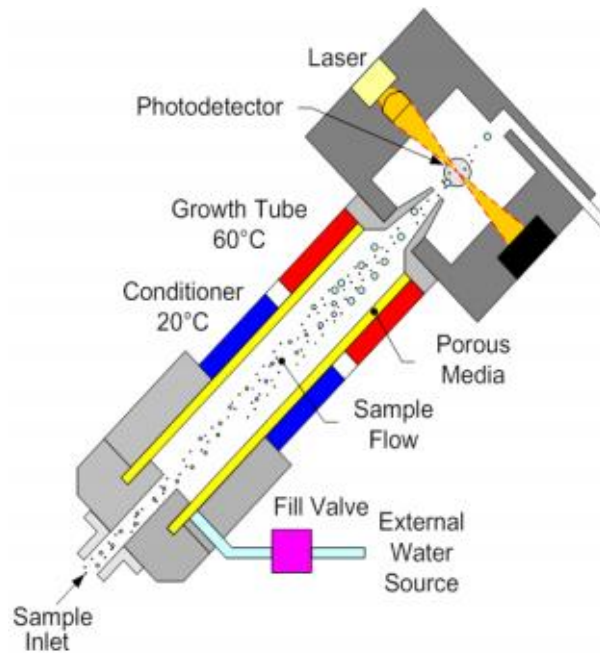
Figure 2.15: Schematic of a Condensation Particle Counter [67].

In a SMPS system, the voltage of the DMA changes progressively, therefore allowing particles of the corresponding electrical mobility to exit, which are then counted by the CPC and generating in this way a size distribution.

Chapter 3:

Particle Image Velocimetry (PIV)

Particle Image Velocimetry (PIV) is a non-intrusive technique for the visualization of the flow field, providing an instantaneous velocity vector map. The flow is seeded with particles (termed tracer particles), which illuminate when irradiated by the laser and thus the flow is visualized. A camera is located at 90° to the laser sheet taking multiple images of the illuminated flow, which are then transferred to a computer for further processing. Ludwig Prandtl was one of the first who used particles for a more thorough investigation of the flow field in the beginning of the 20th century, as he suspended fine scales of micaceous iron ore in the flow [68]. Other popular similar to PIV techniques, such as Laser Doppler Velocimetry (LDV) and hot-wire anemometry preceded, but PIV prevailed due to its ability to produce 2D and 3D vector fields. Depending on the concentration of the tracer particles the technique is distinguished in Particle Image Velocimetry (PIV) mentioned already, Particle Tracking Velocimetry (PTV) and Laser Speckle Velocimetry (LSV) [69].
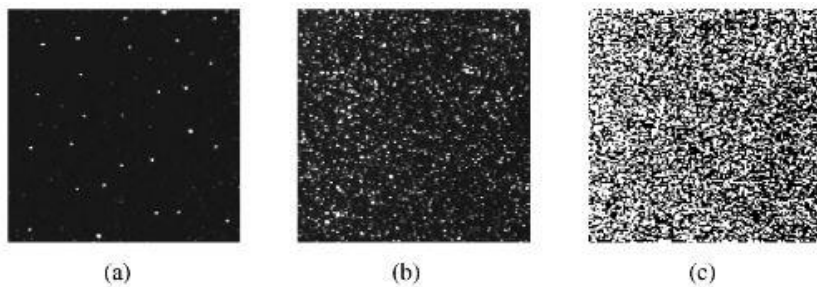
Figure 3.1: Image frames with (a) low particle concentration (PTV), (b) medium particle concentration (PIV) and (c) high particle concentration (LSV) [69].

In PIV the distinction of individual particles in an image is possible, but their tracking in another image is in most cases not feasible. In PTV due to the low particle concentration, the identification of an individual particle and its tracking in another image is relatively easy. Finally, in LSV the particle concentration is much higher and thus the distinguishing of individual particles in any image is very difficult.

The PIV system consists mainly of 4 basic components: the lasers, the camera, the synchronizer and a computer.

Frequency doubled Nd: YAG lasers are commonly used in PIV applications, typically at 532 nm wavelength. The green light emitted at this wavelength passes through consecutive lenses, creating a thin light sheet that irradiates the tracer particles suspended in the flow. The light scattered by the tracer particles is captured by a photographic lens located perpendicular to the laser sheet. Nowadays CCD or CMOS camera sensors are mostly used, as they are capable of capturing two frames with a few hundred ns difference between the frames. The timing between each laser pulse and the corresponding frame of the CCD camera is accurately controlled by the synchronizer. The time interval between the two consecutive laser pulses and therefore the two frames is depending on the fluid's velocity. The captured images are directly transferred to the computer, offering a real time or later time analysis.
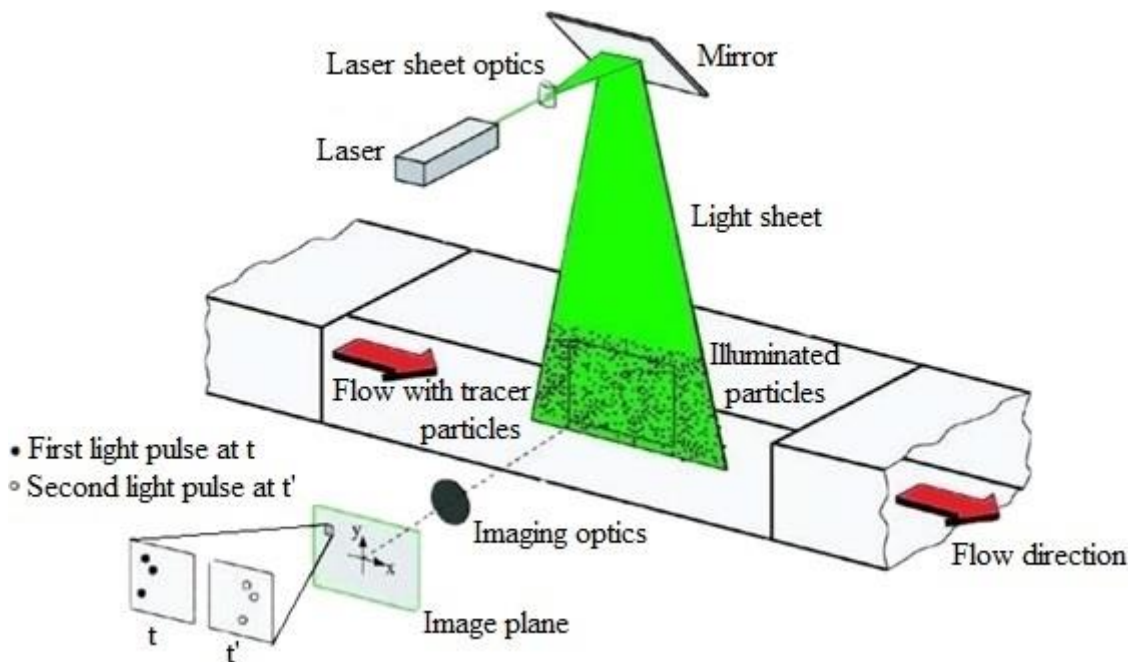
Figure 3.2: The components of a PIV system [69].

3.1 Rayleigh Scattering

Scattering is the phenomenon of the dispersion of light or other electromagnetic radiation when is incident on particles. More specifically, when an electromagnetic wave illuminates a particle, the latter becomes polarized (separation of positive and negative charges on the two sides), forming an induced dipole, which will oscillate on the electromagnetic wave's frequency. This oscillation results in scattering, a secondary radiation generated by the particles [70].
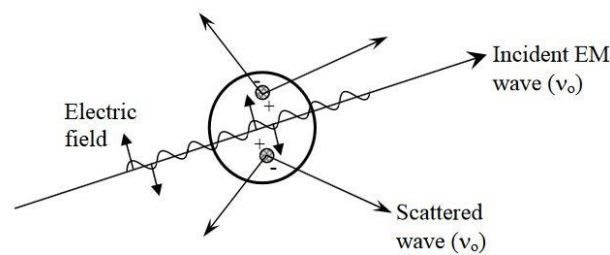
Figure 3.3: Elastic light scattering [71].

If the size of molecules or particles is much smaller than the electromagnetic wave's wavelength, then this type of scattering is called "Rayleigh" scattering". It was given its name in honor of John William Strutt (known as Lord Rayleigh), who first described it in 1871 in a series of papers [72], [73], [74], [75] and he attributed the sky's blue color to the Rayleigh scattering of sunlight when incident to air molecules. For particles of bigger radius the Rayleigh scattering is not dominantly applied and when the particle size is the approximately the same size as the electromagnetic wave's wavelength the scattering follows the Mie theory [76], [77].
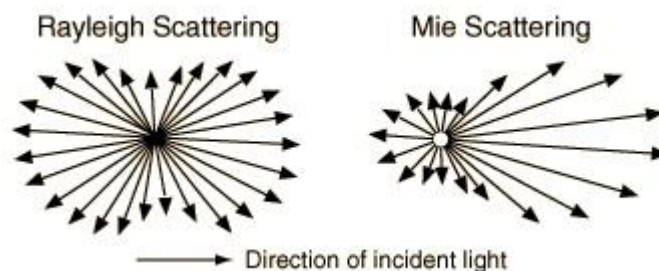
Figure 3.4: Direction of incident light for Rayleigh and Mie scattering respectively [78].

Generally, Rayleigh scattering applies for a particle size of $x \ll 1$, where x is the ratio:

$$x = \frac{2\pi r}{\lambda} \tag{2.1}$$

where r is the particle's characteristic length (radius) and λ is the light's wavelength. The dependence of the particle's or molecule's diameter on the value x for a 532 nm wavelength used in PIV applications is demonstrated in Figure 3.5. It is obvious that Rayleigh scattering is applicable for particles of diameter smaller than 100 nm.
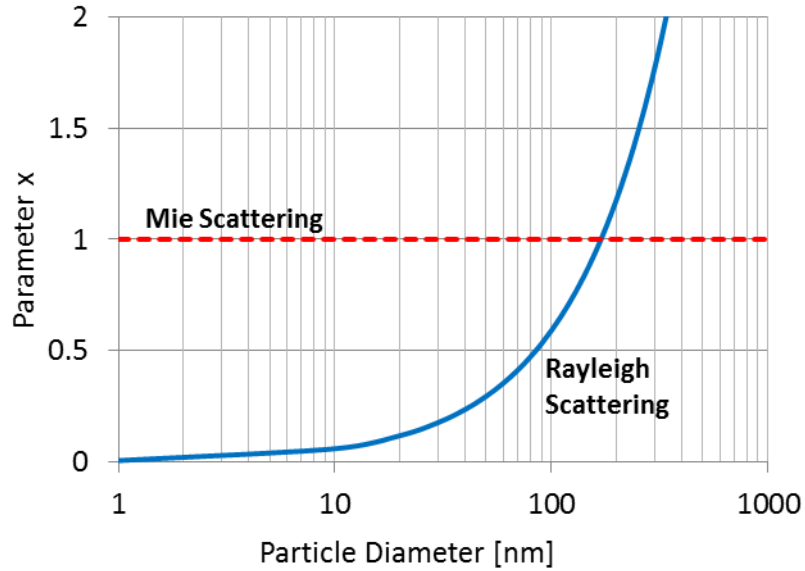
Figure 3.5: The dependence of the particle's diameter on parameter x for a 532 nm wavelength.

The intensity of light undergoing Rayleigh scattering for small particles is expressed in the following form [79]:

$$I = I_o \frac{\pi^4 d^6}{8\lambda^4 R^2} \left(\frac{n^2 - 1}{n^2 + 2} \right)^2 \left(1 + \cos^2 \theta \right) \tag{2.2}$$

Here I_0 is the intensity of the incident light, R is the distance between the particle and the light source, d is the diameter of the particle, n is the refractive index from the incident light and θ is the scattering angle. From Eq. (2.2) it is obvious that the scattering efficiency I / I_0 is inversely proportional to λ^4 and R^2, meaning that the scattering of light by smaller particles is enhanced by increasing the frequency of the radiation (reducing wavelength) or reducing their distance from the light source. It is also concluded that the scattering efficiency is enhanced by increasing the particle size, as it is proportional to d^6. Therefore, the size of the particles employed in PIV applications becomes the critical parameter for increasing the scattering efficiency.

23

The scattering efficiency of a particle is plotted as a function of scattering angle in Figure 3.6. Two different distances between the light source and the scattering plane as well as multiple particle sizes were investigated. In most PIV setups the CCD camera is installed perpendicularly (90°) to the laser light sheet, where the scattering efficiency is minimized. A striking observation is that scattering efficiency for 10 nm particles is of the order of ~10^{-24} and that for 100 nm particles of the order of 10^{-18}, both of which are extremely low values, which explain the low particle count rate observed experimentally when particles with $d <$ 100 nm are employed.
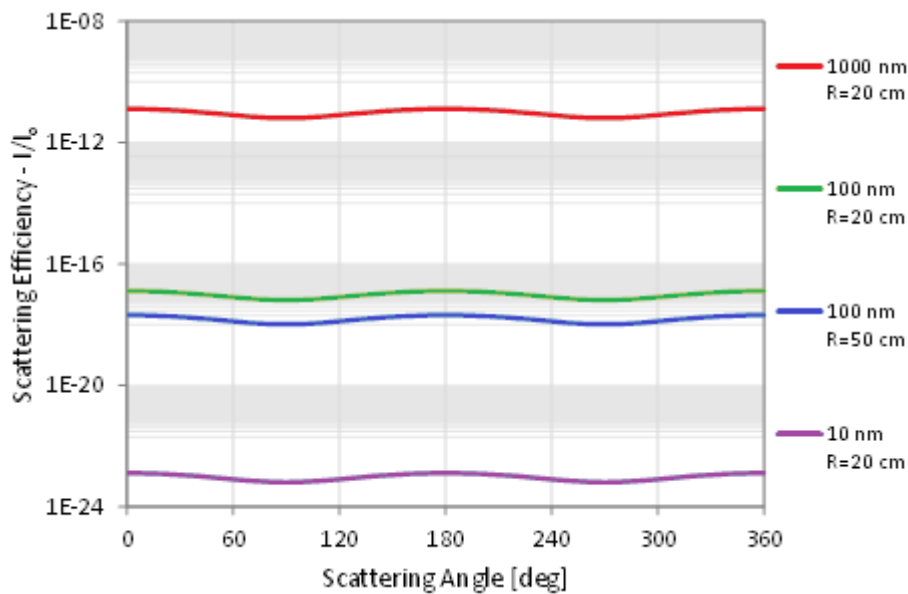
Figure 3.6: Rayleigh scattering efficiency for particles as a function of scattering angle using Eq. (2.2). The wavelength of the laser light used is 532 nm and the value of the refractive index for Al is 0.938777.

3.2 Tracer Particles (Relaxation time)

The dynamics of a particle suspended in a flow play a crucial role for the faithful visualization of the flow, especially in supersonic flows, where, due to the existence of shock waves, the velocity fluctuations are very steep. The assumption of spherical particle shape is valid for small droplets and monodisperse solid particles that are commonly used in PIV applications. Melling [80] quantified the particle's response according to the relaxation time (τ_p), which is defined as the time needed for the velocity lag $\left|\hat{V}\right| = \left|\hat{U}_p - \hat{U}_f\right|$

to be reduced by a factor of $\frac{1}{e} = 0.368$, where $\hat{U}_p$ and $\hat{U}_f$ are the instantaneous velocities of the particle and fluid respectively.

More specifically, he used a simplified form of the equation for unsteady motion of a suspended sphere for PIV measurements in gases,

$$\frac{d\hat{U}_p}{dt} = -C(\hat{U}_p - \hat{U}_f),$$
(2.3)

a modified Stoke's drag coefficient

$$C_D = \frac{24}{Re_D\left(1 + 2.7Kn_d\right)},$$
(2.4)

and the Knudsen number Kn as

$$Kn = \frac{l}{d_p},$$
(2.5)

where l is the mean free path of the gas, to express the relaxation time through the following equation:

$$\tau_p = \frac{\rho_p d_p^2}{18\mu}\left(1 + 2.7Kn_d\right).$$
(2.6)

It is obvious from Eq. (2.6) that the particle's response is a function not only of particle's properties but fluid's as well. As the flows characteristics are determined by the fluid selection and the particle's density by the particle's type, the particle's diameter d_p is the only property remained to adjust for the minimization of the relaxation time. Thus, it is deduced that the smaller the particle's size is, the more accurate its response in the flow's fluctuations will be, as it is also shown in Figure 3.7, in which the smaller particles recover faster after the shock [80].

However, the reduction in particle's diameter would result in a subsequent reduction of particle's scattering efficiency mentioned in section 3.1 and thus in all PIV applications a compromise between the increased scattering efficiency of bigger particles and the accurate representation of the flow is inevitable.

A list of particles used for seeding in gas flows along with the particle size and the laser characteristics is presented in Table 1 [80]. The particles have a typical size of ~1 μm or

greater and the only exceptions are the TiO_2 and Al_2O_3 particles with size 0.7-1 μm and 0.3 μm respectively.

Table 1: Seeding particles in gas flows [80].

| Material | d_p (μm) | Laser | Pulse energy, pulse time | Light sheet | | Reference |
				w (mm)	t (mm)	
TiO_2 (m = 2.6, ρ = 3500 kg m^{-3})	<1	Nd:YAG	10 mJ, 20 ns	15	0.3	Reuss *et al* (1989)
TiO_2, ZrO_2	0.7–1	Nd:YAG	110 mJ, 12 ns			Paone *et al* (1996)
Al_2O_3 (m = 1.76, ρ = 3970 kg m^{-3})	0.3	Nd:YAG	400 mJ		0.2	Muniz *et al* (1996)
	3	Nd:YAG	9 mJ, 6 ns			Anderson *et al* (1996)
	0.8	Ruby	20 ns	150	$\simeq$1	Krothapalli *et al* (1996)
Polycrystalline	30	Nd:YAG	135 mJ, 6 ns			Grant *et al* (1994)
Glass	30	Ruby	30 mJ, 30 ns			Schmidt and Löffler (1993)
Oil smoke	1	Ruby	5 J			Stewart *et al* (1996)
Corn oil	1–2	Nd:YAG	100 mJ			Jakobsen *et al* (1994)
Oil	1–2	Nd:YAG	120 mJ		0.4	Westerweel *et al* (1993)
Olive oil (m = 1.47, ρ = 970 kg m^{-3})	1.06	Nd:YAG	70 mJ, 16 ns	200	0.5	Höcker and Kompenhans (1991) Fischer (1994) Raffel *et al* (1996)
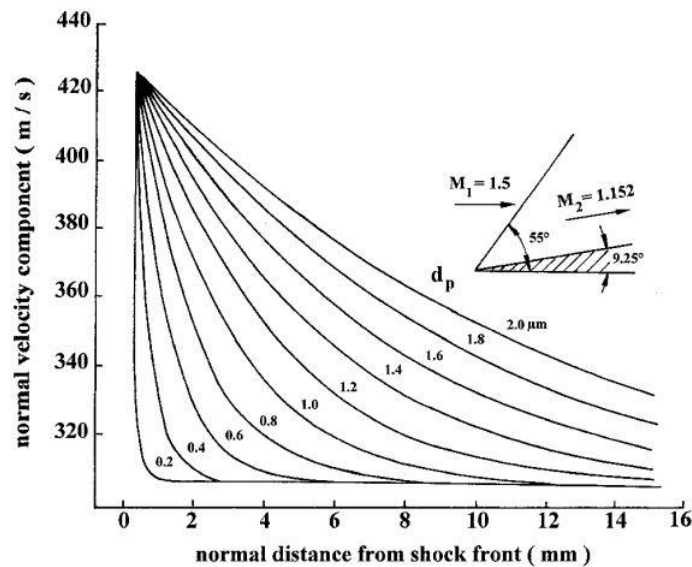
Figure 3.7: Particle response downstream of an oblique shock [80].

For the visualization of gas flows, solid or liquid particles are used. Solid tracers have the drawback of agglomeration, which results in the formation of bigger particles of unknown size, and liquid tracers have the disadvantage of fast evaporation. The relaxation time and consequently the response of the particles is estimated as the tracers pass through

26

a shock wave, known as shock wave test [81], [82], [83], [84], [85], [86], [87], [88] and also demonstrated previously in Figure 3.7.

Ghaemi et al. [89] used a Spark Discharge Source in argon to generate 10 nm primary particles, which through rapid coagulation and oxidation were grown to aggregates of 1 μm. These aggregates exhibit a fractal-like structure, which enhance the light scattering, in contrast to the particles with a spherical shape. The experimental investigation through an oblique shock of these particles showed a relaxation time of 0.27μs, which is approximately a reduced order of magnitude with respect to the compact agglomerated with an approximate 2.0 μs relaxation time [89].

The fast response of Al particles is contrasted against TiO_2 particles of smaller size (~0.5 μm). A significantly greater relaxation time of 2.0 μs is shown, which is attributed to the greater effective density of TiO_2 particles, highlighting the capabilities of the former ones to perform laser-based measurements in supersonic and hypersonic flows [89].

Chapter 4:

Experimental Setup and Approach

4.1 Hardware

Besides the main setup for the PIV experiments, described in detail in section 4.1.1 (Figure 4.1), another setup was also implemented. In this secondary setup it is possible to switch between two configurations (Figure 4.2): the Scanning Mobility Particle Sizer (SMPS) explained in section 4.1.2, through which particle concentrations are measured, and the DMA explained in section 4.1.3, through which particle size selection is implemented for PIV experiments.
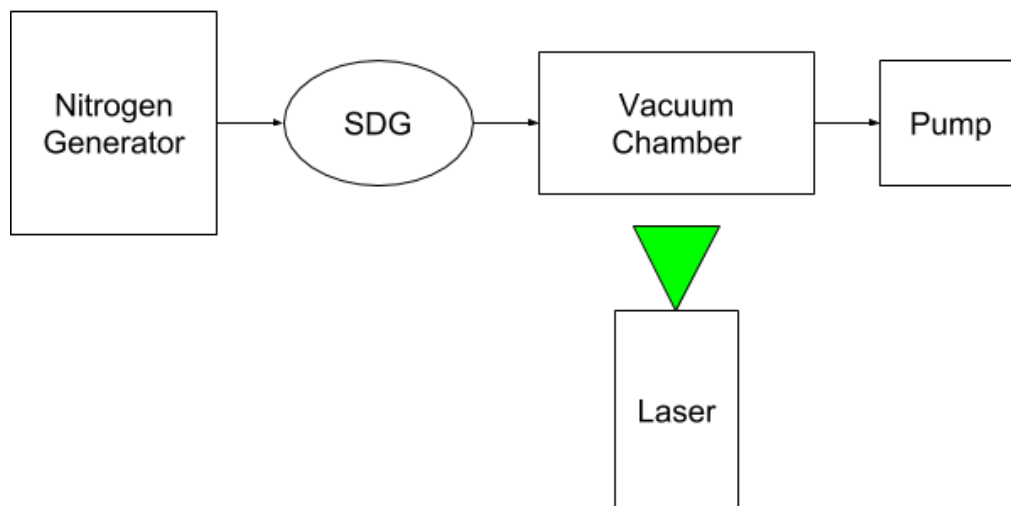
Figure 4.1: Schematic of the PIV setup.
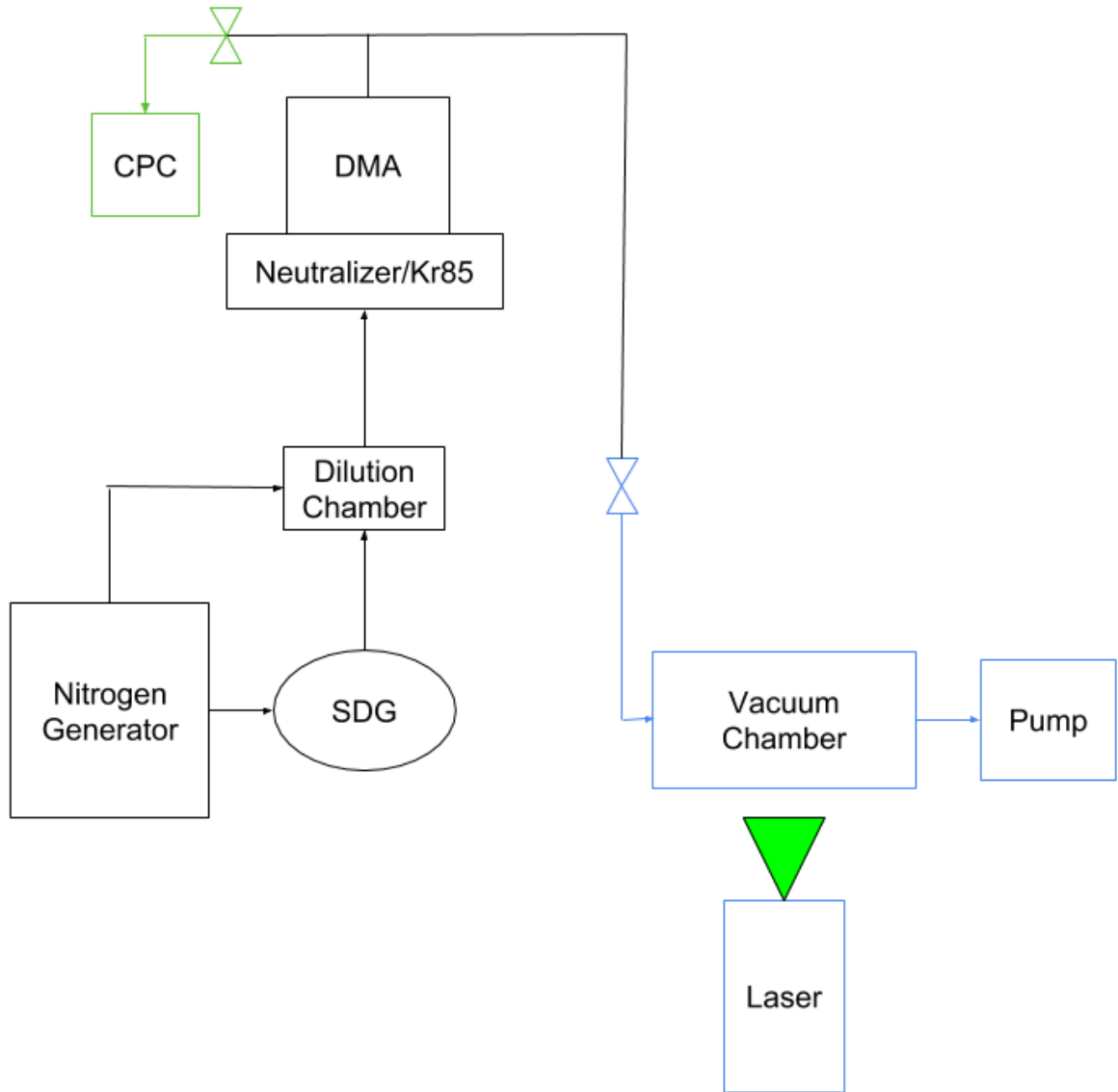
Figure 4.2: Schematic of the implementation of DMA and CPC devices. With green color are displayed the parts that belong only to the SMPS mode, with blue color the parts that belong only to the Particle Size Selection with the DMA and with black color are displayed the parts that are part of both configurations.

4.1.1 Particle Image Velocimetry (PIV) apparatus

The procedure of the setup presented in Figure 4.1 is as following: the nitrogen flow is seeded with tracer nanoparticles capable of scattering laser light. A heated capillary is then used to transfer the ions from the atmospheric pressure into the first vacuum compartment operated at 20 or 5 mbar, where the flow undergoes expansion. Two Nd: YAG lasers irradiate the jet and a CCD camera is used to capture the illuminated by the particles light. At the end, a 2D velocity vector field is produced. The spark discharge source (SDG), the electrospray ionization source (ESI) and the Nd:YAG lasers will be separately explained

later in subsections 4.1.1.1, 4.1.1.2 and 4.1.1.3 respectively. A nitrogen generator is used to supply the carrier gas, which is seeded with tracer particles and inserted into the vacuum chamber through the capillary.

The capillary has 0.5 mm inner diameter, 1/16 inches (1.5875 mm) external diameter and 80 mm length. In order to heat the capillary to the specific temperature of 200 °C two 100 Watt and 230 V heaters are connected to it, as shown in Figure 4.3. A type K thermocouple is also installed, to monitor the temperature in real time.
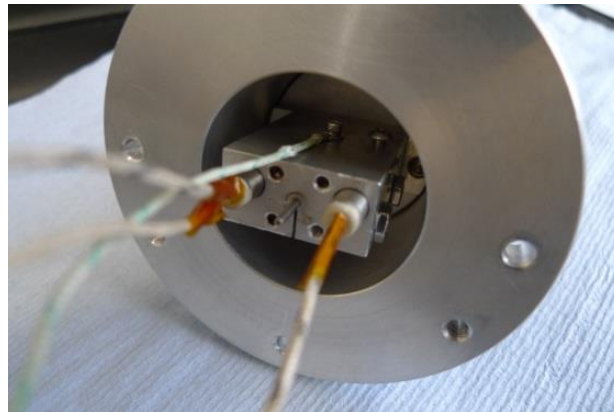
Figure 4.3: Setup of capillary, heaters and thermocouple on the vacuum chamber.

The sealing between the tube coming from the spark source and the capillary was achieved using thread sealing tape as shown in Figure 4.4.
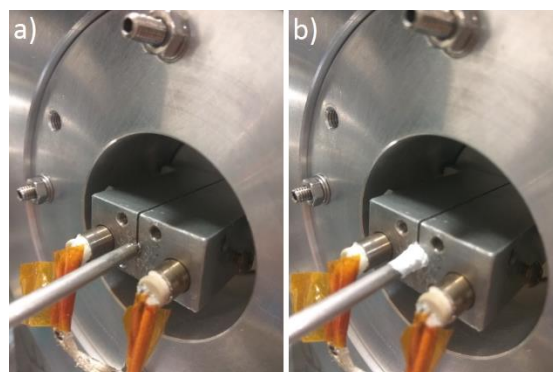
Figure 4.4: Capillary sealing before (a) and after (b) using the thread sealing tape.

When the experiments include the Aerolens^{TM}, a 5x5 mm^2 and 100 mm long rectangular glass channel is installed a few millimeters downstream the capillary. The four corners of the Aerolens^{TM} are painted black, as shown in Figures 4.5, 4.6, to minimize the laser reflections and consequently the resulted noise captured by the camera.
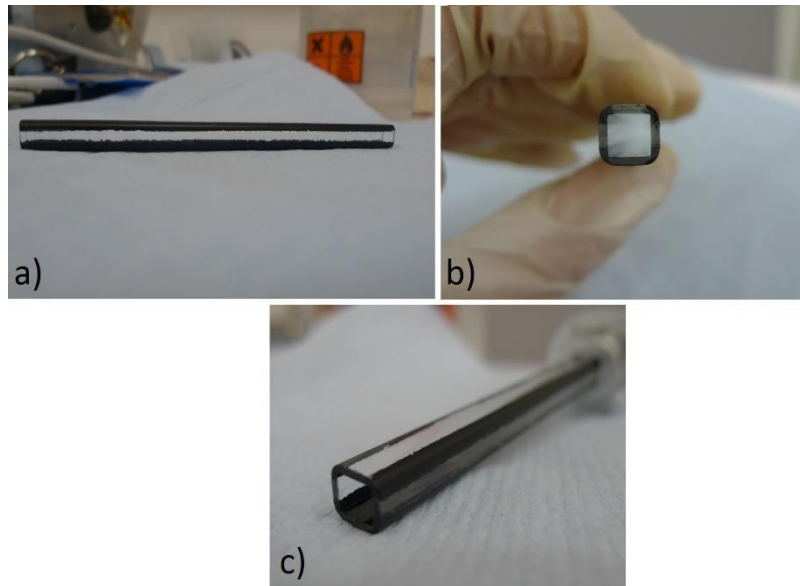
Figure 4.5: Aerolens™ glass channel.

The vacuum chamber is comprised of two vacuum compartments. The first vacuum chamber is where the nitrogen flow exits the capillary and undergoes expansion. Aerolens™ is positioned a few millimeters downstream from the capillary's aperture, as shown in Figure 4.6, and confines the entire under-expanded flow.
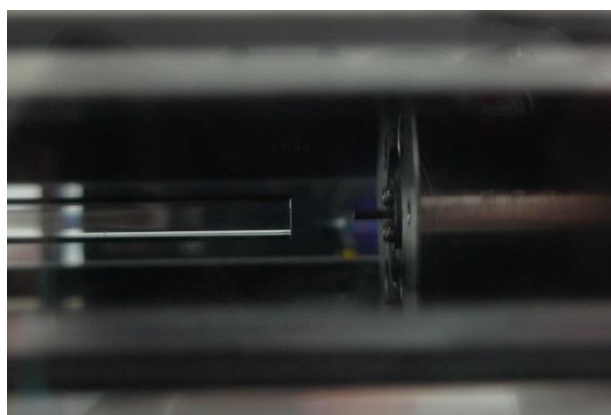
Figure 4.6: Side view of the capillary's outlet.

The Aerolens™ extends till the second consecutive compartment, where at the rear end the pumping is applied through a 28 m³/h rotary pump. The first and second compartments (chambers) are hermetically separated and are only connected via the Aerolens™, thus the entire gas load is directed through the Aerolens™. The second chamber operates at a

pressure of 26.6 or 6.6 mbar (depending on the case). In order to be able to investigate the nitrogen flow throughout the entire length of the Aerolens™, the vacuum chamber is set up in two different configurations, as shown in Figure 4.7.
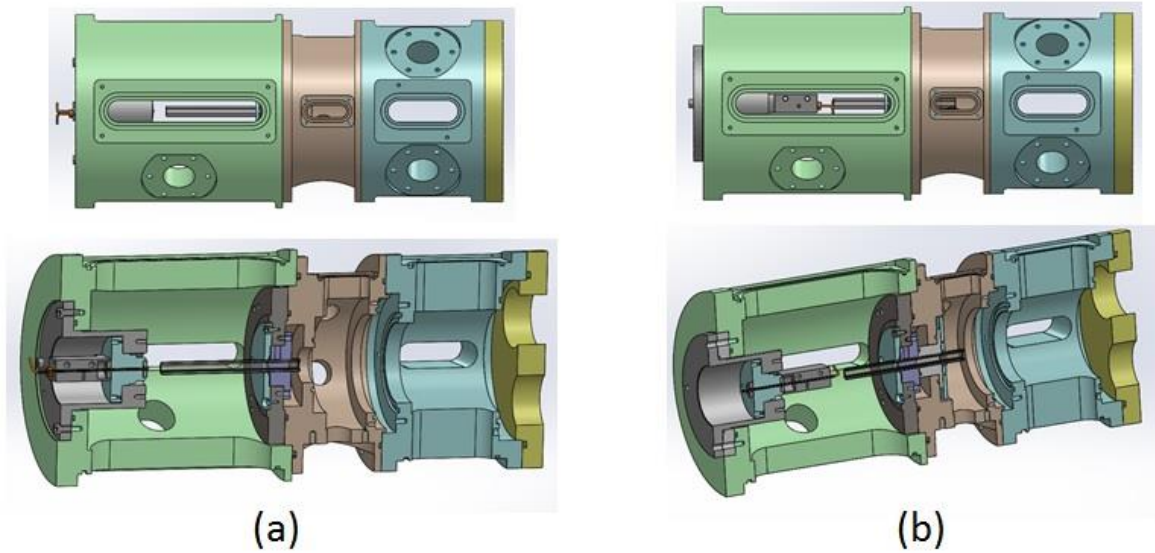
Figure 4.7: The configuration (a) is used for the visualization of the flow inside the first 75 mm of Aerolens™, while configuration (b) is used for the remaining 25 mm.

The experimental parameters, such as the distance between capillary's exit and the entrance of Aerolens™, the chamber's pressure, etc., are kept unaltered for both configurations.

The image capturing is achieved with a PowerView Plus 4MP Camera, which is designed for Particle Image Velocimetry measurements and displayed in Figure 4.8.
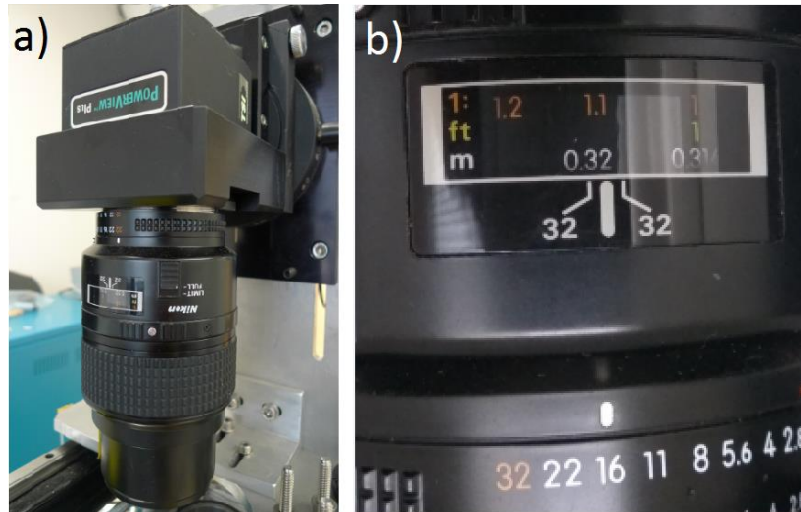
Figure 4.8: The PowerView Plus 4M Camera (a) and the settings used for the experiments (b).

A critical parameter for the PIV experiments is the precise focusing of the camera, as the particles should look like very small bright spots. This is achieved by concentrating many particles inside the chamber, while no pumping is happening, by inputting some smoke, e.g. when burning a paper. The final result of the focused camera is displayed on Figure 4.9 and the settings of the camera on Figure 4.8.

Figure 4.9: Visualization of the particles when the camera is focused.

Two modes of operation are available: the Free-Run mode, which helps in the initial diagnostics and the alignment of the system, and the Frame Straddling mode, which is used for the actual PIV measurements. The camera captures two consecutive image frames of the illuminated flow field as one image capture and through the Insight $3G^{TM}$ software the frames and their particles can be later separately examined. The time between the two laser pulses, called Delta T, is dependent on the velocity of the flow field and can be adjusted within the Insight $3G^{TM}$ software [90]. The sequence diagram of the camera in the Frame Straddling mode is presented below:
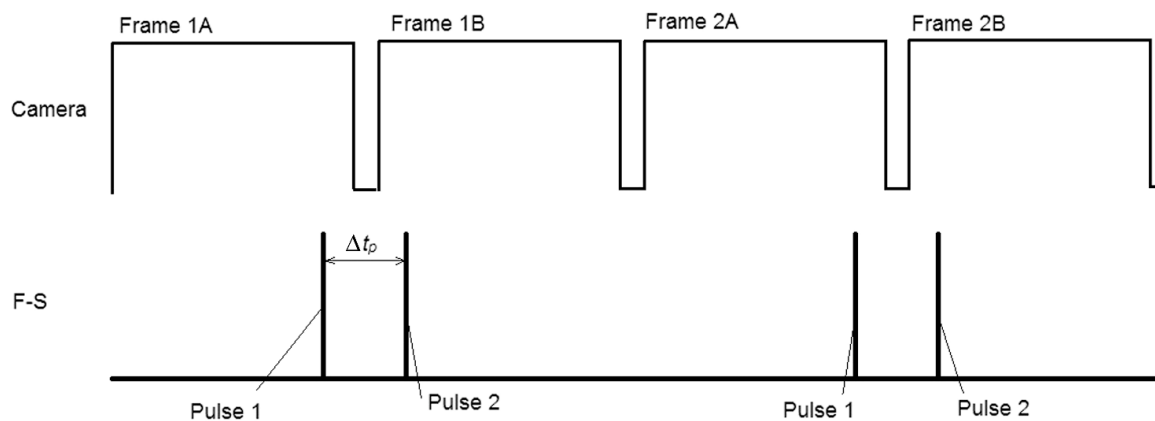
Figure 4.10: Sequence diagram of the camera in Frame Straddling mode [84].

The Synchronizer is a timing and control device that plays a very crucial role, as it constitutes the communication path between all the devices connected to it (laser, camera and computer) and manages to make them all work together by sequencing them properly. Thus, the delay between the laser pulses is precisely adjusted to the image captures of the CCD camera through the synchronizer.

Figure 4.11: The synchronizer.

In the current experiment, the flow was investigated at four different positions. The optical access for the CCD camera and the double-pulsed Nd-YAG laser is made possible through window ports arranged at right angles. The ports are sealed by using 3 mm thick acrylic sheet when not in contact with the laser beam or glass for the ports that the laser beam enters or exits. The laser sheet comes through the side port of the vacuum chamber, passes through the axis of the flow and exits from the other side port. The orientation of the CCD camera is perpendicular to the side port and thus the CCD camera is placed above. The interior of the vacuum chamber is painted black in order for the reflections to be minimized. The alignment of the system for this experiment is a matter of crucial importance. For this reason, a supporting frame for the whole PIV experiment was designed and constructed. Figure 4.12 depicts the experimental rig including the Nd-YAG lasers, the power supplies, the CCD camera, the spark source, the vacuum chamber and the nitrogen generator.
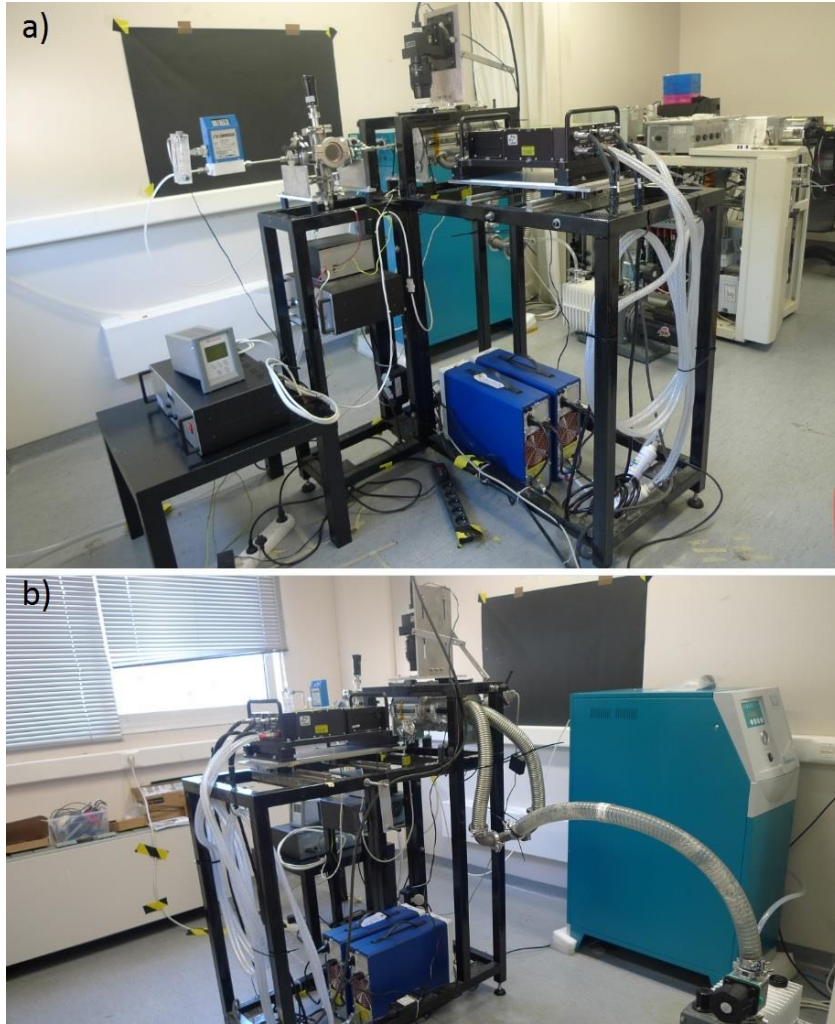
Figure 4.12: The spark discharge source, the vacuum chamber, the Aerolens^{TM} and the supporting frame were all designed by the team of Fasmatech Science and Technology SA.

All the experiments were conducted in the laboratories of Fasmatech Science and Technology S.A., facilitated in the National Centre of Scientific Research "Demokritos", Athens, Greece.

4.1.1.1 Spark Discharge Source (SDG)

The design of the Spark Discharge Source was based on a published work of Ghaemi et al. [89], in which, as mentioned in section 3.2, agglomerates of fractal-like geometry with an enhanced scattering efficiency are created. Aluminum was used for the electrodes of the spark source and nitrogen as the carrier gas.

The power supply of the spark source operates at two basic configurations: the "free spark" mode and the "resistive spark" mode, as presented in Figure 4.13.
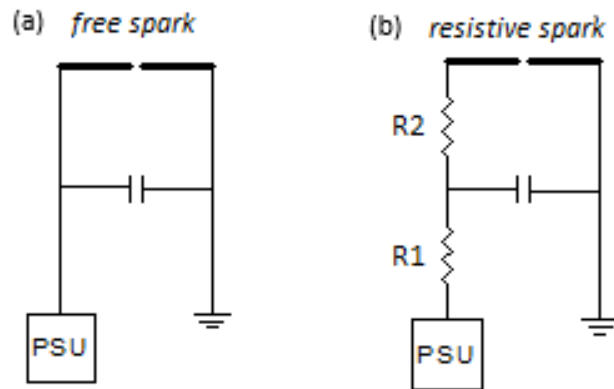
Figure 4.13: Schematic diagram of the "free spark" mode (a) and the "resistive spark" mode (b).

In the free spark mode the current is allowed to run freely during the charging and discharging of the capacitor. On the other hand, in the resistive spark mode the resistor R1 is introduced between the power supply and the capacitor in order to limit the current during the charging and the resistor R2 is introduced in the discharge path.

The effect of limiting the current during charging and discharging of the capacitor has a major influence on the size distribution of the particles. Thus, in order to investigate the particle size distribution as a function of operating parameters (breakdown voltage, frequency, gas flow, etc.), experiments were conducted with a Scanning Mobility Particle Sizer (SMPS) system, as presented in section 4.1.2. The spark source created by Fasmatech Science and Technology S.A. and used in the experiments of this work is presented in Figure 4.14.
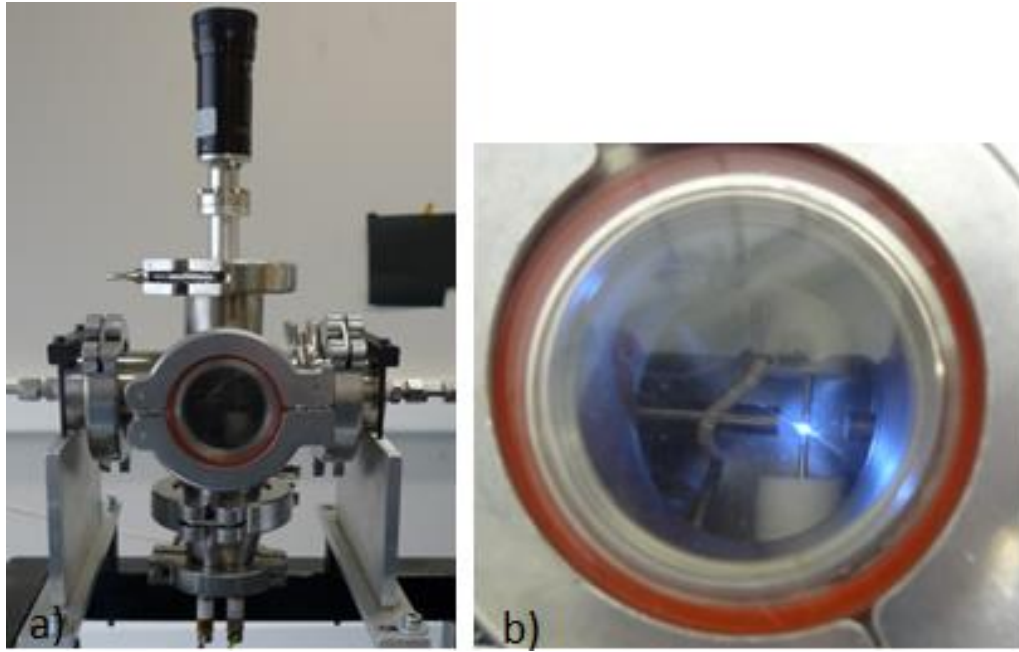
Figure 4.14: The spark source used in the experimental setup.

4.1.1.2 Electrospray Ionization (ESI)

The Electrospray Ionization was implemented in Particle Image Velocimetry with the use of fluorescent molecules in previous experimental work of Fasmatech Science and Technology S.A., where Rhodamine B was used inside methanol [22].
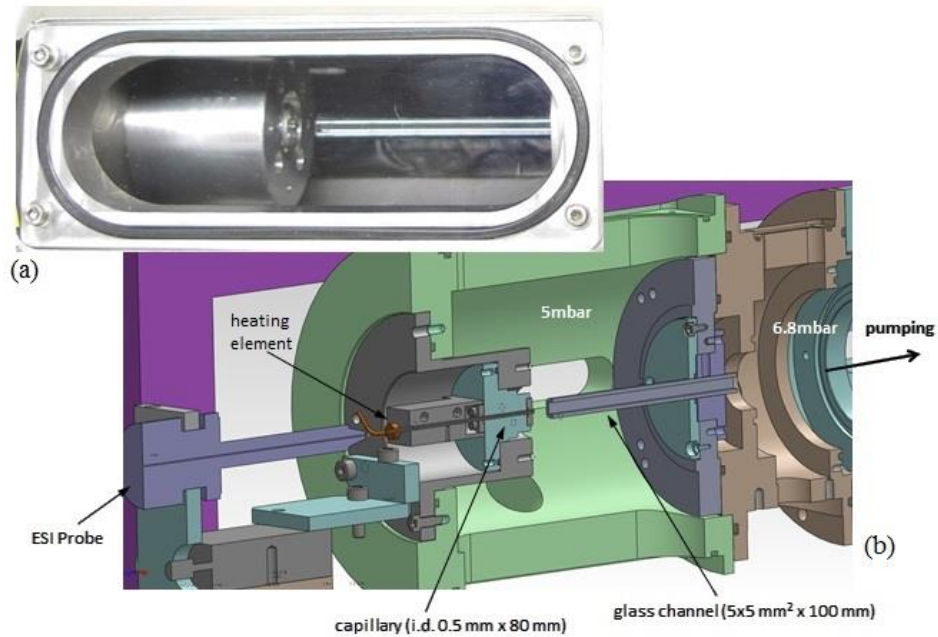
Figure 4.15: (a) The capillary holder and Aerolens^{TM} are shown from the side port of the installed apparatus. (b) Cross section of the 3D ESI model [22].

The results indicated a highly inaccurate visualization of the flow compared to the computational calculations that probably emanates from incomplete desolvation of the ionized clusters.

In the current work 100 nm fluorescent particles inside water with an excitation maxima of 540 nm and emission maxima of 560 nm were implemented.
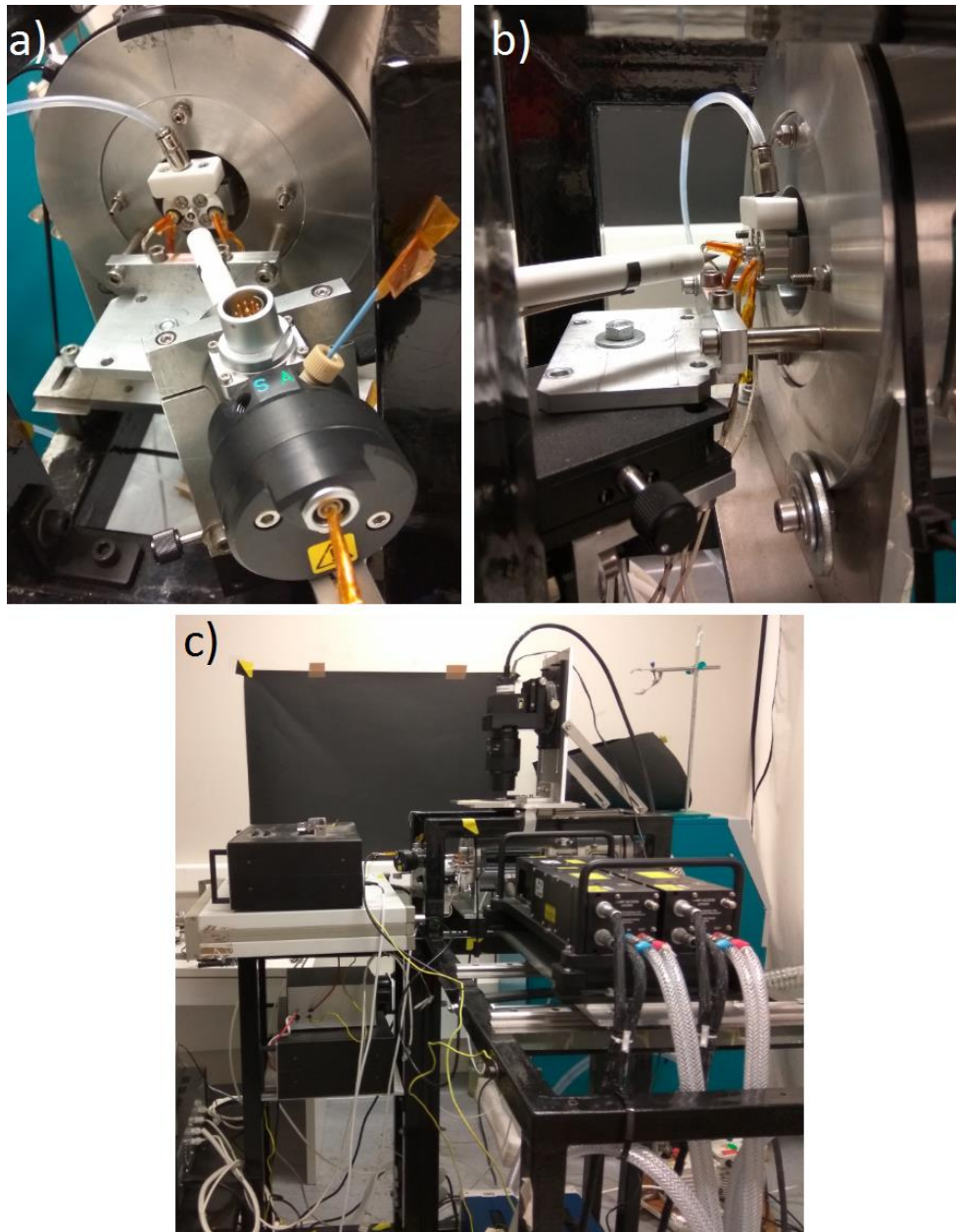
Figure 4.16: Close up view of the ESI source (a), (b) and experimental rig of the implementations of the ESI source in the PIV experiments (c).

4.1.1.3 Nd: YAG Lasers

For the conducted experiments the Twins BSL lasers from Quantel were used, which belong to the category of the Double- pulse Nd: YAG laser systems. The laser produce green light at 532 nm wavelength, with a short duration of 10 ns and a medium energy of 120 mJ. The short duration of the pulse manages to "freeze" the motion of supersonic flows and the use of double pulsed laser ensures the short times between the pulses, which are required for such applications [92].

In a PIV experiment the laser uses optics in order to output a light sheet that irradiates the flow field. The properties of this light sheet are of vital importance and are adjusted with the help of a cylindrical and a spherical lens. The cylindrical lens receives the collimated laser beam and diverges it in the height direction. The thickness of the light sheet is controlled by the spherical lens and the camera focuses at the point where the waist of the light sheet is created, which is also set to be the axis of the capillary [93].
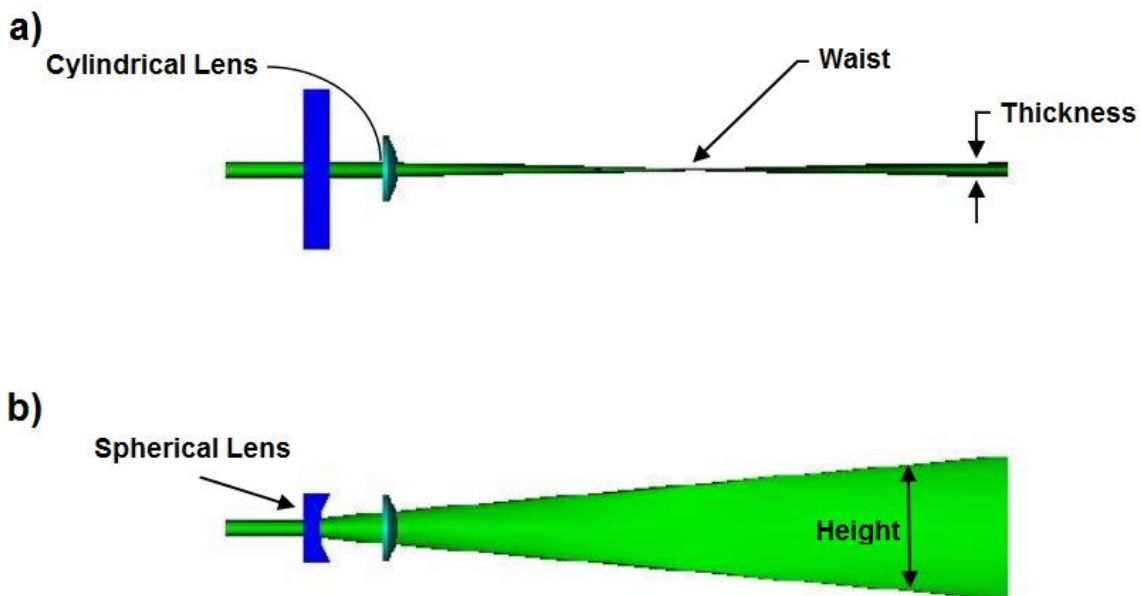
Figure 4.17: Top view (a) and side view (b) of the light sheet optics. [93].

In the conducted experiments a -50 mm cylindrical lens and a 200 mm spherical lens were used, resulting in a laser beam of 210 μm thickness and 18 mm height.

Spherical	100 mm			200 mm			500 mm			1000 mm			2000 mm		
Cyl (mm)	t (μ)	h (mm)	D (°)	t (μ)	h (mm)	D (°)	t (μ)	h (mm)	D (°)	t (μ)	h (mm)	D (°)	t (μ)	h (mm)	D (°)
-12.7	10.6	41	19.9	21	88	23.3	53	230	25.2	106	466	25.9	212	939	26
-25	10.6	18	6.9	21	42	10.3	53	114	12	106	234	13	212	474	13
-50				21	18	3.4	53	54	5.5	106	114	6.2	212	234	6.5
-100							53	24	2.1	106	54	2.7	212	114	3.1
-200							53	9	0.34	106	24	1.0	212	54	1.4

t: Thickness of the light sheet at the waist in μm
h: Height of the light sheet at the waist in mm
D: Divergence of the light sheet in degrees

Figure 4.18: Specifications of light sheet optics [93].

Laser alignment is a very critical parameter for receiving accurate and reliable results on the velocity of the flow. For the alignment of the 0.2 mm laser beam with the 0.5 mm capillary's outlet a procedure is followed, in which first a level is used in order to calibrate approximately the chamber to the laser in both axes (Figure 4.19). When both the laser and the chamber are brought to 0 degrees, cable ties are used on the chamber and progressively tightened while using the level to maintain the calibration, in order to keep the chamber stable.
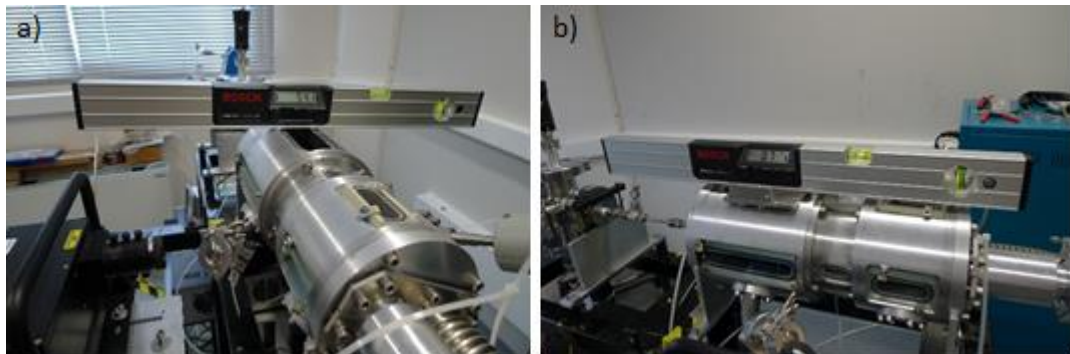
Figure 4.19: Chamber calibration with the level.

Afterwards, two metal slits are used, as shown in Figure 4.20. The one is adjusted on the entrance port and the other on the exit port of the vacuum chamber. The laser beam should enter the one slit and exit the other, in order to be certain that everything is aligned.
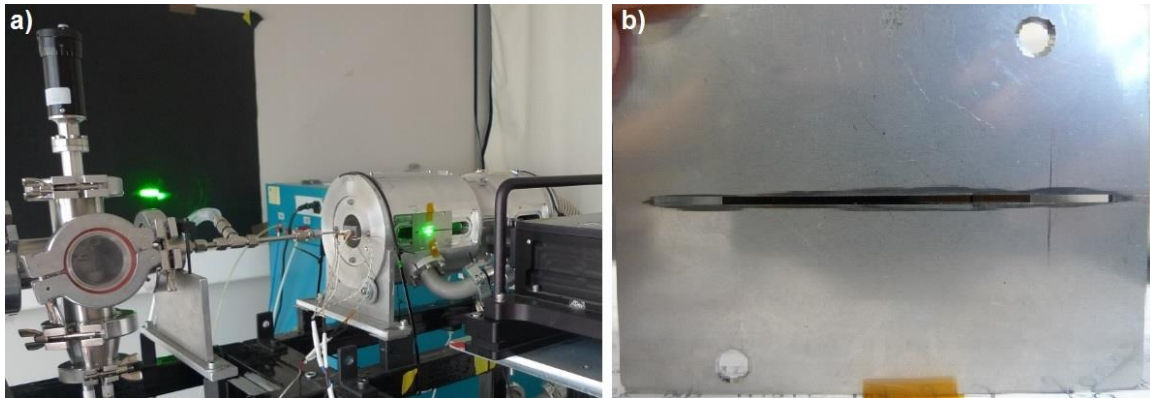
Figure 4.20: (a) Laser alignment with the use of slits and (b) close up view of the slit.

Then comes the final step of the calibration of the beam to the capillary's axis. Paper-markers, as shown in Figure 4.21, are used on the capillary while the laser's height is increased or lowered respectively through the screws on its supporting frame.
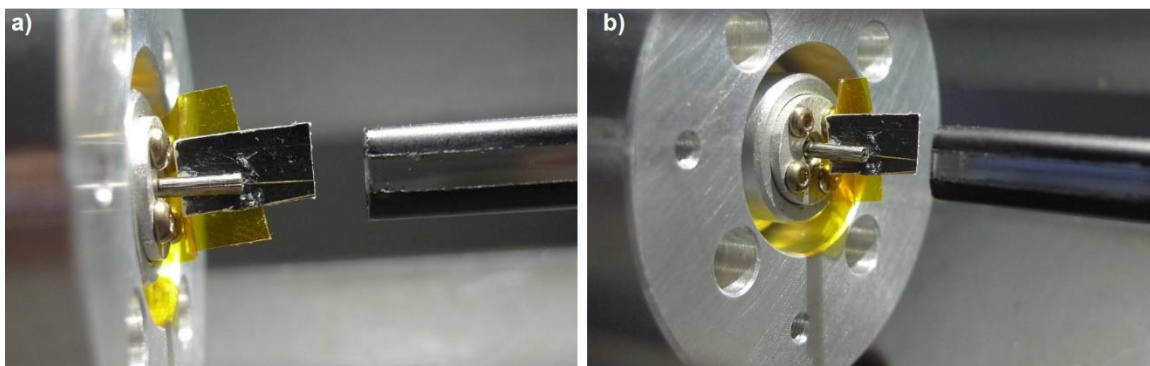
Figure 4.21: Laser alignment with the use of thermal paper behind the capillary.

Finally, the calibration is verified or even improved by firing the laser directly on the capillary on low power. While wearing the safety glasses and with the use of a flashlight to light the capillary's exit, the laser beam can be seen and checked if it fires to the axis of the capillary.

4.1.2   Scanning Mobility Particle Sizer (SMPS)

A Scanning Mobility Particle Sizer (SMPS) system, described previously in section 2.2, was made available by the "Environmental Radioactivity Laboratory" in Demokritos.

For this configuration, the valve going to the CPC should be open and the valve going to the vacuum chamber closed, as shown in Figure 4.22 (c). A guide on how to use the SMPS is given in Appendix C.
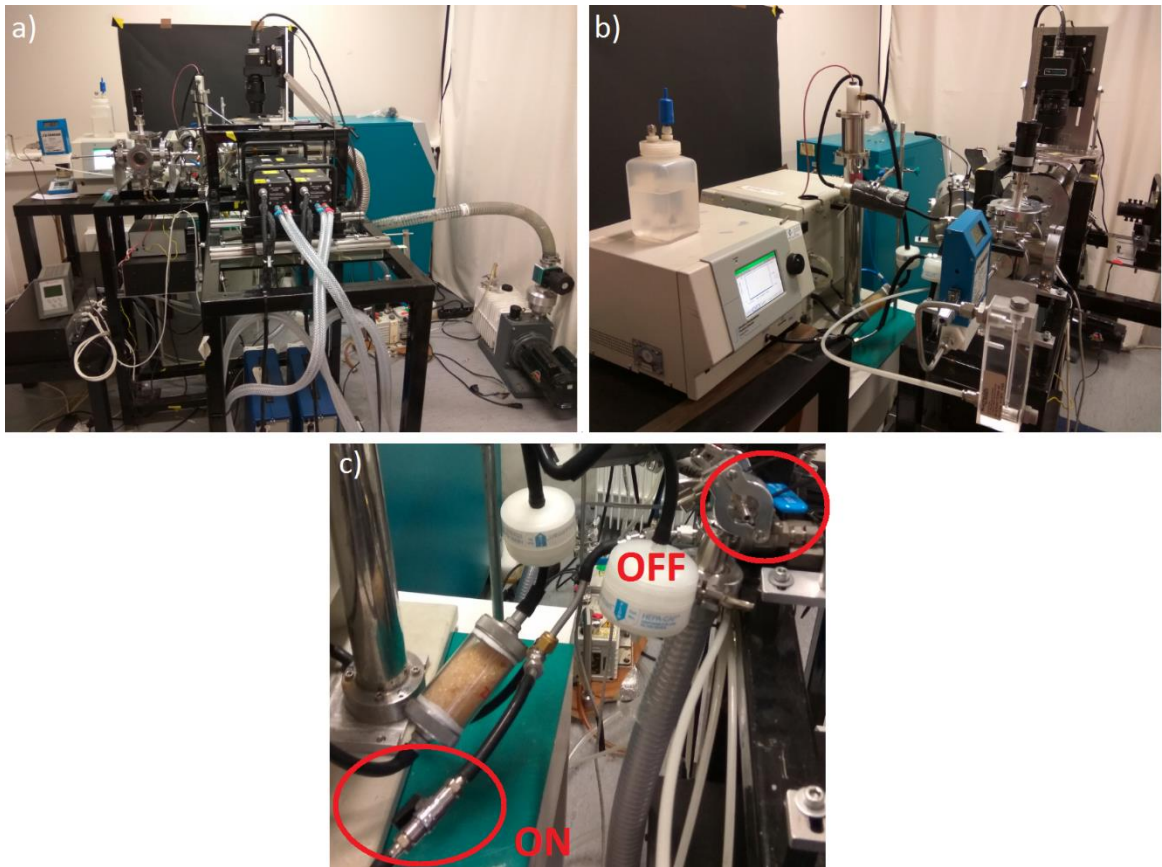
Figure 4.22: Photograph of the experimental system used for measuring size distributions, showing the spark discharge source, the DMA and the CPC.

It was found that, depending on the current flowing into the spark, the particle distributions change dramatically. For better understanding of the spark source's operation, two different capacitors (Figure 4.23) and three wirings that change the resistor value were examined in the tests. The red pins modify the R2 resistor and the black pins the R1 resistor, as shown in Figure 4.24. The results are presented in section 5.1.
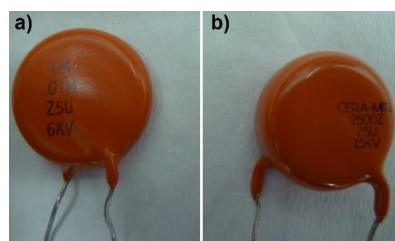
Figure 4.23: (a) 10 nF – 6kV capacitor, (b) 2.5nF – 15kV capacitor.
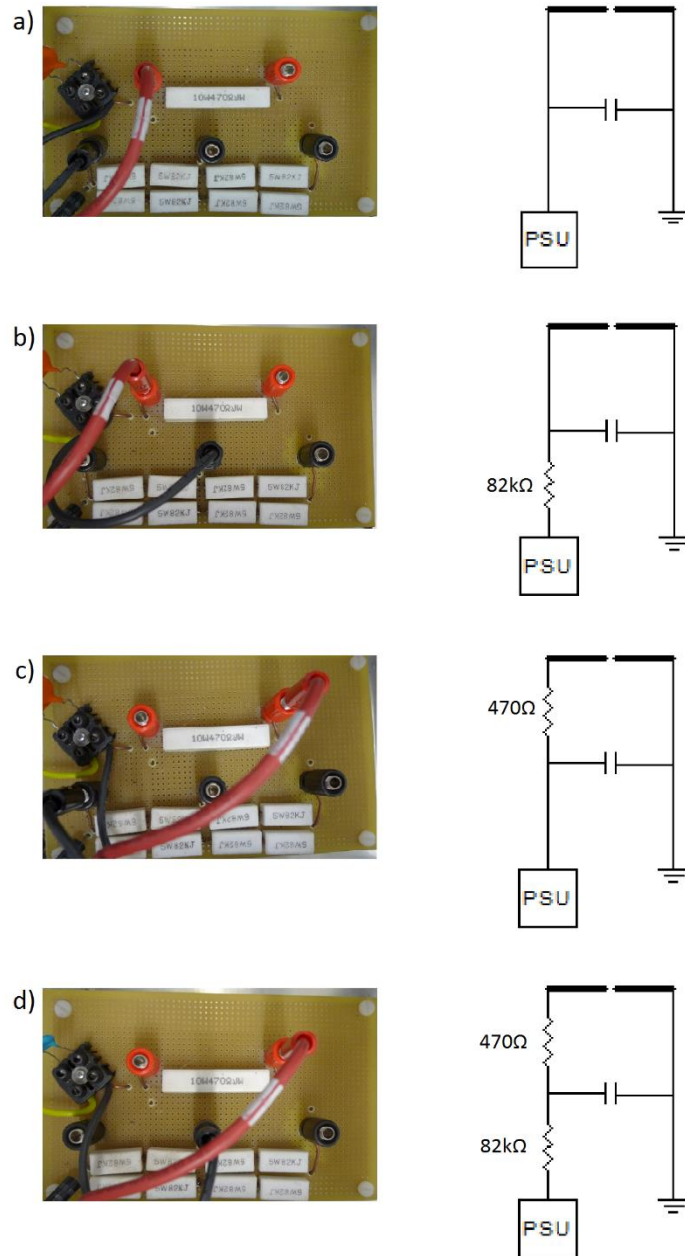
Figure 4.24: (a) Wiring 1, (b) Wiring 2, (c) Wiring 3, (d) Wiring 4.

4.1.3 Implementation of DMA for Particle Size Selection in PIV

The use of the DMA to allow only particles of a specific size to enter the vacuum chamber would give an end to the big problems of the deviation in particle size, the aging of the spark source, etc. The experimental setup, used for the particle size selection through the DMA, is presented in Figure 4.25. For this configuration, the valve going to the CPC should be closed while the valve going to the vacuum chamber should be open, as shown in Figure 4.25(c).
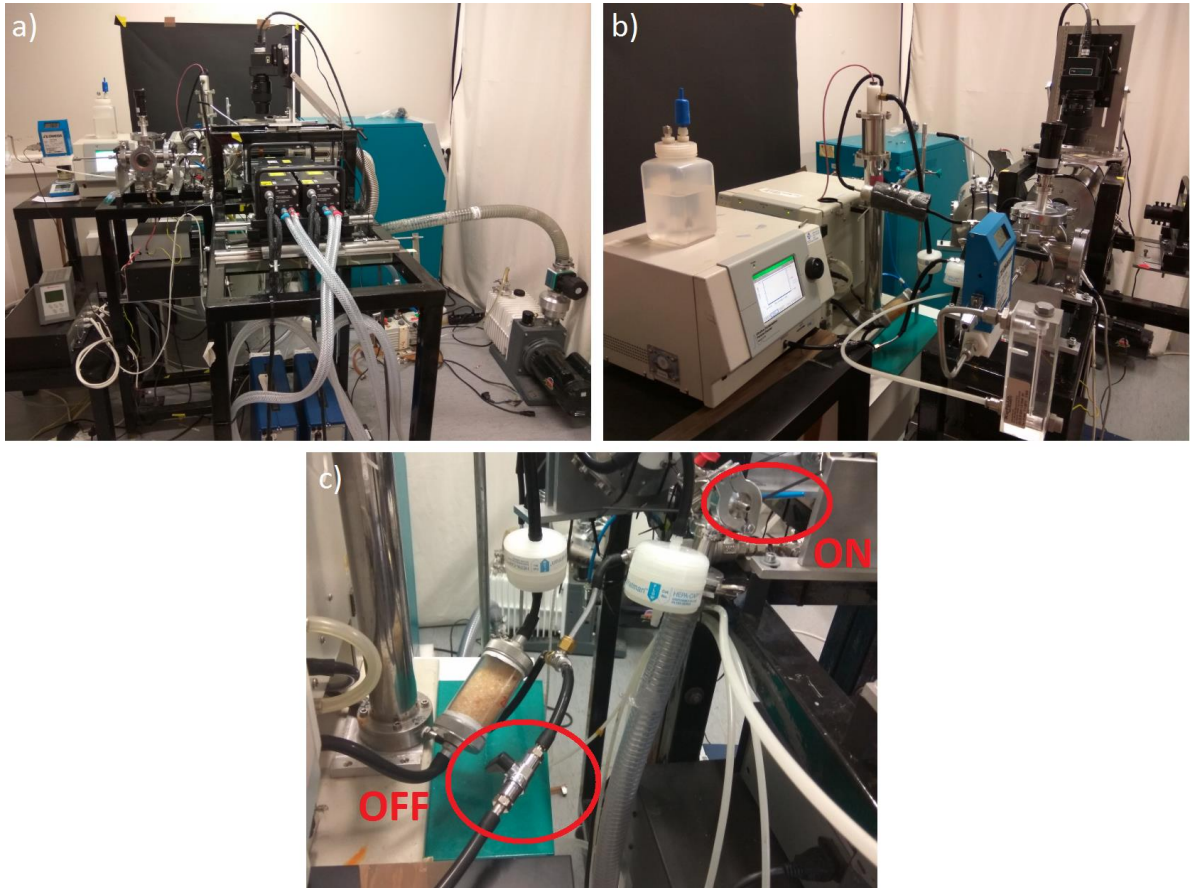
Figure 4.25: Photograph of the experimental setup, used for selecting specific particle size during the PIV experimental procedure.

Unfortunately, the particle concentration was too low, even when bigger particles of 100-200 nm were selected for seeding the nitrogen flow. Therefore, the time of the experiment would be extremely prolonged, making impossible to run it. A guide on how to select the size of the particles with the DMA is given in Appendix C.

4.2 Insight 3G™ Software for Image Processing

The utilized PIV system includes a commercial software package that enables the image capture and process as long as the visualization of the velocity vector fields. The Insight 3G™ software can measure the flow velocity using the Cross-Correlation technique (Figure 4.26). With this technique the first laser pulse exposes the first frame and the second laser pulse the second frame, thus optimizing the signal-to-noise ratio.
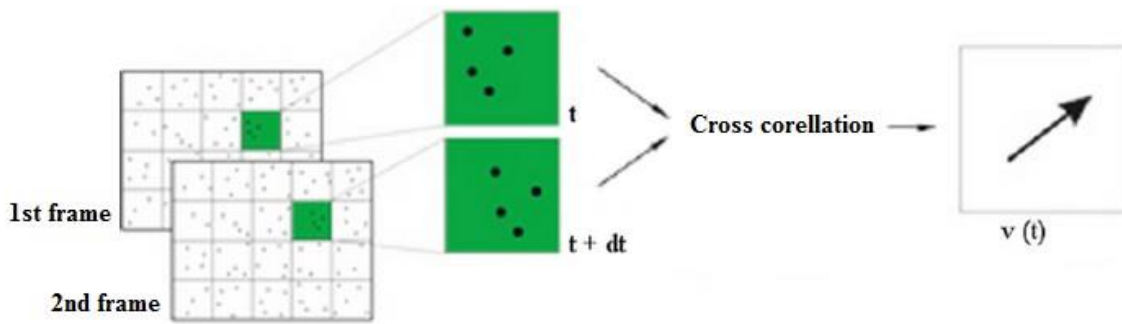
Figure 4.26: Cross Correlation technique in Particle Tracking Velocimetry [94].

The main difficulty encountered with this particular software is that it is designed for PIV applications which are developed at atmospheric pressure conditions, where both the tracer particle concentrations and the particle sizes are considerably larger than those encountered in a low pressure chamber. Therefore, the software algorithms are developed to specifically treat ensembles rather than individual particles.

It must be noted that the Insight 3G^{TM} software package does include a Particle Tracking Velocimetry algorithm, but a minimum number of 16 particles within a single interrogation window is required in order for the algorithm to respond accurately, which is not met in the experiments of this work.

The Insight 3G^{TM} software also enables the generation of "Maximum Intensity" images. It calculates the pixel-wise maximum intensity of the list of input images and creates a single image carrying the entire information. This tool has been really helpful for the validation of the vector field produced by the PTV custom code, developed in Matlab^{TM}.

The "Maximum Intensity" Image Generator was used intensively when investigating the flow field inside the glass channel, in which the enhanced noise near the wall boundaries resulted in many misleading vectors.

A comparison between the resulted vector map and the image generated from the list of the input images gives valuable information. For example, Figure 4.27 was one of the comparisons that were made, in order to conclude that there are no particles near the walls with velocity as high as 540 m/s, thus these misleading vectors should be removed. On the other hand, it was unexpected that slow particles with velocity lower than 60 m/s existed near the jet's axis. A guide on how to use the Insight 3G^{TM} software is presented in Appendix B.
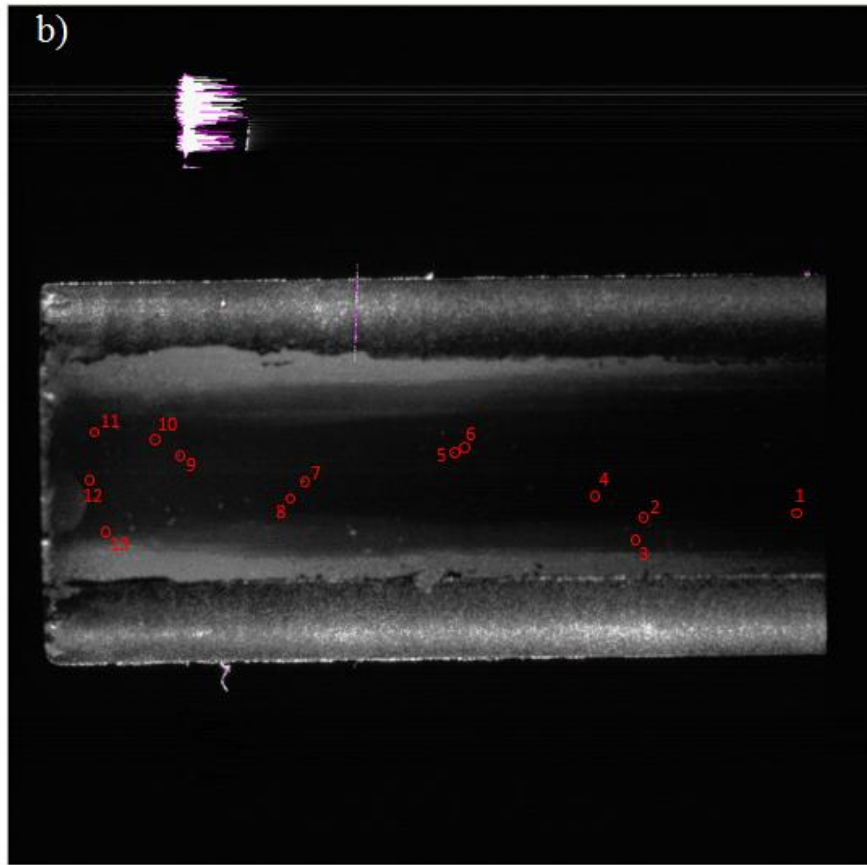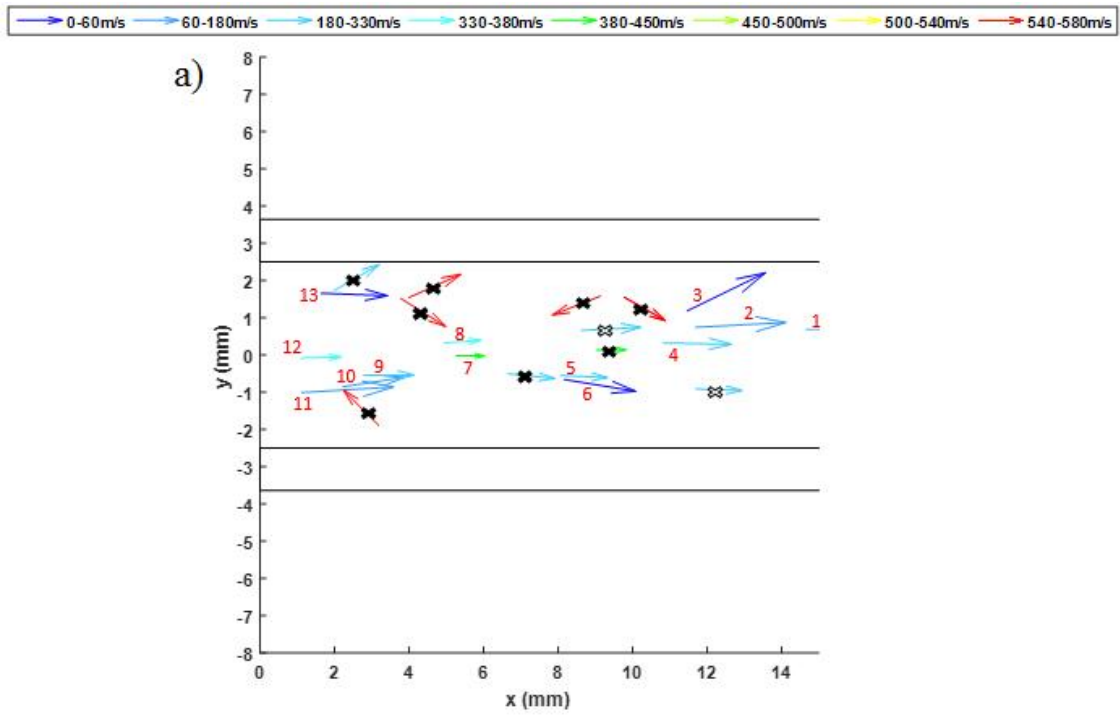
Figure 4.27: Comparison of (a) the vector field created by the PTV code and (b) the generated image using the Insight 3G™ software of 21 pairs of images, in which the code found a particle.

4.3 Custom Software for Particle Tracking Velocimetry (PTV)

Due to the low particle concentration in the experiments of the current work the method of Particle Tracking Velocimetry was implemented for the identification of the particles and the need for a custom code was indispensable. Crocker and Grier have described methods for tracking Brownian motion in a liquid phase [95] and developed a Particle Tracking Code in IDL [96], which was later translated into a Matlab version by Blair and Dufresne [97], and Kilfoil [98] respectively.

The code accomplishes the Particle Tracking in 5 basic stages:

        a. Image Restoration,

        b. Locating Particles,

        c. Refining Location Estimates,

        d. Noise Discrimination and Tracking in Depth,

        e. Linking Locations into Trajectories.

The stage of Image Restoration deals with the correction of imperfections of the individual image, which originate mostly by the sensor and circuitry of the digital camera. More specifically, the particles should look like bright spots on black background and thus a spatial bandpass filter is used to smooth the image and subtract the background. The bandpass filtering is achieved in two stages:

First, a lowpass filter is used by convolving the original image with a Gaussian kernel, where σ is the standard deviation of the Gaussian distribution and determines the degree of smoothing as shown in Figure 4.28. The equation of a Gaussian function in two dimensions is [99]:

$$G(i, j) = \frac{1}{2\pi\sigma^2} e^{-\frac{i^2+j^2}{2\sigma^2}} \tag{3.1}$$

In Eq. (3.1) the indices i and j range from 1 to 2048 and correspond to points in a matrix, which contains brightness intensity values as recorded by the CCD camera (24-bit sensor). The convolution is computed as

$$A_\sigma(x, y) = \frac{1}{B} \sum_{i,j=-w}^{w} A(x+i, y+j) e^{\left(-\frac{i^2+j^2}{4\sigma^2}\right)} \tag{3.2}$$

with normalization $B = B = \left[\sum_{i=-w}^{w} e^{\left(-\frac{i^2}{4\sigma^2} \right)} \right]^2$.
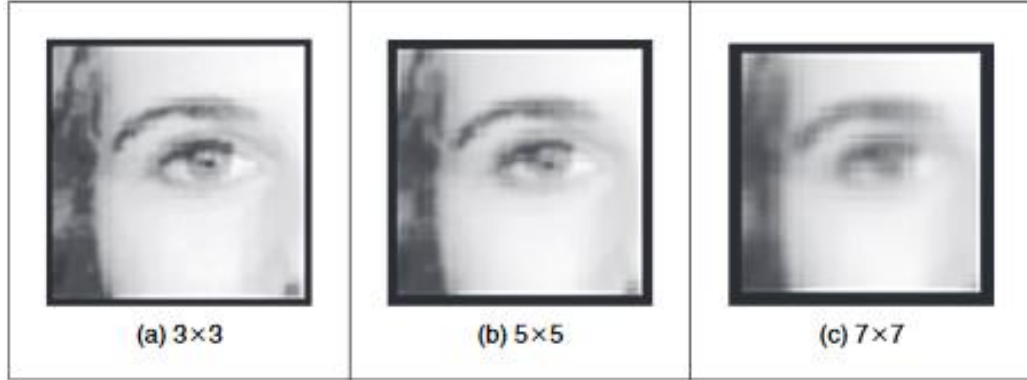
Figure 4.28: Application of Gaussian blurring by applying a (a) 3x3 kernel, (b) 5x5 kernel and (c) 7x7 kernel [92].

Next, a highpass filter is used for the removal of the noise in the background, by applying a boxcar average over a region of extend $2w+1$, where w is an integer larger than a single sphere's apparent radius in pixels, but smaller than an intersphere separation. The corresponding convolution is defined as

$$A_w(x, y) = \frac{1}{(2w+1)^2} \sum_{i,j=-w}^{w} A(x+i, y+j) \ . \tag{3.3}$$

An implementation of equations (3.2) and (3.3) in combination is achieved with the convolution kernel

$$K(i, j) = \frac{1}{K_0} \left[\frac{1}{B} e^{-\frac{i^2+j^2}{4\sigma^2}} - \frac{1}{(2w+1)^2} \right], \tag{3.4}$$

with normalization $K_0 = \frac{1}{B} \left[\sum_{i=-w}^{w} e^{\left(-\frac{i^2}{4\sigma^2} \right)} \right]^2 - \frac{B}{(2w+1)^2}$.

The locating of the particles is achieved by first identifying all the pixels in the image that are above a threshold, which is defined as the minimum brightness of a pixel that could be a maxima. The area within a distance w of each one of these local maxima is then

49

checked for brighter pixels. The local maxima that have no brighter pixels in their neighborhood are considered as candidate particle locations. The size of the particles is also taken into account and, when running experiments in Polydisperse mode, every area of 5x5 pixels of non-zero brightness is considered a particle. If multiple local maxima are found in this area, the code will keep only the brightest.

The centroid of the particle location estimates is then calculated to sub-pixel accuracy. The offset from a local maxima at (x, y) to the brightness-weighted centroid of the pixels in a region around (x, y) is calculated as

$$\begin{pmatrix} \varepsilon_x \\ \varepsilon_y \end{pmatrix} = \frac{1}{m_0} \sum_{i^2+j^2 \le w^2} \begin{pmatrix} i \\ j \end{pmatrix} A(x+i, y+j), \tag{3.5}$$

with $m_0 = \sum_{i^2+j^2 \le w^2} A(x+i, y+j)$ being the integrated brightness of the sphere's image.

Lastly, after removing the noise, comes the linking of the particle locations into trajectories. For each particle identified in the first image, all possible identifications of its position in that image with its new position in the second (successive) image are considered. Finally, the identification, which results in the minimal total squared displacement, is chosen and the trajectories are produced. The result is a list containing the original data rows sorted into a series of trajectories, which are then written to a text file in the form depicted in Table 2.

Table 2: The coordinates and the corresponding velocities outputted by the PTV code.

X location (pixels)	Y location (pixels)	Vx (pixels/us)	Vy (pixels/us)	V (pixels/us)

Fasmatech Science and Technology S.A. had developed and successfully used in previous experiments a PTV code in Matlab, which utilized the previous methodology, as developed by Blair and Dufresne [97]. The code worked efficiently for experiments of free jet expansion, but it was inapplicable for the experiments of this work. The Aerolens™ consists of glass and therefore the development of noise, especially at its boundaries, is favored, due to the laser reflections (Figure 4.29). As noise presents very similar characteristics with a particle, the code found difficulties distinguishing noise from

particles and thus it resulted in misleading trajectories or in the interruption of the software due to excessive combinatorics that encountered.
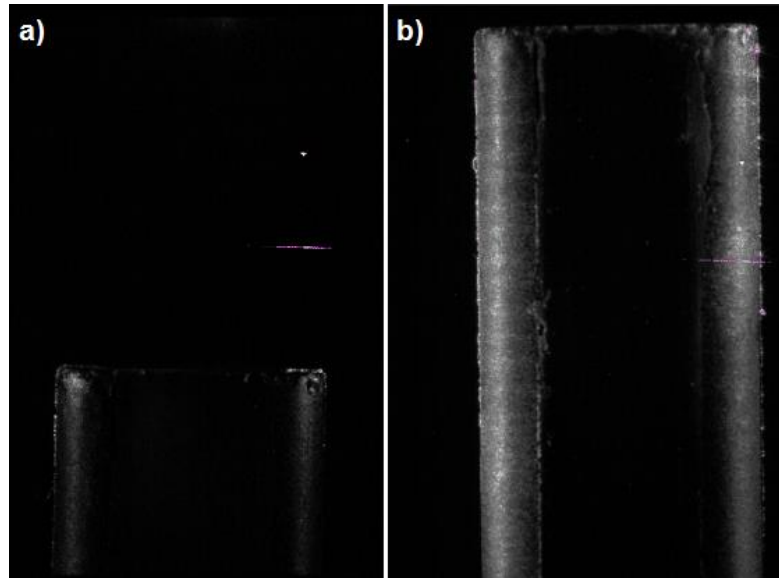
Figure 4.29: Image captured via 3G Insight software during experiments (a) at the exit of capillary and (b) at the entrance of Aerolens™.

The solution to this problem was to create a custom background image, which would only contain the noise developed by the laser reflections. This background image would be subtracted from every image being processed, thus leaving them with only the particles. The whole idea for the creation of the background image depended on the fact that a particle is almost impossible to be seen on exactly the same position more than once and that the noise is repeatedly observed at specific regions. That means, that if a local maxima (possible a particle) is found twice at the exact same position, then it is not a particle but noise.

For the better understanding of the details that will be explained next, it is mentioned that Matlab perceives a greyscale image (also known as monochrome or black-and-white image) as a data matrix, whose values represent the pixel intensity of the image (Figure 4.30). The values range from 0 (total black) to 255 (white), thus allowing the representation of 256 shades of gray.
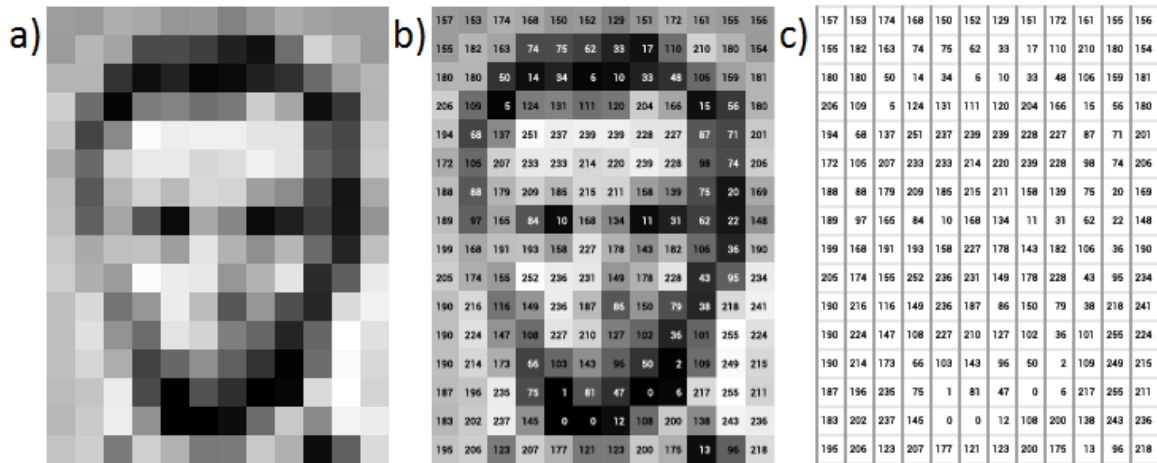
Figure 4.30: A greyscale image (a), combined with its light intensity values (b) and the intensity values by themselves in a matrix (c) [100].

The procedure for the creation of the background image is as following: at first, the background image is totally black (all pixels have zero intensity values) and some pair of images are investigated for local maxima using the methods for Image Restoration and for Locating Particles that are mentioned above. Every time a local maxima is found in any of them, the value of that specific pixel is increased by 1:

$$background\_image(i, j) = background\_image(i, j) + 1;$$

In the end, the background image will contain pixel values ranging from 0 to the number of the pair of images processed (e.g. intensity values between 0 and 1000, if 1000 pairs of images were investigated for local maxima). The resulted image gives valuable information for 3 cases:

-If a pixel has value 0, then there is no noise or particle in that position in any of the images investigated.

-If a pixel has value 1, then there is a particle in that position in one of the images investigated.

-If a pixel has value > 1, then that is noise and not a particle, as it is impossible for a particle to be found twice on exactly the same position.

Therefore, all the pixels with value > 1, consist the background image, which will be deleted from every image through processing in the main PTV code.

52

It is obvious that the greater the amount of images used for the creation of the background image, the more detailed the mapping of the noise will be, as it is demonstrated in Figure 31. The walls of Aerolens^{TM} were cropped in order for the code to run faster, as it is impossible for a particle to be located there.
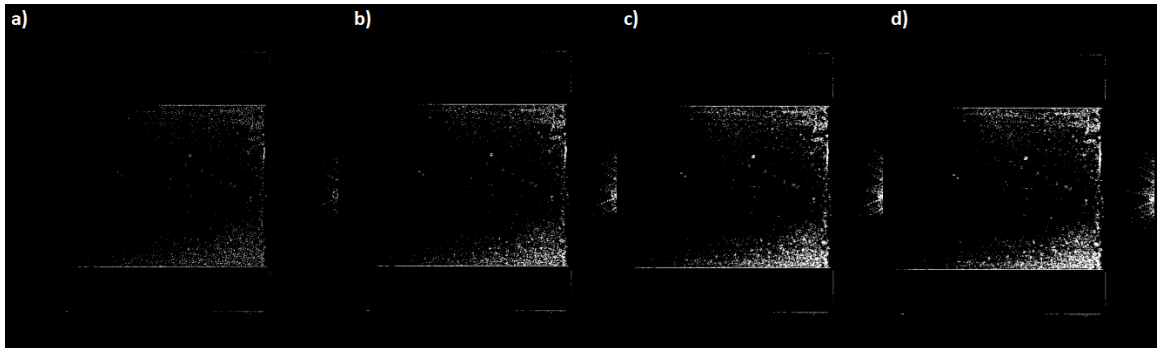
Figure 4.31: Resulted background image using (a) 500, (b) 2500, (c) 5000 and (d) 7500 images respectively, in which both the entrance of Aerolens^{TM} and the exit of capillary are shown.

However, an excessive use of images could result in deleting a great amount of pixels and as a result, getting valuable information from noisy areas, such as near the walls of Aerolens^{TM} or near the capillary is hindered. Finally, the ideal number of images that should be used for the creation of the background image is not fixed and it should be selected depending on the experimental conditions and the noise that is present.

Aiming to the more accurate identification of the particles, two additional processes have been implemented:

-In order to accept a local maxima as a particle, it is required that all pixels inside a radius of 2 pixels from its local maxima are non-zero.

-When the background image is deleted from every image, it is not deleted only the one pixel with value >1, but also the other 8 pixels around it (radius of 1).

Considering that a particle covers a much bigger area (Figure 4.32), it is believed that no valuable information is lost during this procedure.
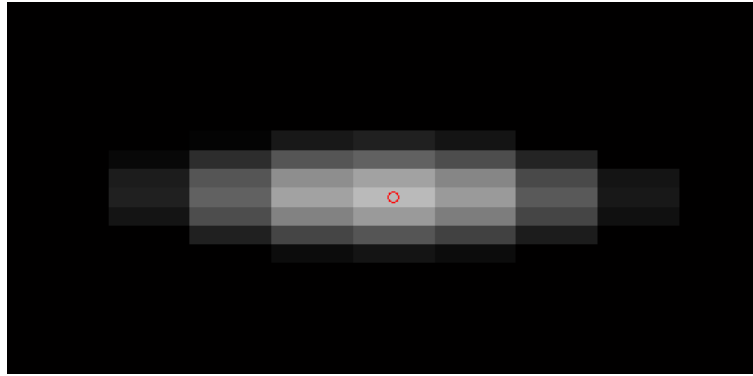
Figure 4.32: Zoomed-in picture of a particle found in an image.

The flowchart of the code for the creation of the background image for each image, as well as the flowchart of the main PTV code are presented in the diagrams in Figures 4.33 and 4.34 respectively.
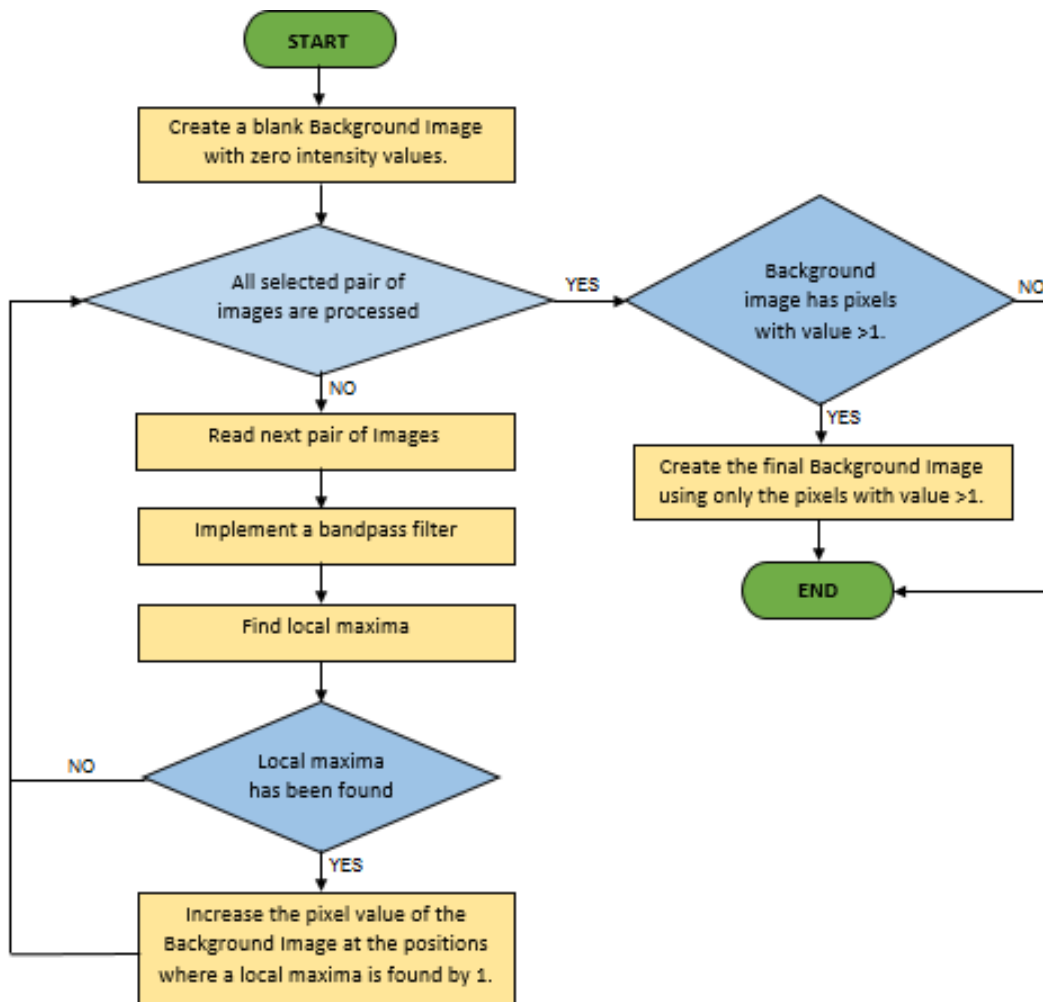
Figure 4.33: Flowchart of the creation of the background image.

54
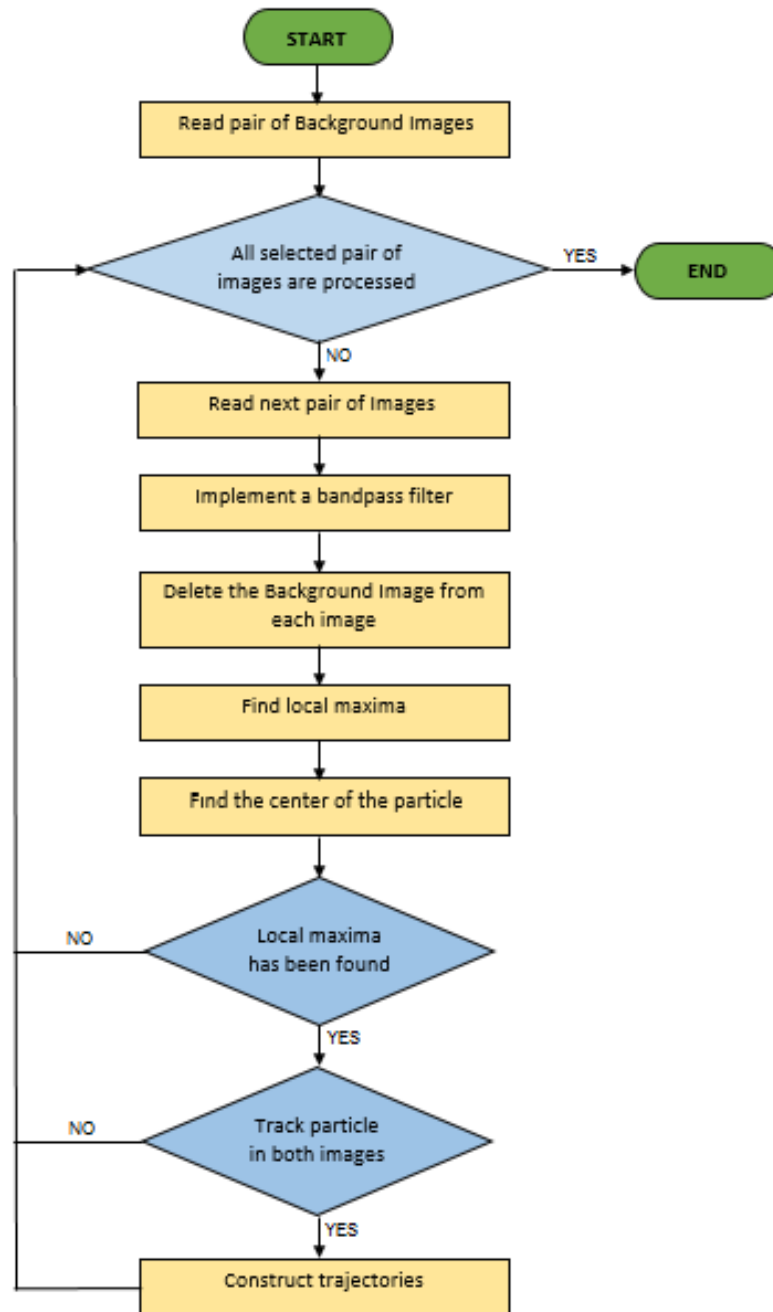
Figure 4.34: Flowchart of the main PTV code.

The resulted text file contains the trajectories in pixels and thus they need to be converted into mm before creating the final vector map. The pixel to mm calibration is achieved by using the known dimension in mm (Figure 4.35) in conjunction with the corresponding number of pixels.

More specifically, it was taken into consideration:

      a. the capillary's external diameter,

      b. the width of Aerolens^{TM} and

c. the known distance between the capillary's exit and the entrance of Aerolens™.
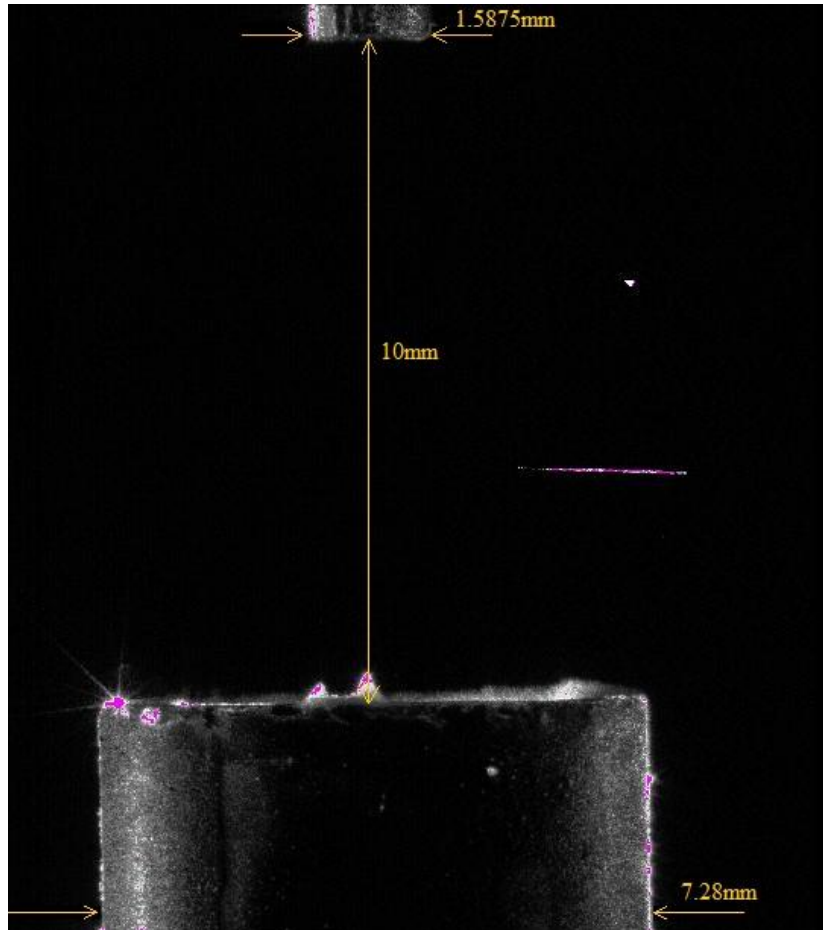
Figure 4.35: Known distances used to calibrate pixels to mm.

The PTV code can be found in Appendix A.

Chapter 5:

Experimental Results

5.1 SMPS Results

In the following Figures (Figure 5.1 - Figure 5.5) the voltage, frequency and particle concentration for various combinations Capacitor-Wiring are presented. The results show that the more resistive the mode, the particle distributions tend to become more monodisperse, with reduced particle size and concentration.

• **10 nF Capacitor –Wiring 1:**
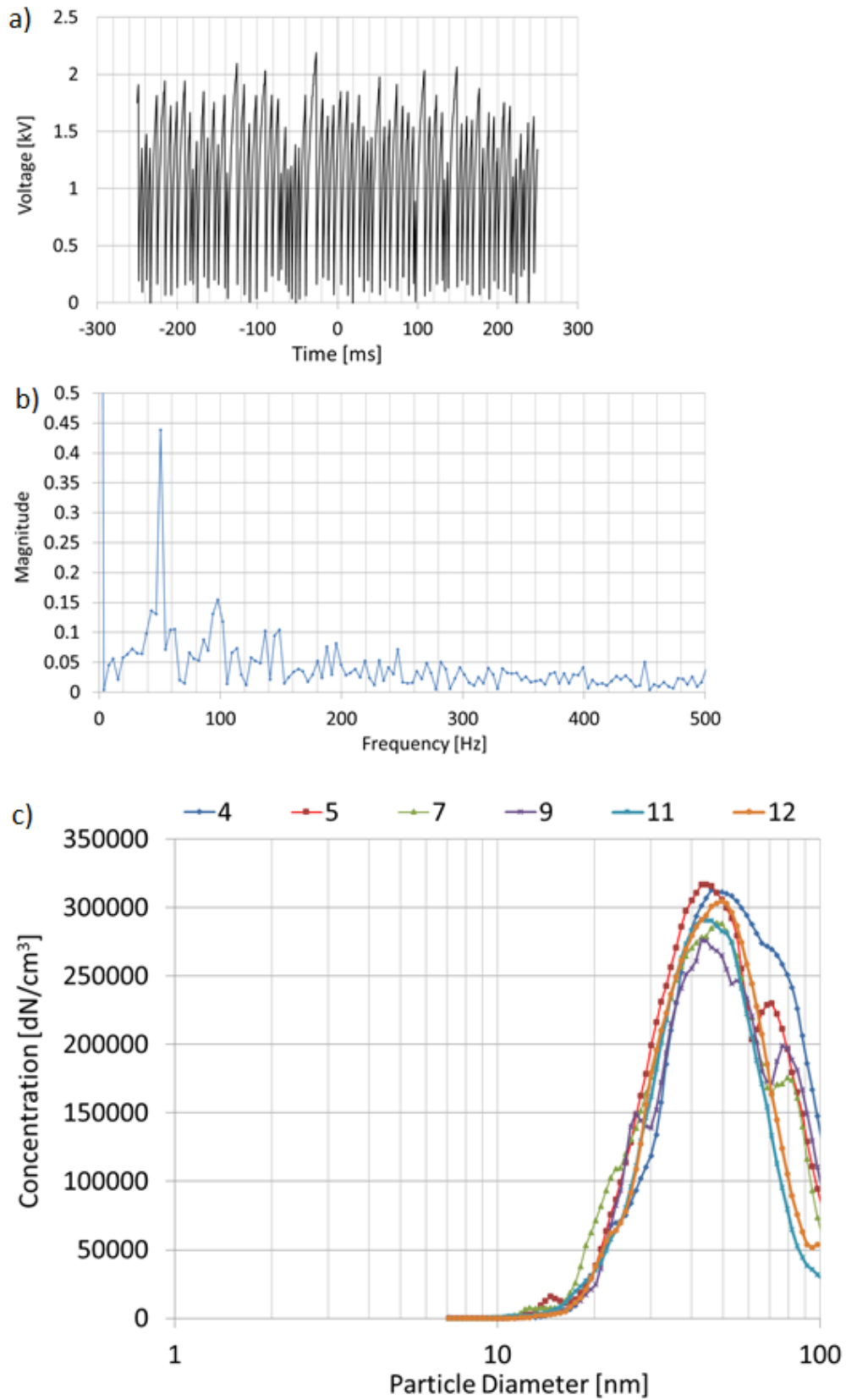
Figure 5.1: The voltage trace on oscilloscope (a), the frequency spectrum (b), and the particle concentration (c) for the Free Spark mode using a 10 nF capacitor.

58

• **10 nF Capacitor –Wiring 2:**

Figure 5.2: The voltage trace on oscilloscope (a), the frequency spectrum (b), and the particle concentration (c) for the Resistive Spark mode (R1=82 kΩ) using a 10 nF capacitor.

• **10 nF Capacitor –Wiring 3:**
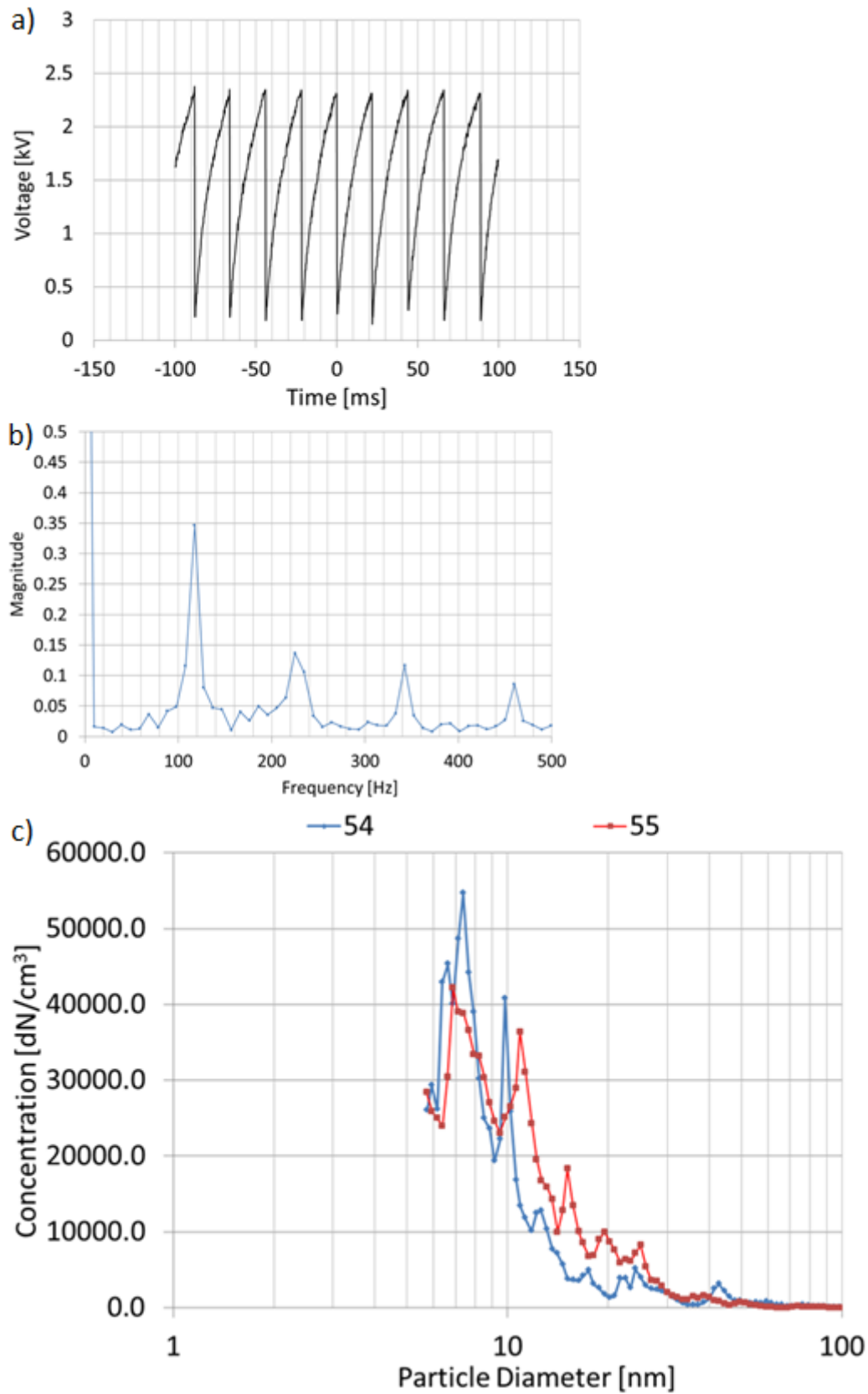
Figure 5.3: The voltage trace on oscilloscope (a), the frequency spectrum (b), and the particle concentration (c) for the Resistive Spark mode (R2=470 Ω) using a 10 nF capacitor.

• <u>2.5 nF Capacitor –Wiring 1:</u>
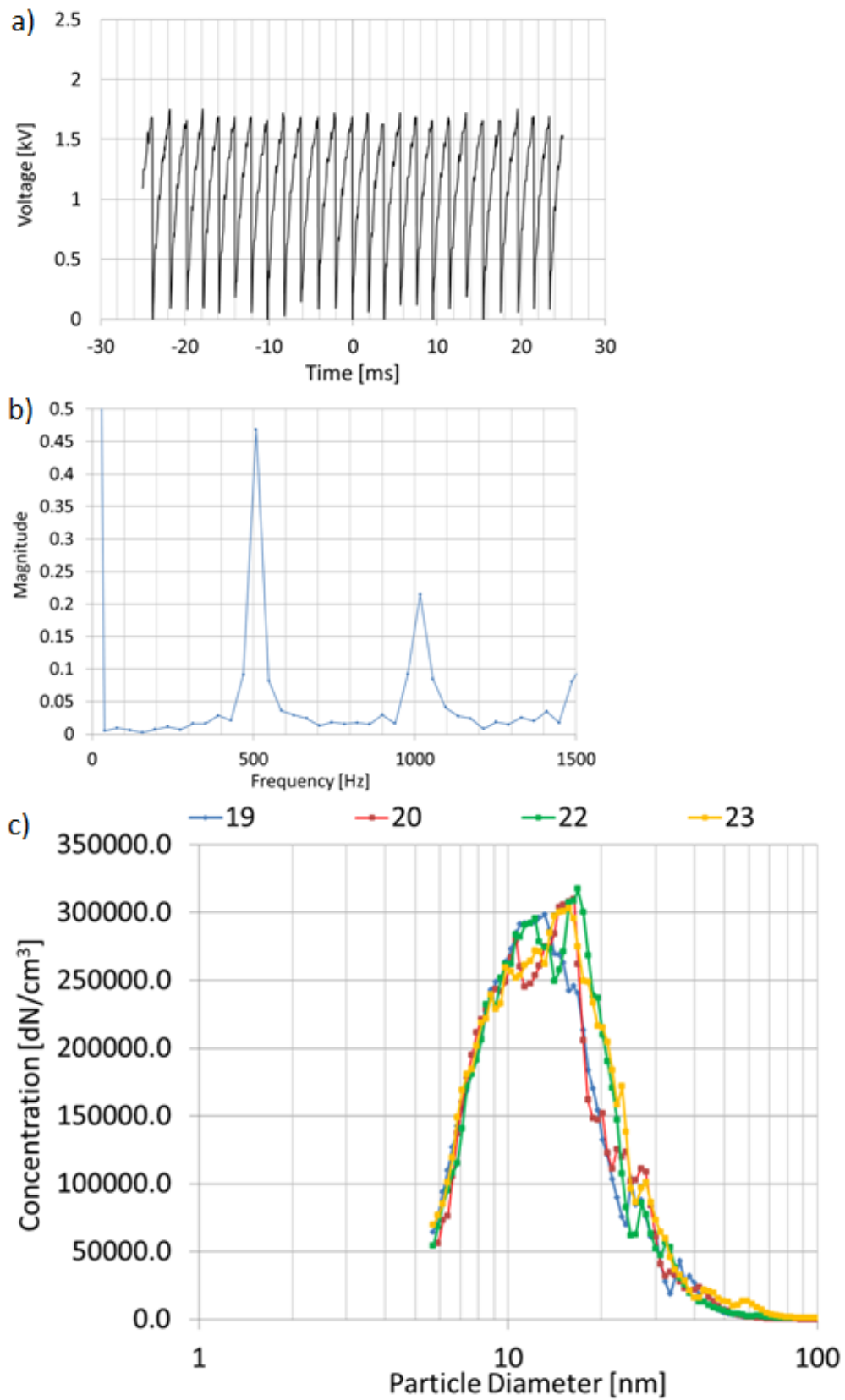
Figure 5.4: The voltage trace on oscilloscope (a), the frequency spectrum (b), and the particle concentration (c) for the Free Spark mode using a 2.5 nF capacitor.

• **2.5nF Capacitor –Wiring 2:**
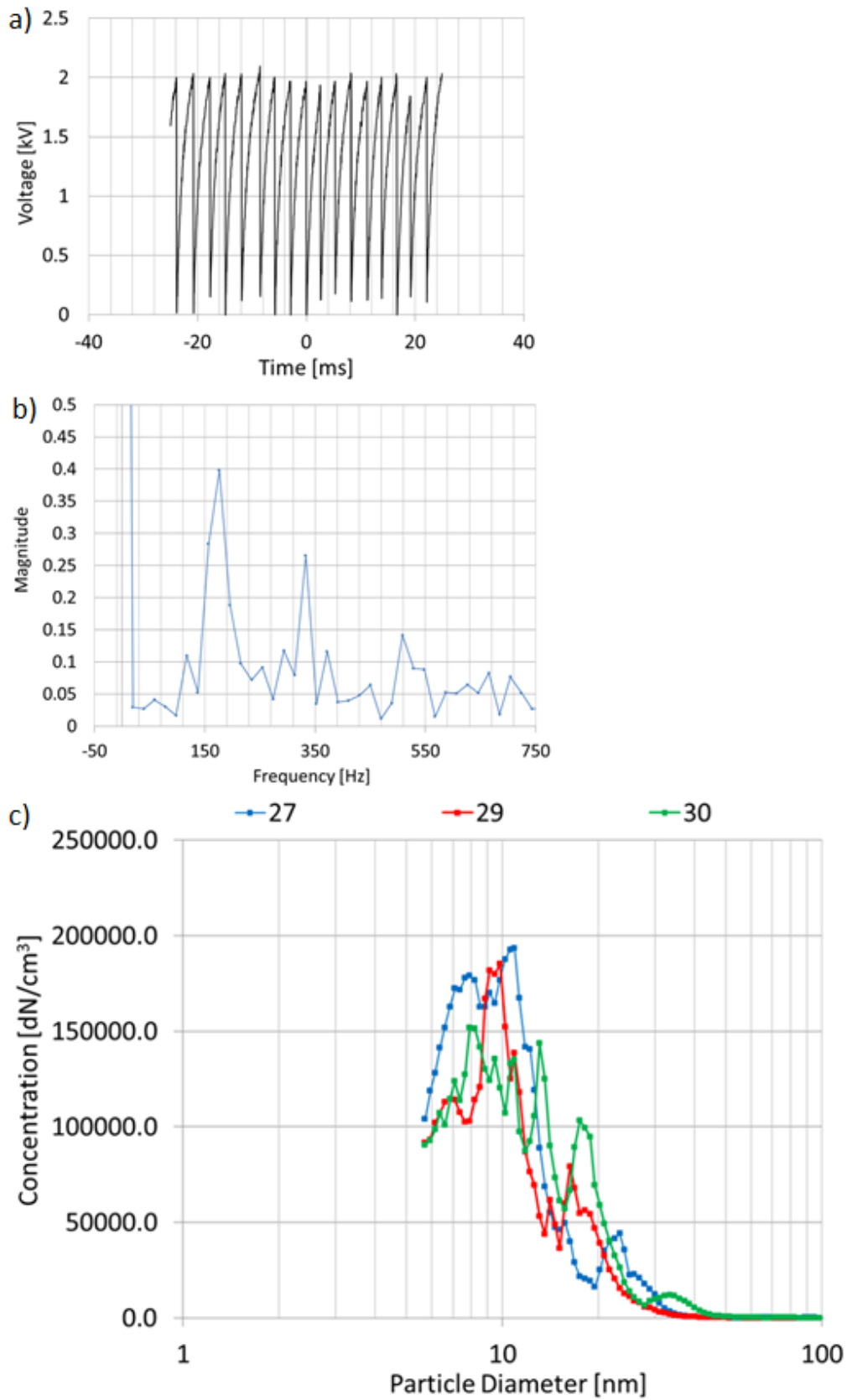
Figure 5.5: The voltage trace on oscilloscope (a), the frequency spectrum (b), and the particle concentration (c) for the Resistive Spark mode (R1=82 kΩ) using a 2.5 nF capacitor.

5.2 PTV Results

The structure of the jet inside the first vacuum chamber is investigated over two pressure ranges, 20 and 5 mbar respectively, using Al_2O_3 particles generated by the Spark Discharge Source. These experiments were conducted on the Polydisperse mode with the tail of the distribution decaying at ~100 nm, as previously demonstrated in Figure 5.1.

More specifically, in subsections 5.2.1 and 5.2.2 the results of an expansion inside Aerolens^{TM} are presented for 20 and 5 mbar respectively, for the first 24 mm downstream the capillary exit, for the far-field region ~63 mm downstream and at the exit of Aerolens^{TM}.

In subsection 5.2.3 the results of a free jet expansion at 20 mbar pressure are presented for the first 24 mm downstream the capillary exit.

Finally, in subsection 5.2.4 the applicability of the Electrospray Ionization Source using 100 nm fluorescent particles was tested and results for the corresponding flow field are presented.

5.2.1 Expansion into Aerolens^{TM} at 20 mbar pressure using Al_2O_3 particles

The Aerolens^{TM} is installed 9.6 mm downstream the capillary exit. PTV experimental results are obtained at the outlet of the capillary, the entrance of the channel, ~63 mm downstream and at a few mm downstream the exit of the 100 mm duct.

Figure 5.6 shows the formation of the jet discharging into the bore of the Aerolens^{TM} obtained experimentally (a) and computationally (b). The barrel shock, the formation of a Mach disk a few mm downstream the capillary exit, followed by the silent zone, as well as the jet boundaries are clearly depicted in the experimental data.
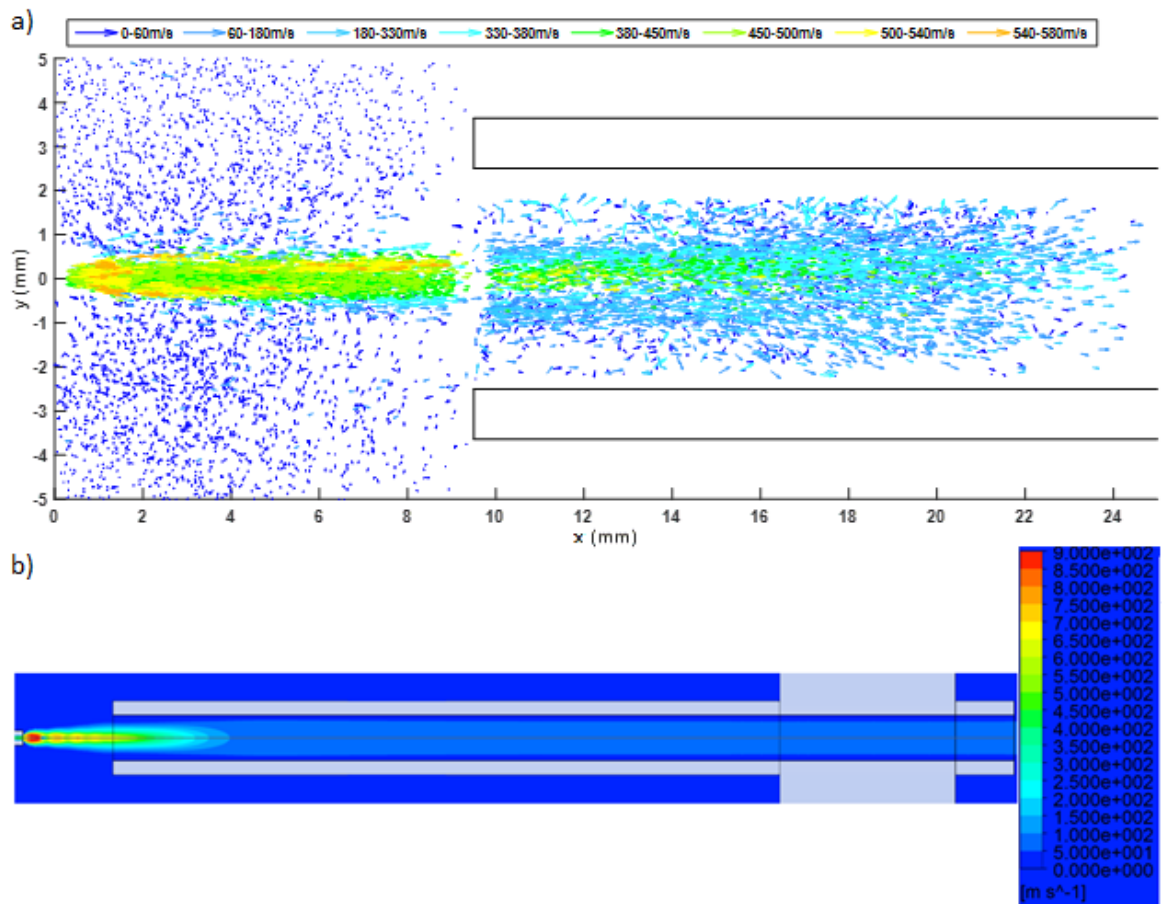
Figure 5.6: Expansion inside Aerolens^{TM} at 20 mbar pressure for experimental (a) and computational (b) results, respectively.

The axial velocity obtained with CFD calculations in comparison with the velocity vector field obtained experimentally is plotted over the axial distance in Figure 5.7. In the near field region, the velocity of the PTV data disagrees significantly with the calculated one, proving that the relaxation time of the Polydisperse mode is not low enough to follow the velocity fluctuations and illustrate the diamond-shock pattern. In the far-field region of the jet, the velocity decays progressively as demonstrated by the computational tool, however, there is clear deviation in velocity.
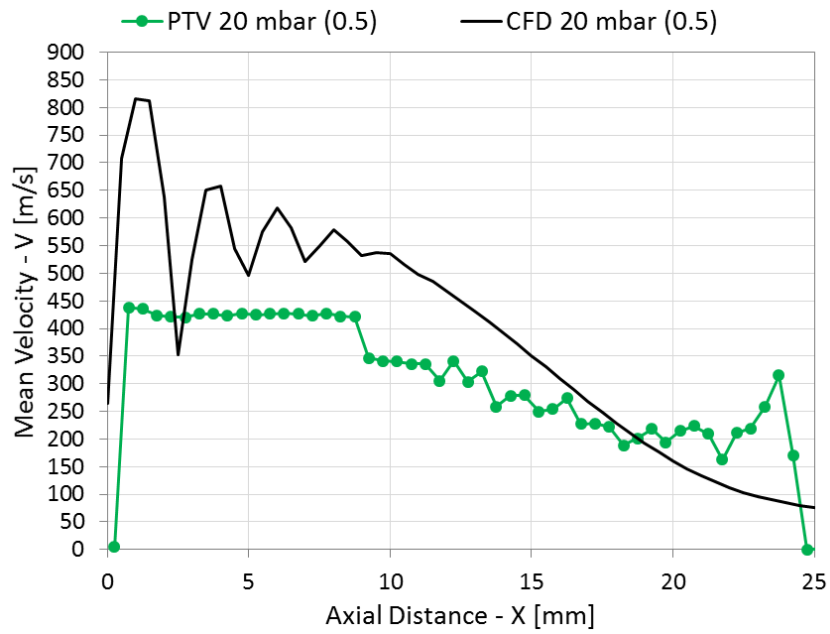
Figure 5.7: Axial velocity profile of the under-expanded jet at 20 mbar pressure.

Further investigation of the under-expanded jet is presented in Figure 5.8 and Figure 5.9, where the PTV velocity measurements are plotted over the radial distance. In Figure 5.9 the interaction of the jet with the wall boundaries of Aerolens^{TM} becomes visible and the flow starts decelerating.
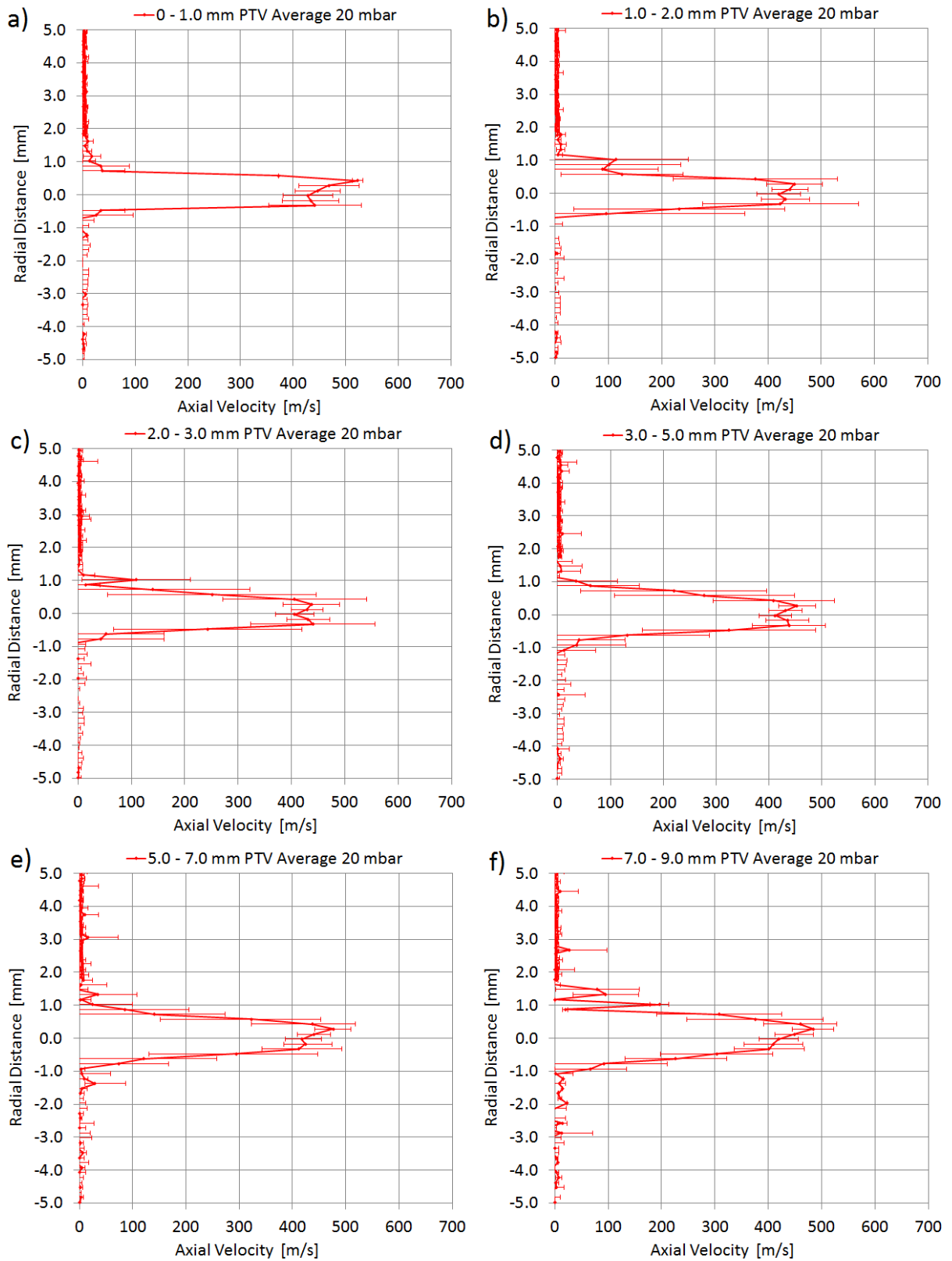
Figure 5.8: Radial velocity profiles of the under-expanded jet at 20 mbar pressure for the first 9 mm downstream the capillary exit.

66
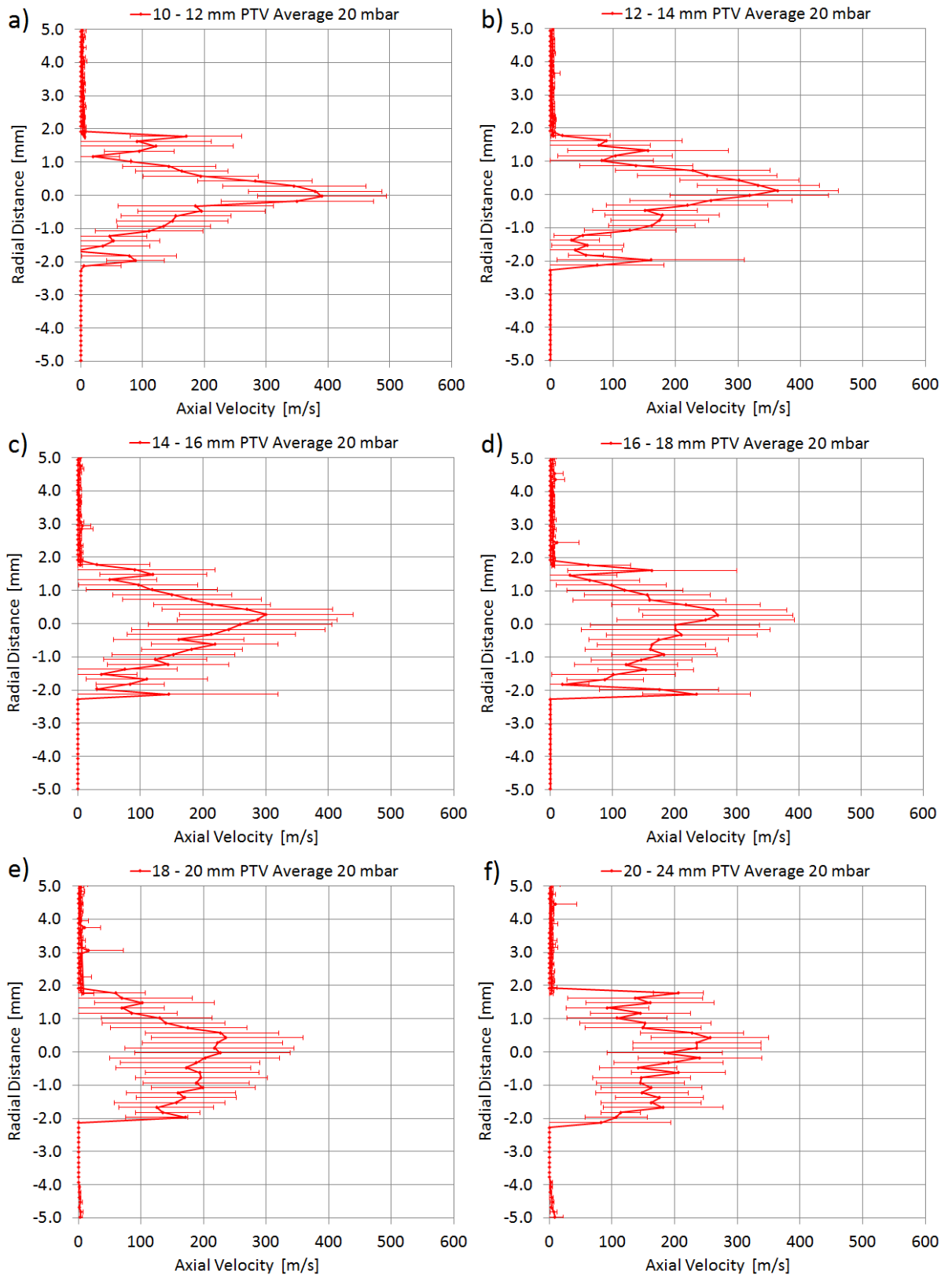
Figure 5.9: Radial velocity profile of the under-expanded jet at 20 mbar pressure at 10 mm - 24 mm downstream the capillary exit.

Further downstream inside the Aerolens^TM the flow has decelerated to velocities <100 m/s and has transformed to unsteady laminar, as shown in Figure 5.10 and Figure 5.11 (a-c). The measured flow is characterized by wide error bars.
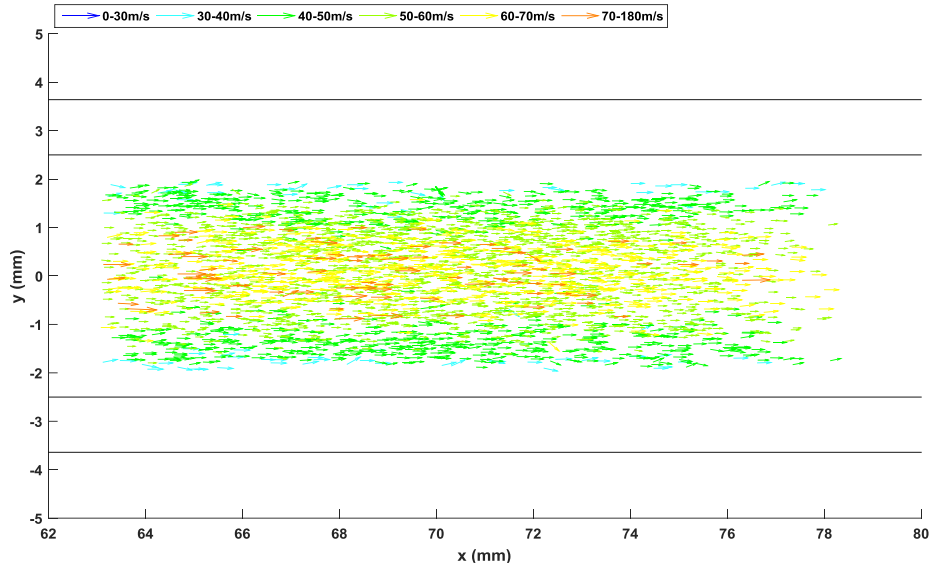
Figure 5.10: Visualization of the flow field at 20 mbar pressure 63 mm downstream the capillary exit.
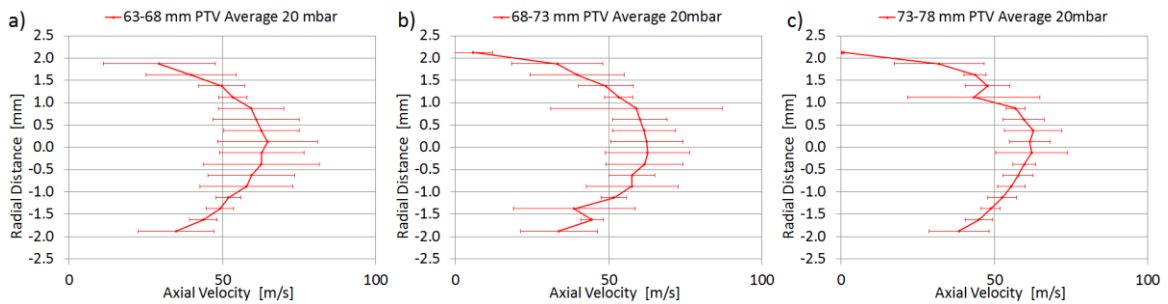
Figure 5.11: Radial velocity profiles of the under-expanded jet at 20 mbar pressure at 63 mm - 78 mm downstream the capillary exit.

Finally, the fully developed laminar flow, established a few mm downstream the Aerolens^TM exit is presented in Figure 5.12 and Figure 5.13 (a-c), where the velocity of the gas has a parabolic profile of less than 50 m/s.
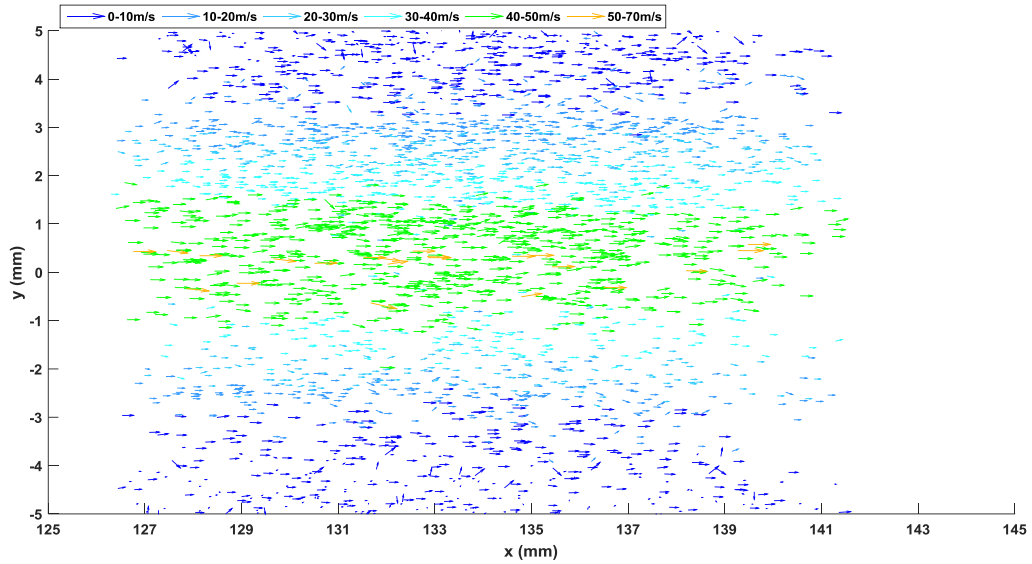
Figure 5.12: Visualization of the flow field at 20 mbar pressure 126 mm downstream the capillary exit.
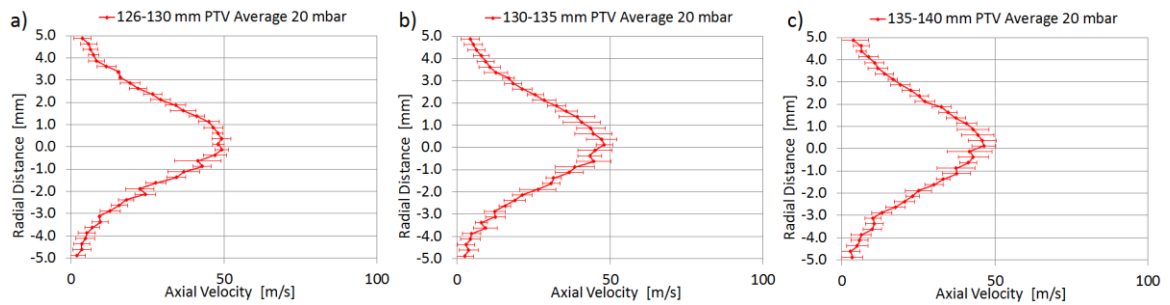
Figure 5.13: Radial velocity profiles of the under-expanded jet at 20 mbar pressure at 126 mm - 140 mm downstream the capillary exit.

5.2.2 *Expansion into Aerolens^{TM} at 5 mbar pressure using* Al_2O_3 *particles*

The Aerolens^{TM} is installed 8.7 mm downstream the capillary exit. PTV experimental results are obtained at the outlet of the capillary, the entrance of the channel, ~63 mm downstream and at a few mm downstream the exit of the 100 mm duct.

Figure 5.14 shows the formation of the jet discharging into the bore of the Aerolens^{TM} obtained experimentally (a) and computationally (b). The barrel shock, the formation of a Mach disk a few mm downstream the capillary exit, followed by the silent zone, are clearly observed in the experimental data. The jet boundaries, especially on the upper side, are not fully visualized, as fewer particles were captured at those positions. It is obvious that the jet enters the Aerolens^{TM} with a slight inclination, due to the fact that the jet is not completely aligned to the capillary's outlet.
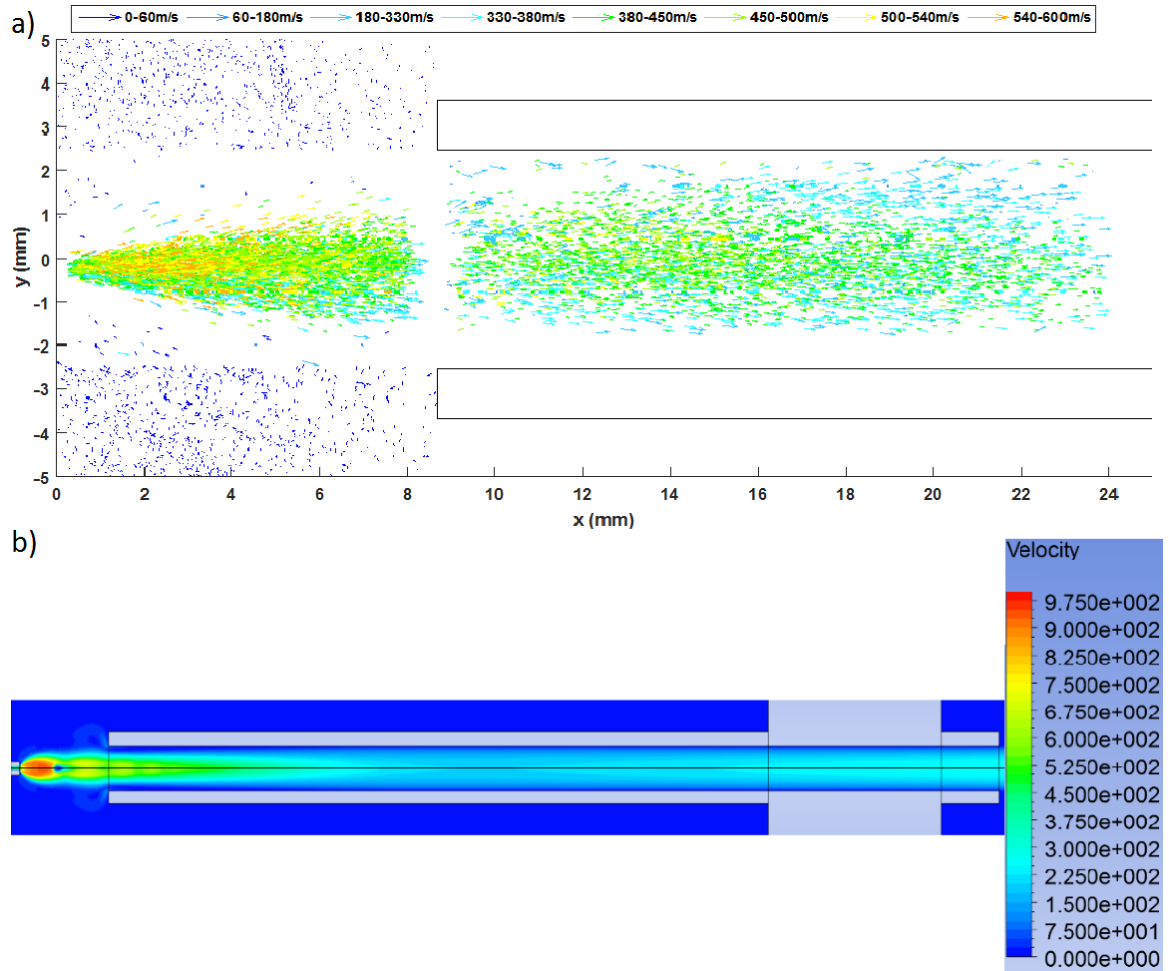
Figure 5.14: Expansion inside Aerolens™ at 5 mbar pressure for experimental (a) and computational (b) results respectively.

The axial velocity obtained with CFD calculations in comparison with the velocity vector field obtained experimentally is plotted over the axial distance in Figure 5.15. In the near field region the velocity of the PTV data varies significantly from the calculated one, proving that the relaxation time of the Polydisperse mode is not low enough to follow the velocity fluctuations and illustrate the diamond-shock pattern. Even in the far-field region of the jet, there is a clear deviation between the CFD and the experimental data with the experimental velocity being greater than 370 m/s.
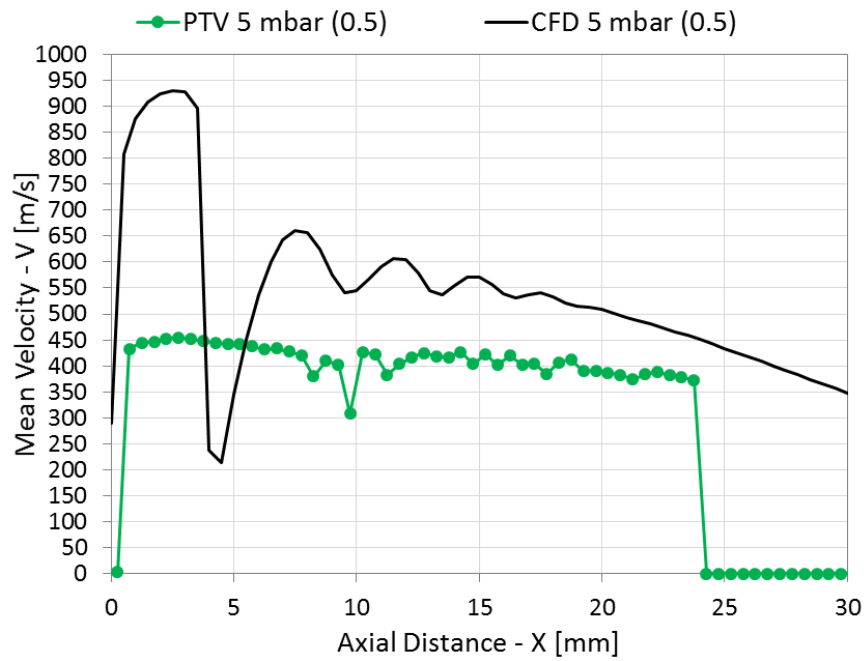
Figure 5.15: Axial velocity profile of the under-expanded jet at 5 mbar pressure.

Further investigation of the under-expanded jet is presented in Figure 5.16 and Figure 5.17, where the PTV velocity measurements are plotted over the radial distance. In Figure 5.17 (a-f) the interaction of the jet with the wall boundaries of Aerolens^{TM} becomes visible and the flow starts decelerating.

71
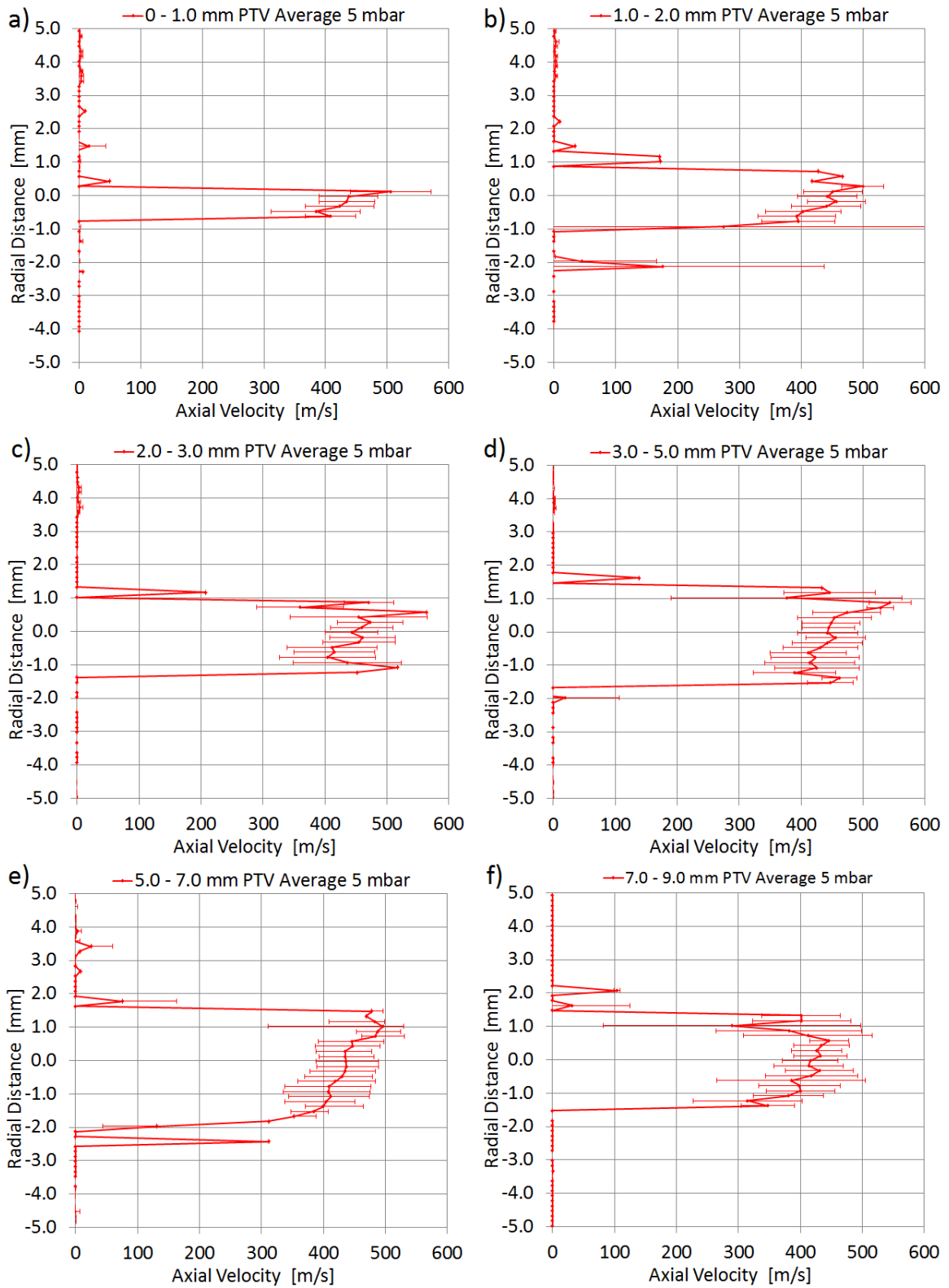
Figure 5.16: Radial velocity profiles of the under-expanded jet at 5 mbar pressure for the first 9 mm downstream the capillary exit.

72
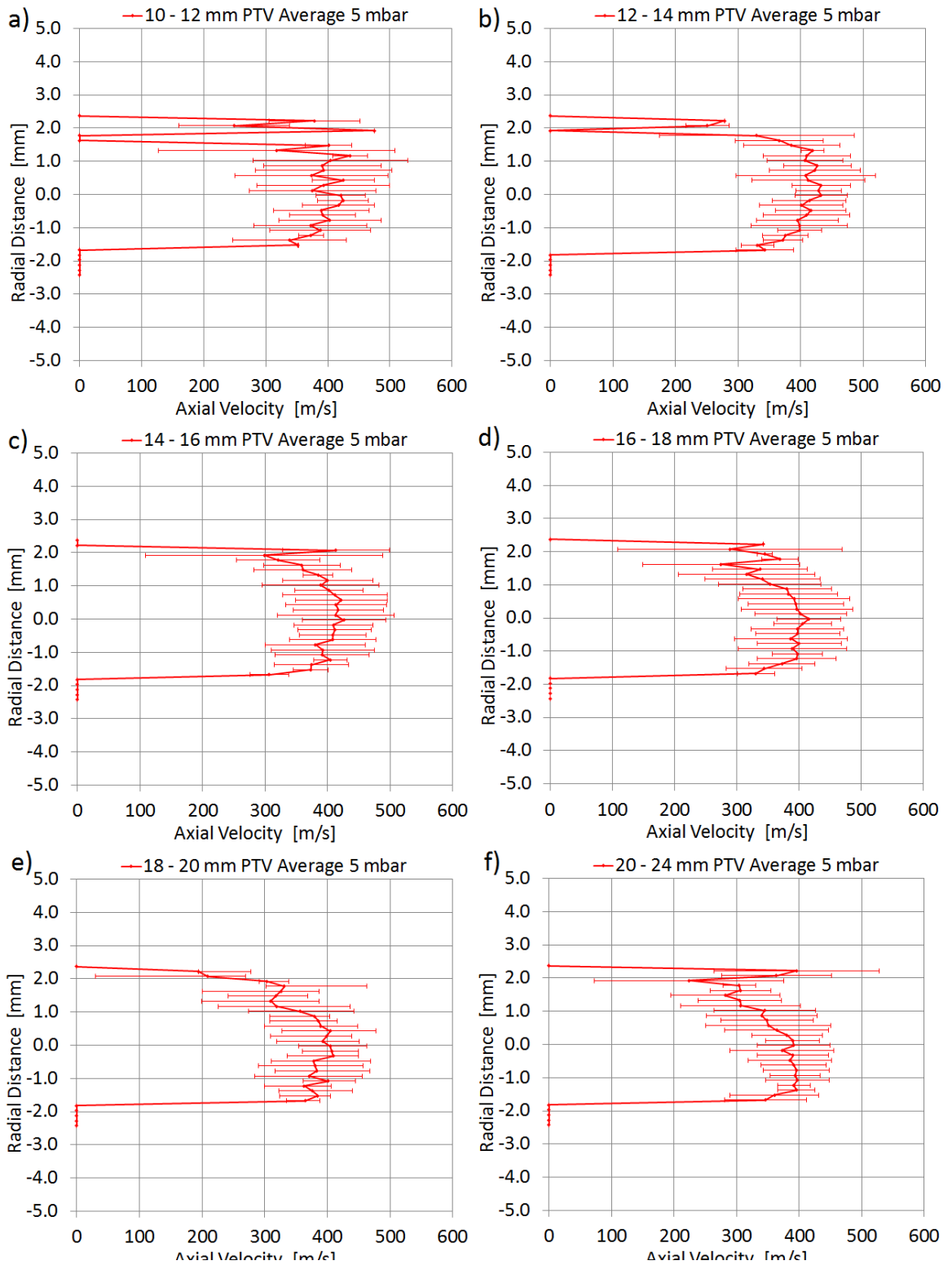
Figure 5.17: Radial velocity profile of the under-expanded jet at 5 mbar pressure at 10 mm - 24mm downstream the capillary exit.

Further downstream inside Aerolens[TM] the flow has deaccelerated to velocities less than 200 m/s and has transformed to unsteady laminar, as shown in Figure 5.18 and Figure 5.19 (a – c). The flow is characterized by wide error bars.

73
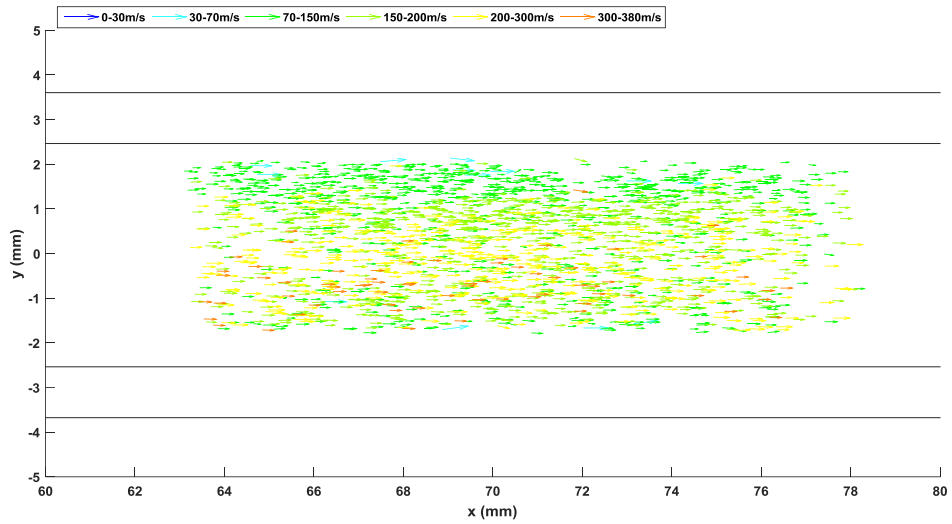
Figure 5.18: Visualization of the flow field at 5 mbar pressure 63 mm downstream the capillary exit.
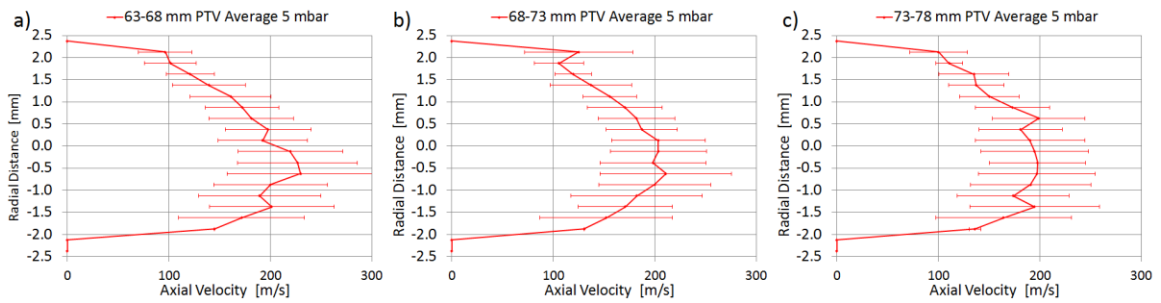
Figure 5.19: Radial velocity profile of the under-expanded jet at 5 mbar pressure at 63 mm – 78 mm downstream the capillary exit.

Finally, the transitional and turbulent character of the flow is suppressed and a fully laminarized flow with a near-parabolic velocity profile of less than 200m/s is presented in Figure 5.20 and Figure 5.21 (a-c).
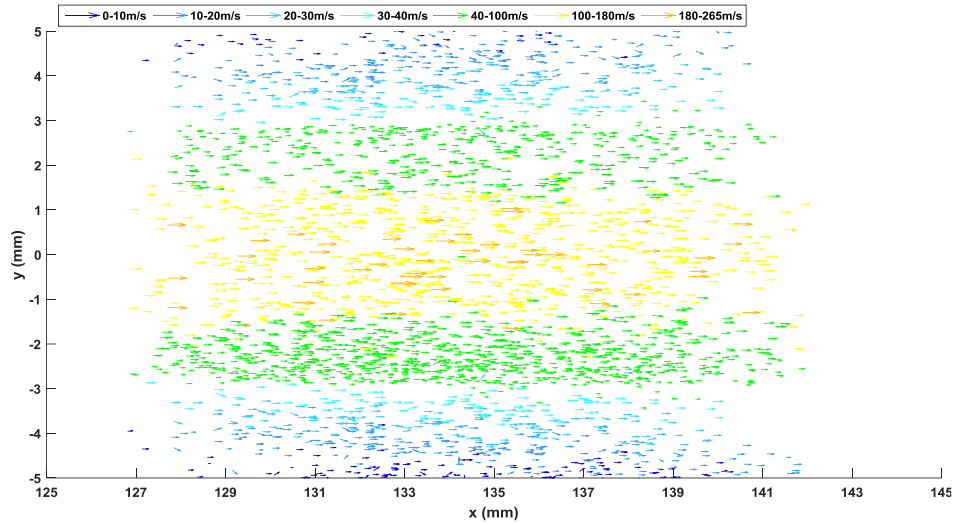
Figure 5.20: Visualization of the flow field at 5 mbar pressure 126 mm downstream the capillary exit.
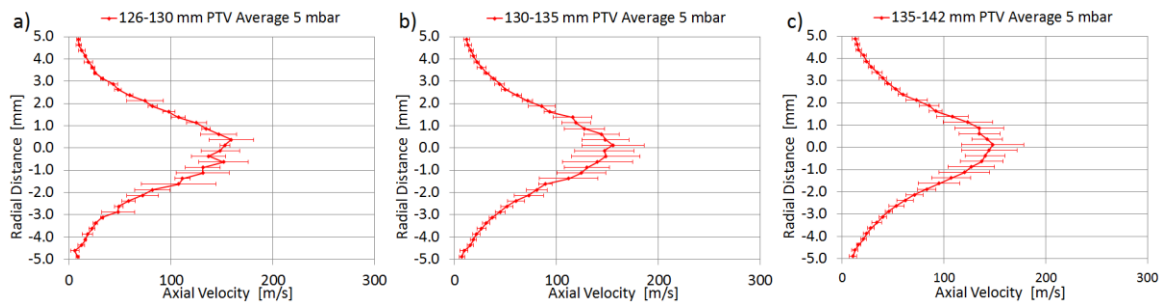
Figure 5.21: Radial velocity profile of the under-expanded jet at 5 mbar pressure at 126 mm – 142 mm downstream the capillary exit.

5.2.3 Free Jet Expansion at 20 mbar pressure using Al_2O_3 particles

PTV experimental results are obtained at the outlet of the capillary for the first ~30mm. Figure 5.22 shows the formation of the jet discharging into the bore of the Aerolens[TM] obtained experimentally (a) and computationally (b). The barrel shock, the formation of a Mach disk a few mm downstream the capillary exit, followed by the silent zone, as well as the jet boundaries are clearly observed in the experimental data.
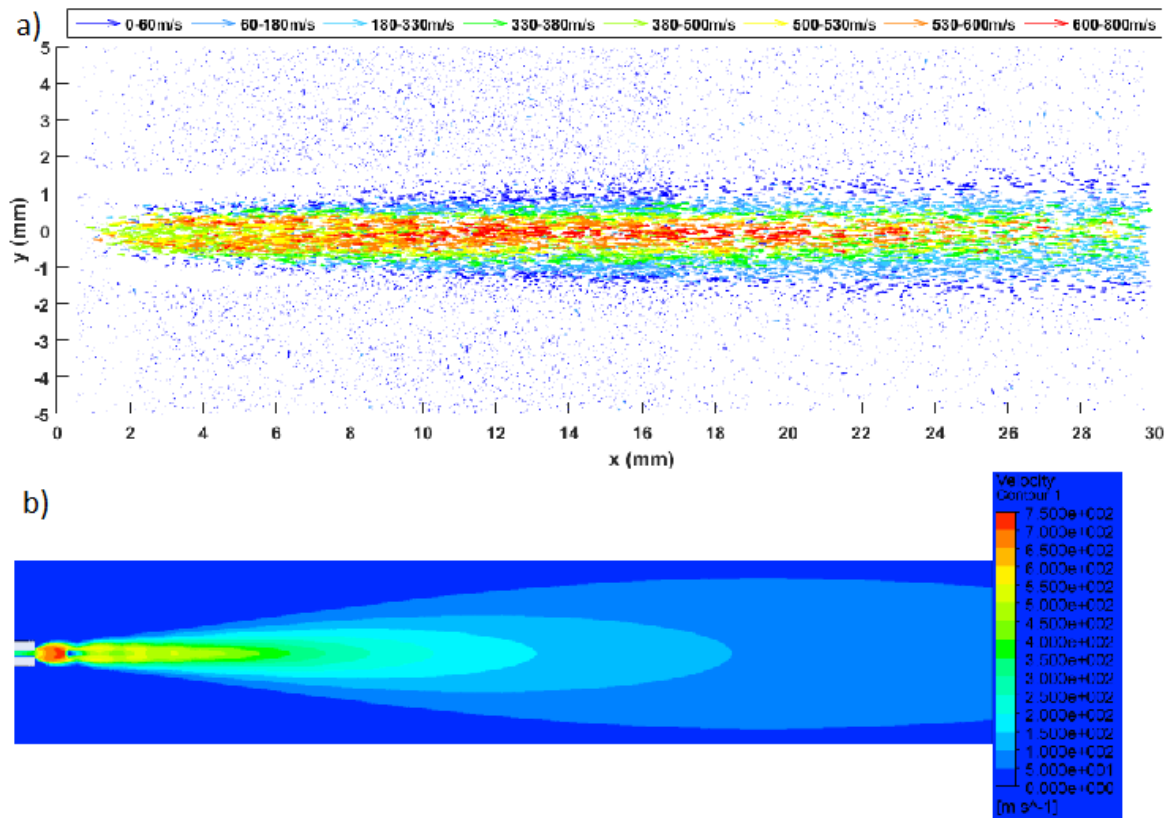
Figure 5.22: Free jet expansion at 20 mbar pressure for experimental (a) and computational (b) results respectively.

The axial velocity obtained with CFD calculations in comparison with the velocity vector field obtained experimentally is plotted over the axial distance in Figure 5.23. In the first 2mm the supersonic region of the jet wasn't captured and thus there is not data to compare. However, in the next few mm the velocity of the PTV data differs slightly from the computational calculations. In the far-field region of the jet, the velocity was expected to decay, but a further acceleration of the flow is displayed instead.
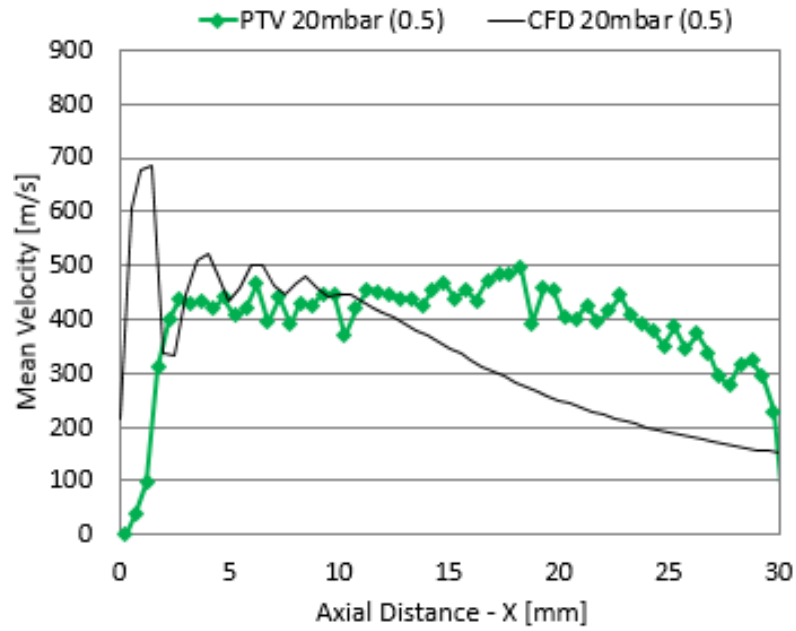
Figure 5.23: Axial velocity profile of the under-expanded jet at 20 mbar pressure.

Further investigation of the under-expanded jet is presented in Figure 5.24(a-f), where the PTV data is plotted over the radial distance.
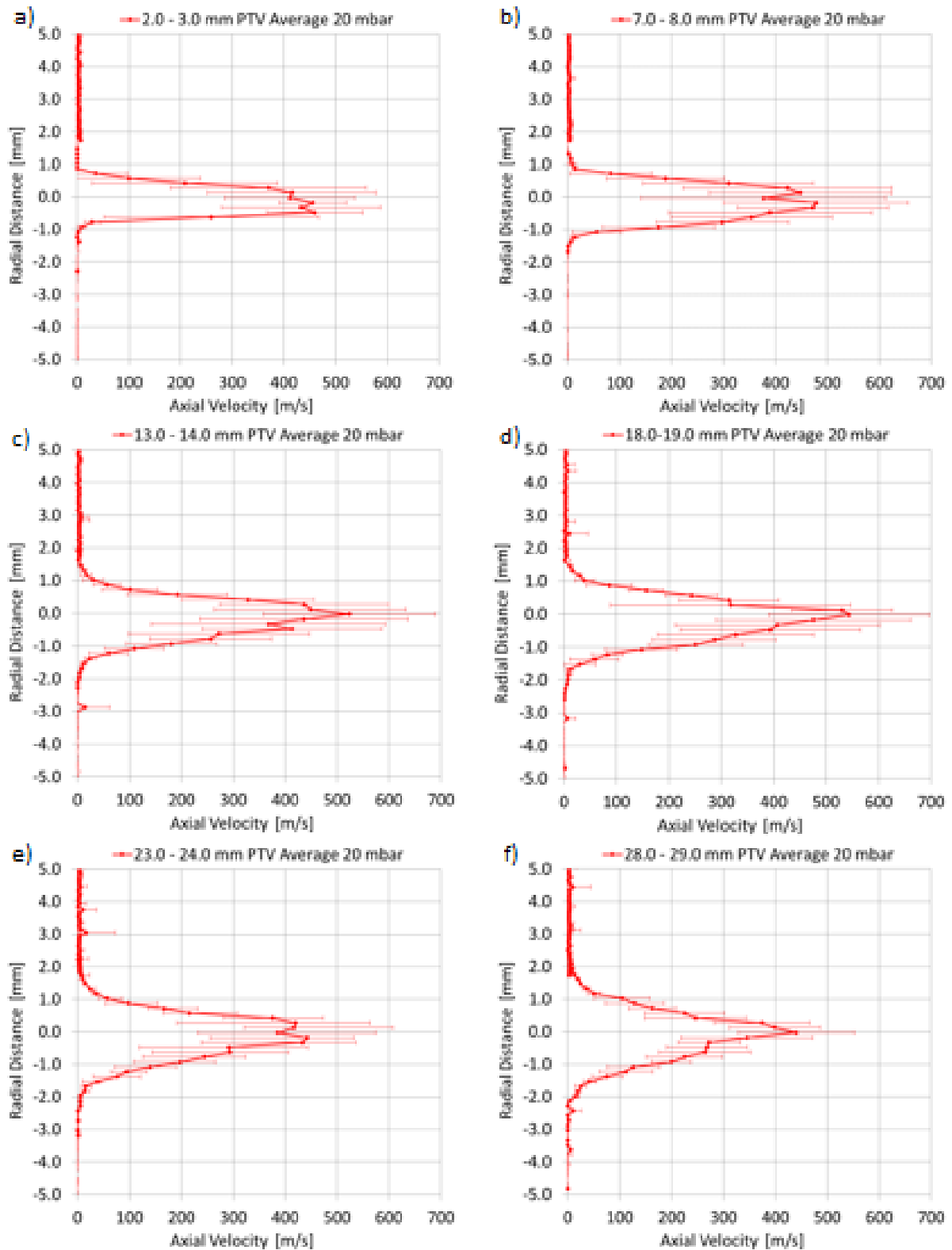
Figure 5.24: Radial velocity profile of the under-expanded jet at 20 mbar pressure for the first 29 mm downstream the capillary exit.

5.2.4   Free Jet Expansion at 20 mbar pressure using fluorescent particles

PTV experimental results are obtained 5 mm downstream the capillary exit using an Electrospray Ionization Source at 20 mbar pressure. Figure 5.25 shows a comparison between the flow field in which fluorescent particles were used and the flow field presented in subsection 5.2.3, in which Al_2O_3 particles were employed. The velocity of the latter particles is obviously lower, which can be attributed to the larger particle size (~100 nm).
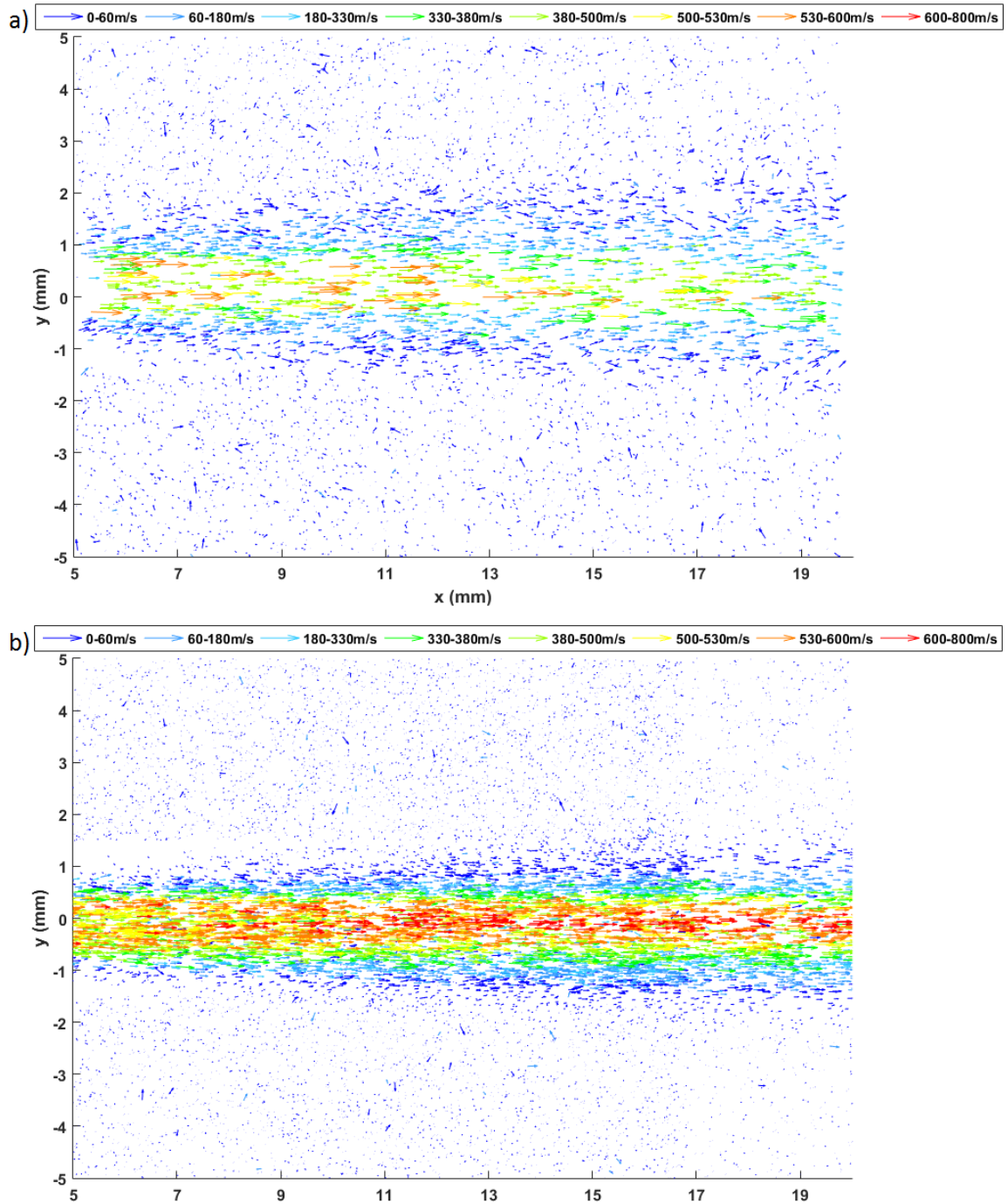
Figure 5.25: Flow field 5 mm downstream a free jet expansion using 100 nm fluorescent particles (a) and Al_2O_3 particles (b) respectively.

Chapter 6: Discussion

Even though the properties of the flow in the first few mm between the expansion inside Aerolens^{TM} and the Free Jet expansion at 20 mbar was expected to be identical, the velocity of the latter was significantly higher. An additional acceleration of the flow downstream the silent zone reaching velocities up to ~800 m/s was also demonstrated, which was not observed when the jet expanded inside the Aerolens^{TM}. This is attributed to the fact that when Aerolens^{TM} is implemented in the experiments the laser operates on low power, due to the high reflections of the glass channel. On the other hand, the Free Jet expansion experiments were achieved on high laser power, which probably results in the illumination of particles of smaller size and consequently an enhanced particle rate overall.

When working on high laser power, three facts were observed that were never seen at lower laser power:

a. A "ghost" particle is often observed on the first frame near the tracked particle, revealing the future particle position on the second frame. The PTV code sometimes tracks both the real and the "ghost" particle on the first frame, as showed in Figure 6.1(b), thus calculating no displacement between the "ghost" particle on the first frame and the particle on the second frame, as they have the exact same position.
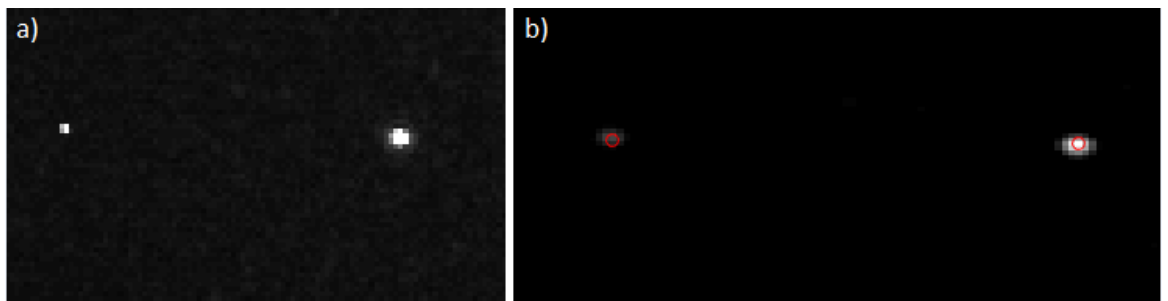
Figure 6.1: "Ghost" particle observed in the first frame as showed in the Insight 3G software (a) and in the PTV custom software (b).

b. Even though the particle should be displayed as bright spots on black background, sometimes the reflections coming from a particle are that high that they create a reflection tail. In such cases, the PTV code has difficulty in finding the center of the

particle, as it finds multiple centers (Figure 6.2(b)). This is encountered by deleting the too bright pixels.
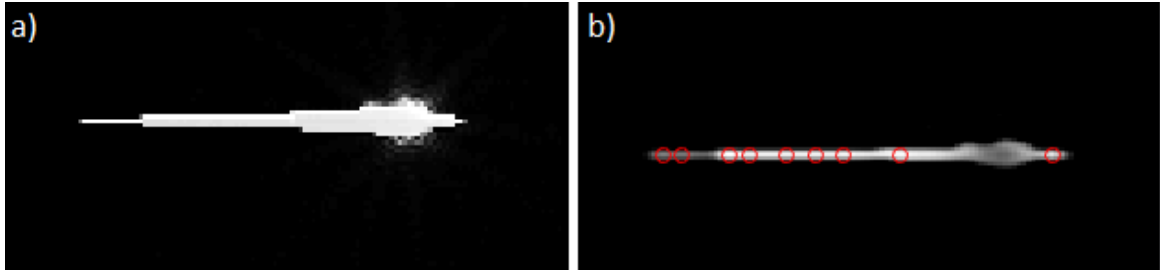
Figure 6.2: Reflection tail created by a particle as showed in the Insight 3G software (a) and in the PTV custom software (b).

c. Particle break down into smaller pieces was sometimes also observed (Figure (6.3)).
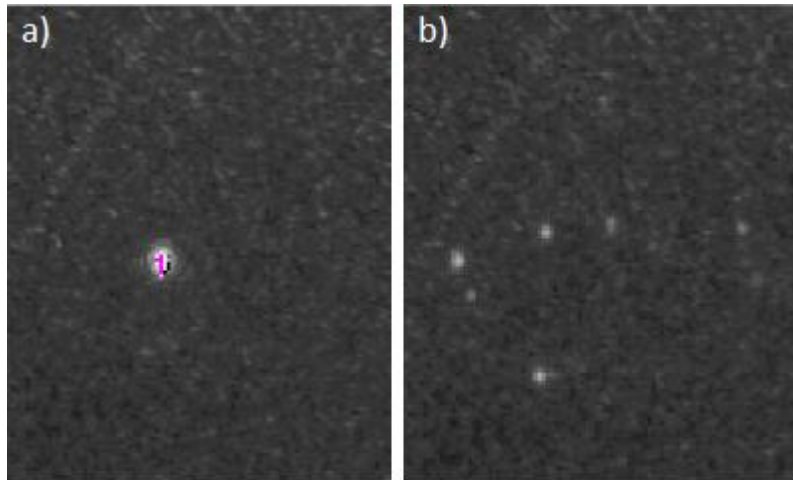
Figure 6.3: Visualization of the particle before (a) and after (b) its break down, due to the high laser power.

None of the three above observations produce large problems during the post processing of the data and in the worst case scenario the code does not track the specific particles. As the particle rate is considerably improved when working on high laser power and also the jet's characteristics are more accurately visualized, it would be concluded that all experiments should be run on high laser power.

However, the only important problem that arises with high laser power is the higher reflections, especially near the capillary, in conjunction to its reflection to the glass used on the rear port for the laser exit. That is also the reason that no particles were managed to be investigated on the supersonic region of the jet, just downstream the capillary exit,

presented previously in Figure 5.22 in subsection 5.2.3. In the following Figure (6.4) the background noise is presented, with and without installing the rear glass on the vacuum chamber, respectively.
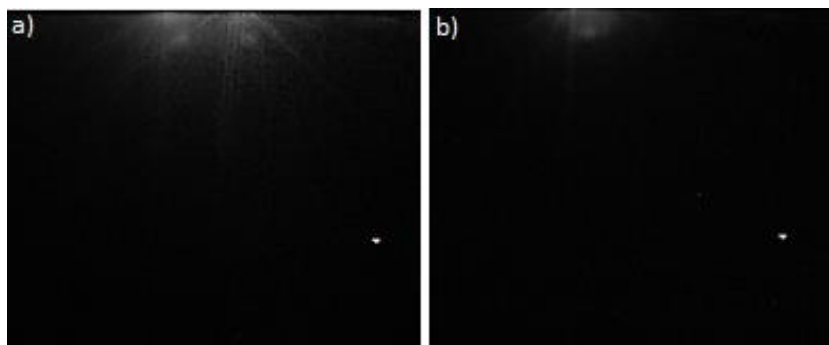
Figure 6.4: Produced noise due to laser reflections when the rear glass is installed (a) and not installed (b) on the vacuum chamber.

In the results presented in subsection 5.2.2, in which the jet expanded inside Aerolens^{TM} at 5 mbar pressure, it is obvious that the Aerolens^{TM} was not fully calibrated to the capillary, as the supporting flange in which Aerolens^{TM} was installed, did not support it totally straight.

Taking all the above into account, the experiments of this work indicate that a redesign of the vacuum chamber is necessary in order to increase the accuracy of the experimental results. Thus, great attention should be paid to three important factors:

a. The minimization of the reflections near the capillary, by trying other materials for the capillary with better absorption or by installing the rear glass at an angle in order to change the direction of the reflections.

b. The easier and more precise calibration of the vacuum chamber to the laser, by using rods, as Fasmatech Science and Technology S.A. already has implemented in its newer designs.

c. The better and more stable support of Aerolens^{TM} glass channel, in order to be totally calibrated to the capillary exit.

Finally, it must be noted that the testing of the ESI source with the fluorescent particles gave very promising results. The particle rate was amazingly enhanced and thus the experimental time is reduced by weeks if not months.

Chapter 7:

Conclusion and Future work

The flow field in the fore vacuum of a Mass Spectrometer was investigated in this work using Particle Image Velocimetry. The flow was investigated both during a Free Jet expansion at 20 mbar, as well as inside Aerolens^{TM} at 5 and 20 mbar respectively. For these experiments polydisperse distributions of Al_2O_3 particles generated by a Spark Discharge Source were employed. The great advantages of the Aerolens^{TM} optics at intermediate pressures were presented, as a fully developed laminarized flow was achieved at the exit of the glass channel. The need of running the experiments on the higher laser power possible was indicated, as it results in a more accurate velocity map and in a reduced amount of time.

Additional experiments were conducted in order to test the applicability of the Electrospray Ionization Source, using fluorescent particles for such PTV applications, which led to very promising results.

Future research would be interesting to include the corresponding experiments of the Free Jet expansion on both high laser power and on the Monodisperse mode, as it has been proved that monodisperse distributions lead to more accurate results [101]. Unfortunately, that will be very difficult inside Aerolens^{TM}, due to the enhanced laser reflections that would probably damage the camera.

In addition, the employment of fluorescent particles using the ESI source should be further investigated, especially with smaller particle size, as it solves the biggest problem encountered when running PIV experiments at high vacuum: the low particle rate.

References

[1]   S. Maher, F.P.M. Jjunju and S. Taylor, "Colloquium: 100 years of mass spectrometry: Perspectives and future trends," *Reviews of Modern Physics,* vol. 87, pp. 113 - 135, 2015.

[2]   J.J. Thomson, Rays of Positive Electricity and their Application to Chemical Analyses, Longmans, Green and Co., London, 1913.

[3]   X. Han, A. Aslanian and J.R. Yates III, "Mass spectrometry for proteomics," *Chemical Biology,* vol. 12, pp. 483 - 490, 2008.

[4]   B.F. Cravatt, G.M. Simon and J.R. Yates III, "The biological impact of mass-spectrometry-based proteomics," *Nature,* vol. 450, pp. 991 - 1000, 2007.

[5]   M.J. Bueno, A. Agüera, . M.J. Gómez, M.D. Hernando, J.F. García-Reyes and A.R. Fernández-Alba, "Application of Liquid Chromatography/Quadrupole-Linear Ion Trap Mass Spectrometry and Time-of-Flight Mass Spectrometry to the Determination of Pharmaceuticals and Related Contaminants in Wastewater," *Analytical Chemistry,* vol. 79, no. 24, pp. 9372 - 9384, 2007.

[6]   P.T. Palmer and T.F. Limero, "Mass Spectrometry in the U.S. Space Program: Past, Present and Future," *American Society for Mass Spectrometry,* vol. 12, p. 656 – 675, 2001.

[7]   D.R. Justes, N. Talaty, I. Cotte-Rodriguez and R.G. Cooks, "Detection of explosives on skin using ambient ionization mass spectrometry," *The Royal Society of Chemistry,* pp. 2142 - 2144, 2007.

[8]   D.R. Ifa, N.E. Manicke, A.L. Dill and R.G. Cooks, "Latent Fingerprint Chemical Imaging by Mass Spectrometry," *Science,* vol. 321, p. 805, 2008.

[9]   D.R. Ifa, L.M. Gumaelius, L.S. Eberlin, N.E. Manicke and R.G. Cooks, "Forensic analysis of inks by imaging desorption electrospray ionization (DESI) mass spectrometry," *The Royal Society of Chemistry,* vol. 132, pp. 461 - 467, 2007.

[10]   A.T. Cawley and U. Flenker, "The application of carbon isotope ratio mass spectrometry to doping control," *Journal of Mass Spectrometry,* vol. 43, pp. 854 - 864, 2008.

[11]   E.C. Horning, M.G. Horning, D.I. Carroll, I. Dzidic and R.N. Stillwell, "New Picogram Detection System Based on a Mass Spectrometer with an External Ionization Source at Atmospheric Pressure," *Analytical Chemistry,* vol. 45, no. 6, pp. 936 - 943, 1973.

[12]   V.V. Laiko, M.A. Baldwin and A.L. Burlingame, "Atmospheric Pressure Matrix-Assisted Laser Desorption/Ionization Mass Spectrometry," *Analytical Chemistry,* vol. 72, no. 4, pp. 652 - 657, 2000.

[13]   D.B. Robb, T.R. Covey and A.P. Bruins, "Atmospheric Pressure Photoionization: An Ionization Method for Liquid Chromatography-Mass Spectrometry," *Analytical Chemistry,* vol. 72, no. 15, pp. 3653 - 3659, 2000.

[14]   W. Paul and H. Steinwedel, "Ein neues Massenspektrometer ohne Magnetfeld," *Z. Naturforschg.,* vol. 8a, pp. 448 - 450, 1953.

[15]   W.E. Stephens, "A Pulsed Mass Spectrometer with Time Dispersion," *Physical Review,* vol. 69, p. 691, 1946.

[16]   W.C. Wiley and I.H. McLaren, "Time-of-Flight Mass Spectrometer with Improved Resolution," *The Review of Scientific Instruments,* vol. 26, no. 12, pp. 1150 - 1157, 1955.

[17]   S. Helmut and W. Paul, "Apparatus for separating charged particles of different specific charges". Patent US 2939952 A, 7 June 1960.

[18]   Q. Hu, R.J. Noll, H. Li, A. Makarov, M. Hardman and R.G. Cooks, "The Orbitrap: A New Mass Spectrometer," *J. Mass Spectrom.,* vol. 40, pp. 430 - 443, 2005.

[19]   D.W. Koppenaal, C.J. Barinaga, M.B. Denton, R.P. Sperline, G.M. Hieftje, G.D. Schilling, F.J. Andrade and J.H. Barnes, "MS Detectors," *Analytical Chemistry,* vol. 77, no. 21, pp. 418 A - 427 A, 2005.

[20]   D. Kounadis, D. Papanastasiou, I. Orfanopoulos, A. Lekkas, A. Zacharos, I. Nikolos and E. Raptakis, "A Novel Ion-Optical Design for Laminarization of Under-expandthed Gas Flows," *ASMS 2013, the 61st ASMS Conference on*

Mass Spectrometry and Allied Topics, Minneapolis, MN, USA, 9 - 13 June, 2013.

[21]   D. Papanastasiou, D. Kounadis, A. Lekkas, A. Zacharos, I. Nikolos, I. Orfanopoulos and E. Raptakis, "The Aerolens: An Evaluation Study based on Computational Methods and Mass Spectrometric Tests," *ASMS 2014, the 62nd ASMS Conference on Mass Spectrometry and Allied Topics*, Baltimore, USA, 15 - 19 June, 2014.

[22]   E. Raptakis, D. Kounadis, A. Lekkas, A. Zacharos, I. Nikolos and D. Papanastasiou, "Tracing Ions and visualizing charged clusters in the aerolens under transitory gas flow conditions", *ASMS 2015, the 63rd ASMS Conference on Mass Spectrometry and Allied Topics*, St. Louis, Missouri, USA, 31 May-4 June, 2015.

[23]   D. Papanastasiou, E. Raptakis, D. Kounadis, A. Lekkas, I. Orfanopoulos and I. K. Nikolos, "Improvements In and Relating to the Control of Ions". US2015340218 (A1), 26 November 2015.

[24]   E. Hoffmann and V. Stroobant, *Mass Spectrometry Principles and Applications*, 3rd ed., John Wiley & Sons Ltd, pp. 42, 2007.

[25]   D. Gerlich, " Inhomogeneous RF Fields: A Versatile Tool for the Study of Processes with Slow Ions," in *Advances in Chemical Physics: State-Selected and State-To-State Ion-Molecule Reaction Dynamics, Part 1. Experiment*, pp. 1 - 176, 1992.

[26]   D. Kounadis, D. Papanastasiou, I. Orfanopoulos, A. Lekkas, I. Nikolos and E. Raptakis, "Visualization of Gas Dynamics inside the Ion Funnel using Particle Tracking Velocimetry", *ASMS 2012, the 60th ASMS Conference on Mass Spectrometry and Allied Topics,* Vancouver, BC, USA, 20 - 24 May, 2012.

[27]   J.B. Fenn, "Electrospray Ionization Mass Spectrometry: How it All Began," *Journal of Biomolecular Techniques,* vol. 13, no. 3, p. 101 – 118, 2002.

[28]   S.A. Shaffer, K. Tang, G.A. Anderson, D.C. Prior, H.R. Udseth and R.D. Smith, "A novel ion funnel for focusing ions at elevated pressure using

electrospray ionization mass spectrometry," *Rapid Communications in Mass Spectrometry,* vol. 11, no. 16, p. 1813 – 1817, 1997.

[29]   [Online]. Available: http://fasmatech.com/.

[30]   E. Mach and P. Salcher, "Photographische Fixirung der durch Projectile in der Luft eingeleiteten Vorgänge," *Sitzungsberichte der Kaiserlichen Akademie der Wissenschaften,* pp. 764 - 781, 1887.

[31]   P. Salcher and J. Whitehead., "Über den Ausfluss stark verdichteter Luft," *Sitzungsberichte der Kaiserlichen Akademie der Wissenschaften,* pp. 267 - 287, 1889.

[32]   E. Mach and P. Saldier, "Optische Untersuchung der Luftstrahlen," *Sitzungsberichte der Kaiserlichen Akademie der Wissenschaften,* pp. 1303 - 1309, 1890.

[33]   L. Prandtl, "Neue Untersuchungen über die strömende Bewegung der Gase und Dämpfe," *Ludwig Prandtl Gesammelte Abhandlungen,* pp. 904 - 934, 1907.

[34]   D.K. Huzel and D.H. Huang, Design of Liquid Propellant Rocket Engines, 2nd ed., pp. 15, 1971.

[35]   J.D. Anderson, [Online]. Available: https://history.nasa.gov/SP-4219/Chapter3.html.

[36]   S. Crist, P.M. Sherman and D.R. Glass, "Study of the Highly Underexpanded Sonic Jet," *AIAA Journal,* vol. 4, no. 1, pp. 68 - 71, 1966.

[37]   J.A. Wilkes, P.M. Danehyt and R.J. Nowakt, "Fluorescence Imaging Study of Transition in Underexpanded Free Jets," ICIASF 2005, the 21st International Congress on Instrumentation in Aerospace Simulation Facilities, Sendai, Japan, 29 August - 1 September, 2005.

[38]   J.A. (Wilkes) Inman, P.M. Danehy, R.J. Nowak and D.W. Alderfer, "Identification of Instability Modes of Transition in Underexpanded Jets," *the 38th Fluid Dynamics Conference and Exhibit, Seattle, Washington, USA, 23 - 26 June,* 2008.

[39]   V.A. Goryaino, "Some possibility of reverse phenomenon for supersonic flows in free jets," *Matem.Mod,* vol. 15, pp. 86 - 92, 2003.

[40]   V.I. Zapryagaev, V.M. Boiko, I.N. Kavun, N.P. Kiselev and A.A. Pivovarov, "Flow Structure Behind the Mach Disk in Supersonic Non-Isobaric Jet," *AIP Conference Proceedings,* vol. 1770, no. 1, pp. 1 - 8, 2016.

[41]   P.A. Skovorodko, "About the Nature of the Recirculation Zone Behind a Mach Disk in an Underexpanded Jet," 2011.

[42]   A. Krothapalli, G. Buzyna and L. Lourenco, "Streamwise vortices in an underexpanded axisymmetric jet," *Physics of Fluids A,* vol. 3, no. 8, pp. 1848 - 1851, 1991.

[43]   M. Jugroot and C.P.T. Groth, "Numerical Investigation of Ion Transport in Under-Expanded Jet Flows," *AIAA 2003, the 36th AIAA Thermophysics Conference*, Orlando, Florida, USA, 23 - 26 June, 2003.

[44]   C. Chauveau, D.M. Davidenko, B. Sarh, I. Gökalp, V. Avrashkov and C. Fabre, "PIV Measurements in an Underexpanded Hot Free Jet," the *13th Int Symp on Applications of Laser Techniques to Fluid Mechanics*, Lisbon, Portugal, 26 - 29 June, 2006.

[45]   E.S. Love and C.E. Grigsby, "Some Studies of Axisymmetric Free Jets Exhausting from Sonic and Supersonic Nozzles into Still Air and into Supersonic Streams," NACA-RM-L54L31, 1955.

[46]   E.S. Love, M.J. Woodling and L.P. Lee, "Boundaries of Supersonic Axisymmetric Free Jets," NACA-RM-L56G18, 1956.

[47]   E.S. Love and L.P. Lee, "Shape of Initial Portion of Boundary of Supersonic Axisymmetric Free Jets at Large Jet Pressure Ratios," NACA-TN-4195, 1958.

[48]   E.S. Love, C.E. Grigsby, L.P. Lee and M.J. Woodling, "Experimental and Theoretical Studies of Axisymmetric Free Jets," NASA-TR-R-6, 1959.

[49]   T.C. Adamson and J.A. Nicholls, "On the Structure of Jets from Highly Underexpanded Nozzles into Still Air," *Journal of the Aerospace Sciences,* Vol. 26, No. 1, pp. 16-24, 1958.

[50]   D.W. Eastman and L.P. Radtke, "Location of the Normal Shock Wave in the Exhaust Plume of a Jet," *AIAA Journal,* vol. 1, no. 4, pp. 918 - 919, 1963.

[51]   J. Bowyer, L. D' Attorre and H. Yoshihara, "The Flow Field Resulting from Mach Reflection of a Convergent Conical Shock at the Axis of a Supersonic, Axially Symmetric Jet," General Dynamics/ Astronautics, Report GDA 63-0586, 1963.

[52]   A.L. Addy, "Effects of axisymmetric sonic nozzle geometry on Mach disk characteristics," *AIAA Journal,* vol. 19, no. 1, pp. 121 - 122, 1981.

[53]   E. Franquet, V. Perrier, S. Gibout and P. Bruel, "Free underexpanded jets in a quiescent medium: A review," *Progress in Aerospace Sciences,* vol. 77, pp. 25 - 53, 2015.

[54]   A.D. Birch, D.R. Brown, M.G. Dodson and F. Swaffield, "The Structure and Concentration Decay of High Pressure Jets of Natural Gas," *Combustion Science and Technology,* vol. 36, no. 5-6, pp. 249 - 261, 1984.

[55]   A.D. Birch, D.J. Hughes and F. Swaffield, "Velocity Decay of High Pressure Jets," *Combustion Science and Technology,* vol. 52, no. 1-3, pp. 161 - 171, 1987.

[56]   B.C.R. Ewan and K. Moodie, "Structure and Velocity Measurements in Underexpanded Jets," *Combustion Science and Technology,* vol. 45, no. 5-6, pp. 275 - 288, 1986.

[57]   K.B. Yüceil and M.V. Ötügen, "Scaling parameters for underexpanded supersonic jets," *Physics of Fluids,* vol. 14, no. 12, pp. 4206 - 4215, 2002.

[58]   J.A. Wilkes, C.E. Glass, P.M. Danehy and R.J. Nowak, "Fluorescence Imaging of Underexpanded Jets and Comparison with CFD," *AIAA 2006, the 44th AIAA Aerospace Sciences Meeting and* Exhibit, Reno, Nevada, 9 - 12 January, 2006.

[59]   J.A. Inman, P.M. Danehy, R.J. Nowak and D.W. Alderfer, "The Effect of Impingement on Transitional Behavior in Underexpanded Jets," *AIAA 2009, the 47th AIAA Aerospace Sciences Meeting including The New Horizons Forum and Aerospace Exposition*, Orlando, 5 - 8 January, 2009.

[60]   F.M. White, Viscous Fluid Flow, 2nd ed., pp. 29, New York, 1991.

[61]   M. Dole, L.L. Mack, R.L. Hines, C. Mobley, L.D. Ferguson and M.B. Alice, "Molecular Beams of Macroions," *The Journal of Chemical Physics,* vol. 49, no. 5, pp. 2240 - 2249, 1968.

[62]   M. Yamashita and J.B. Fenn, "Electrospray Ion Source. Another Variation on the Free-Jet Theme," *The Journal of Physical Chemistry,* vol. 88, no.20, pp. 4451 - 4459, 1984.

[63]   J.B. Fenn, "Electrospray Wings for Molecular Elephants," in *Nobel Lecture*, 2002.

[64]   C. Ho, C. Lam, M. Chan, R. Cheung, L. Law, L. Lit, K.Ng, M. Suen and H. Tai, "Electrospray Ionisation Mass Spectrometry: Principles and Clinical," *Clinical Biochemist Reviews,* vol. 24, No. 1, pp. 3 - 12, 2003.

[65]   H. Altgeldt, A. Schnettler and D. Stehmeier , "Spark discharge particle generator for laser Doppler anemometry," *Journal of Physics E: Scientific Instruments,* vol. 13, no. 4, pp. 437 - 441, 1979.

[66]   S. Schwyn, E. Garwin and A. Schmidt-Ott, "Aerosol Generation By Spark Discharge," *J. Aerosol Sci.,* vol. 19, no.5, pp. 1 - 4, 1988.

[67]   [Online].   Available: http://www.tsi.com/uploadedFiles/_Site_Root/Products/Literature/Applicatio n_Notes/Review_on_CPC_and_SMPS_CPC-003-US-web.pdf?id=32305.

[68]   L. Prandtl, "Motion of Fluids with very little Viscosity," 1928.

[69]   M. Raffel, C. Willert, S. Wereley and J. Kompenhans, Particle Image Velocimetry. A practical guide, 2nd ed., Springer, pp. 7, 2007.

[70]   C.F. Bohren and D.R. Huffman, Absorption and Scattering of Light by Small Particles, pp. 3-11, 2007.

[71]   D.W. Hahn, *Light Scattering Theory*, Department of Mechanical and Aerospace Engineering, University of Florida, 2009.

[72]   H.J. Strutt, "On the light from the sky, its polarization and colour," *Philosophical Magazine Series 4,* vol. xxxvi, pp. 107 - 120, 1871.

[73]   H.J. Strutt, "On the scattering of light by small particles," *Philosophical Magazine Series 4,* pp. 447 - 454, 1871.

[74]   Lord Rayleigh F.R.S, "On the electromagnetic theory of light," *Philosophical Magazine Series 5,* vol. 12, no. 73, pp. 81 - 101, 1881.

[75]   Lord Rayleigh F.R.S., "On the transmission of light through an atmosphere containing small particles in suspension, and on the origin of the blue of the sky," *Philosophical Magazine Series 5,* pp. 375-384, 1899.

[76]   G. Mie, "Beiträge zur Optik trüber Medien, speziell kolloidaler Metallösungen," *Annalen der Physik,* vol. 4, no. 25, pp. 377 - 445, 1908.

[77]   C.F. Bohren and D.R. Huffman, Absorption and Scattering of Light by Small Particles, pp. 82 - 129, 2007.

[78]   R. Nave. [Online]. Available: http://hyperphysics.phy-astr.gsu.edu/hbase/atmos/blusky.html.

[79]   J.H. Seinfeld and S.N. Pandis, Atmospheric Chemistry and Physics: From Air Pollution to Climate Change, John Wiley and Sons, pp. 633 - 639, 2006.

[80]   A. Melling, "Tracer particles and seeding for particle image velocimetry," *Meas. Sci. Technol.,* vol. 8, p. 1406 – 1416, 1997.

[81]   G. Tedeschi and H.R. Gouin, "Particle motion through an oblique shock wave," *Proc. SPIE, the 5th International Conference on Laser Anemometry: Advances and Applications,* vol. 2052, pp. 273 - 278, Veldhoven, Netherlands, 1993.

[82]   G. Tedeschi, H. Gouin and M. Elena, "Motion of tracer particles in supersonic flows," *Experiments in Fluids,* vol. 26, pp. 288 - 296, 1999.

[83]   N. Lang, "Investigation of the Supersonic Flow Field around a delta wing using Particle-Image-Velocimetry," *the 10th International Symposium on Applications of Laser Techniques to Fluid Mechanics*, Lisbon, 10 - 13 July, 2000.

[84]   W.D. Urban and M.G. Mungal, "Planar velocity measurements in compressible mixing layers," *J. Fluid Mech.,* vol. 431, pp. 189 - 222, 2001.

[85]   F. Scarano and B. van Oudheusden, "Planar velocity measurements of a two-dimensional compressible wake," *Experiments in Fluids,* vol. 34, p. 430 – 441, 2003.

[86]   D. Ragni, F. Schrijer, B.W. van Oudheusden and F. Scarano, "Particle tracer response across shocks measured by PIV," *Exp Fluids,* vol. 50, pp. 53 - 64, 2011.

[87]   D. Mitchell, D. Honnery and J. Soria, "Particle relaxation and its influence on the particle image velocimetry cross-correlation function," *Experiments in Fluids,* vol. 51, p. 933 – 947, 2011.

[88]   O.J.H. Williams, T. Nguyen, A.M. Schreyer and A.J. Smits, "Particle response analysis for particle image velocimetry in supersonic flows," *Physics of Fluids,* vol. 27, no. 7, pp. 1 - 15, 2015.

[89]   S. Ghaemi, A. Schmidt-Ott and F. Scarano, "Nanostructured tracers for laser-based diagnostics in high-speed flows," *Measurement Science and Technology,* vol. 21, 2010.

[90]   [online].   Available: http://flowell.hu/wp-content/uploads/downloads/2013/06/Insight3G.pdf

[91]   K.N. Margaris, Z.Nepiyushchikh , D.C. Zawieja , J.J. Moore and R.A. Black, "Microparticle image velocimetry approach to flow measurements in isolated contracting lymphatic vessels," *Journal of Biomedical Optics,* vol. 21, no. 2, 2015.

[92]   R.J. Adrian and J. Westerweel, Particle Image Velocimetry, Cambridge University Press, p. 129, 2011.

[93]   [Online].   Available: http://www.tsi.com/uploadedFiles/_Site_Root/Products/Literature/Applicatio n_Notes/LLS-001-Model_610026_Laser_Light_Sheet_Optics-A4-web.pdf.

[94]   [Online].   Available: https://www.pnnl.gov/main/publications/external/technical_reports/PNNL-14819.pdf

[95]   J.C. Crocker and D.G. Grier, "Methods of Digital Video Microscopy for Colloidal Studies," *Journal of Colloid and Interface Science,* vol. 179, no. 1, pp. 298-310, 1996.

[96]   J.C. Crocker and E.R. Weeks. [Online]. Available: http://www.physics.emory.edu/faculty/weeks//idl/.

[97] D.Blair and E.Dufresne. [Online]. Available: http://site.physics.georgetown.edu/matlab/code.html.

[98] [Online]. Available: http://people.umass.edu/kilfoil/tools.php.

[99] M. Nixon and A. Aguado, Feature Extraction & Image Processing, 2nd ed., Elsevier, 2008, p. 88.

[100] G. Levin. [Online]. Available: http://openframeworks.cc/ofBook/chapters/image_processing_computer_visi on.html#preliminariestoimageprocessing.

[101] D. Papanastasiou, D. Kounadis, I. Orfanopoulos, I. K. Nikolos and E. Raptakis, "Visualization of Under-Expanded Jets in the Atmospheric Pressure - Vacuum Interface of a Mass Spectrometer," *ASMS 2012, the 60th ASMS Conference on Mass Spectrometry and Allied Topics,* Vancouver, BC, USA, 20 - 24 May, 2012.

Appendix A

Codes

What follows is the Matlab code, developed for the following functions:

• <u>Particle Tracking</u>

"PTV_Background_noisemapping.m" – Calls the bpass and pkfnd functions and generates an image containing the noise coordinates for each frame. This image will be used as the background image in PTV_remove_noisemapping.m.

"PTV_remove_noisemapping.m" – Calls the bpass, cntrd, pkfnd and track functions and generates a ".txt" file containing the coordinates and velocity of particles. The ".txt" file will be then used to create the vectormap.

The "bpass.m", "pkfnd.m", "cntrd.m" and "track.m" created by John C. Crocker and Eric R. Weeks have been used (http://site.physics.georgetown.edu/matlab/).

• <u>Creation of Vectormap</u>
"loadpoints_0mm.m"
"display_coloured_vectors.m"

PTV_Background_noisemapping.m

```matlab
clear all
close all

lnoise1=0.9;   %bpass
lnoise2=0.9;
lobject1=5;   %bpass
lobject2=5;
th1=7.0;   %pkfnd
th2=7.0;
sz1=5;   %cntrd
sz2=5;
maxdisp=100;   %track
dt=1;  %microseconds
%pixmm=7.11;

x0=80;
y0=50;   %pixels
x=1900;
y=1900;

theta=-90.5;
rect=[x0 y0 x y];




%%%%%%%%%%%%%%%%%%fopen a single file%%%%%%%%%%%%%%%%%%%%%
%%%%%%%%%%%%%%%%%%%%%%%START%%%%%%%%%%%%%%%%%%%%%%%%%%%
folder = uigetdir;
Files = dir(folder);
files = {Files.name};isdir = [Files.isdir];
files(isdir) = [];
s = listdlg('ListString', files);
selectedFiles = files(s);

if iscell(selectedFiles) == 0 %if select only one file, then the data will not be a cell

  image = imread(selectedFiles);
  if image==-1          % If this returns a -1, we did not open the file successfully.
    error('File not found or permission denied');
  end

end
%%%%%%%%%%%%%%%%%%fopen a single file%%%%%%%%%%%%%%%%%%%%%
%%%%%%%%%%%%%%%%%%%%%%%END%%%%%%%%%%%%%%%%%%%%%%%%%%%
```

```matlab
 k=0;     %loop counter. When k=n, don't clear imageA imageB imgA imgB fobjectA fobjectB
(line 227)
n=length(selectedFiles);


for i=1:2:n

  if i==1
    image_number=1
  else
    image_number=i-image_number           %for more than 1 frames: image_number=i-
image_number
  end

  flag=1;

  imageA(:,:) = imread(selectedFiles{i});
  imageB(:,:) = imread(selectedFiles{i+1});

  imageA=imrotate(imageA,theta);
  imageB=imrotate(imageB,theta);




%%%%%%%%%%%%%%%%remove damaged pixels %%%%%%%%%%%%%%%%%
%%%%%%%%%%%%%%%%%%%%%%%%%START%%%%%%%%%%%%%%%%%%%%%%%%%%

%some pixels on the camera were damaged and thus needed to be removed
  %%%%low damaged pixel line%%%%
  for ipB=1:209

    for jpB=1:2043

      imageA(1707+ipB,40+jpB)=0;  % (y,x)
      imageB(1707+ipB,40+jpB)=0;

    end

  end

  %%%%vertical damaged pixel line%%%%
  for ipC=1:310

    for jpC=1:15

      imsubA(1160+ipC,1222+jpC)=0;  % (y,x)
      imsubB(1160+ipC,1222+jpC)=0;

    end

  end
```

```matlab
%%%%small damaged spot%%%%
for ipC=1:19

    for jpC=1:12

        imageA(1342+ipC,1562+jpC)=0;  % (y,x)
        imageB(1342+ipC,1562+jpC)=0;

    end

end

%%%%big damaged spot on pixel line%%%%
for ipC=1:181

    for jpC=1:231

        imageA(1675+ipC,1519+jpC)=0;  % (y,x)
        imageB(1675+ipC,1519+jpC)=0;

    end

end


%%%aerolens upper wall boundary%%%%
for ipE=1:220

    for jpE=1:867

        imageA(480+ipE,111+jpE)=0;
        imageB(480+ipE,111+jpE)=0;


    end

end


%%%%aerolens lower wall boundary%%%%
for ipF=1:210

    for jpF=1:861

        imageA(1200+ipF,111+jpF)=0;
        imageB(1200+ipF,111+jpF)=0;

    end

end

%%%%%%%%%%%%%%%%%remove damaged pixels %%%%%%%%%%%%%%%%%
```

```matlab
  cimageA(:,:) = imcrop(imageA(:,:),rect);    %crops the image rectangular
  cimageB(:,:) = imcrop(imageB(:,:),rect);


  imgA(:,:)=bpass(cimageA(:,:),lnoise1,lobject1);      % Implements a real-space bandpass
filter. See bpass.m for more info.
  imgB(:,:)=bpass(cimageB(:,:),lnoise2,lobject2);


  fobjectA(:,:)=pkfnd(imgA(:,:),th1,sz1);      % finds local maxima in an image to pixel level
accuracy. See pkfnd.m for more info.
  fobjectB(:,:)=pkfnd(imgB(:,:),th2,sz2);


  sfobjectA=size(fobjectA(:,:));    %e.g. sfobjectA = 127  2
  sfobjectA=sfobjectA(1);    %Number of local maxima found with pkfnd e.g. sfobjectA = 127

  sfobjectB=size(fobjectB(:,:));
  sfobjectB=sfobjectB(1);


  if i==1
    size_imgA=size(imgA,1);

    for i=1:size_imgA
      for j=1:size_imgA
        peaks_A(i,j)=0;   %Create a black image same size as imgA
        peaks_B(i,j)=0;
      end
    end
  end


  for i=1:sfobjectA

    d=fobjectA(i,1);    %fobjectA is a matrix with 2 columns and sfobjectA rows. It contains
the coordinates of local maxima.
    e=fobjectA(i,2);
    peaks_A(e,d) = peaks_A(e,d)+1;    %Thus, we say here e.g. go to peaks_A(1175,1146) and
increase intensity by 1.

  end


  for i=1:sfobjectB

    d=fobjectB(i,1);
    e=fobjectB(i,2);
    peaks_B(e,d) = peaks_B(e,d)+1;
```

```matlab
        end


    k=k+1;

    if k~=n
        clear imageA imageB imgA imgB fobjectA fobjectB
    end


end


oneA=zeros(size_imgA); %oneA=peaks_A;    %pixels encounteres only once, hopefully only
particles
oneB=zeros(size_imgA);
noiseA=zeros(size_imgA);   %the noise that will consist the background image in main code.
noiseB=zeros(size_imgA);


for i=1:size_imgA
    for j=1:size_imgA
        if peaks_A(i,j)== 1
            oneA(i,j)=500;   %From the peaks_A keep only the local maxima found once (particles)
        end
        if peaks_B(i,j)== 1
            oneB(i,j)=500;
        end
        if peaks_A(i,j)> 1
            noiseA(i,j)=1000;   %From the peaks_A keep only the local maxima founde more than
once (noise)
        end
        if peaks_B(i,j)> 1
            noiseB(i,j)=1000;
        end
    end
end


figure,%('Color',[1 1 1]),
imagesc(oneA);    % Scale data and display as image. imagesc(...) is the same as IMAGE(...)
except the data is scaled to use the full colormap.
colormap(gray);   %Color look-up table.
xlabel({'pixels'});   % adds text "pixels" beside the X-axis on the current axis.
ylabel({'pixels'});   % adds text "pixels" beside the Y-axis on the current axis.
set(gca,'DataAspectRatio',[1 1 1]);      %gca: Get handle to current axis. The first element
specifying the intensity of red light, the second green, and the third blue.  Color intensity can
be specified on the interval 0.0 to 1.0. For example, [0 0 0] is black, [1 1 1] is white
impixelinfo;
```

```matlab
figure,%('Color',[1 1 1]),
imagesc(noiseA);    % Scale data and display as image. imagesc(...) is the same as IMAGE(...)
except the data is scaled to use the full colormap.
colormap(gray);    %Color look-up table.
xlabel({'pixels'});    % adds text "pixels" beside the X-axis on the current axis.
ylabel({'pixels'});    % adds text "pixels" beside the Y-axis on the current axis.
set(gca,'DataAspectRatio',[1 1 1]);      %gca: Get handle to current axis. The first element
specifying the intensity of red light, the second green, and the third blue.  Color intensity can
be specified on the interval 0.0 to 1.0. For example, [0 0 0] is black, [1 1 1] is white
impixelinfo;

figure,%('Color',[1 1 1]),
imagesc(noiseB);    % Scale data and display as image. imagesc(...) is the same as IMAGE(...)
except the data is scaled to use the full colormap.
colormap(gray);    %Color look-up table.
xlabel({'pixels'});    % adds text "pixels" beside the X-axis on the current axis.
ylabel({'pixels'});    % adds text "pixels" beside the Y-axis on the current axis.
set(gca,'DataAspectRatio',[1 1 1]);      %gca: Get handle to current axis. The first element
specifying the intensity of red light, the second green, and the third blue.  Color intensity can
be specified on the interval 0.0 to 1.0. For example, [0 0 0] is black, [1 1 1] is white
impixelinfo;

imwrite(noiseA,'00_20171201_backgroundimageA.tiff');    %Create the background image
imwrite(noiseB,'00_20171201_backgroundimageB.tiff');
% imwrite(oneA,'particles.tiff');
imwrite(oneB,'particles.tiff');
```

PTV_Remove_noisemapping.m


```
clear all
close all

backgroundimage_A = imread('00_20171201_backgroundimageA.TIFF');  %Name of image
created by PTV_Background_Noisemapping.m
backgroundimage_B = imread('00_20171201_backgroundimageB.TIFF');

%%%%%%%%%%%%%%%fopen a single file%%%%%%%%%%%%%%%%%%%%%
%%%%%%%%%%%%%%%%%%%%%%%START%%%%%%%%%%%%%%%%%%%%%%%%%
folder = uigetdir;
Files = dir(folder);
files = {Files.name};isdir = [Files.isdir];
files(isdir) = [];
s = listdlg('ListString', files);
selectedFiles = files(s);

if iscell(selectedFiles) == 0 %if select only one file, then the data will not be a cell

   image = imread(selectedFiles);
   if image==-1          % If this returns a -1, we did not open the file successfully.
     error('File not found or permission denied');
   end

end
%%%%%%%%%%%%%%%fopen a single file%%%%%%%%%%%%%%%%%%%%%
%%%%%%%%%%%%%%%%%%%%%%%END%%%%%%%%%%%%%%%%%%%%%%%%%%


lnoise1=0.9;   %bpass
lnoise2=0.9;
lobject1=5;   %bpass
lobject2=5;
th1=10.0;  %pkfnd
th2=10.0;
sz1=5;   %cntrd
sz2=5;
maxdisp=100;   %track
dt=1; %microseconds
% pixmm=7.11;

x0=80;
y0=50;   %pixels
x=1900;
y=1900;

theta=-90.5;
rect=[x0 y0 x y];
size_img=size(backgroundimage_A,1);
```

```matlab
k=0;     %loop counter. When k=n, don't clear imageA imageB imgA imgB fobjectA fobjectB
(line 227)
flag=1;
n=length(selectedFiles);


for i=1:2:n

%    if i==1
%      image_number=1
%    else
%        image_number=i-image_number    %for more than 1 frames: image_number=i-
image_number
%    end

  flag=1;

  imageA(:,:) = imread(selectedFiles{i});
  imageB(:,:) = imread(selectedFiles{i+1});

  imageA=imrotate(imageA,theta);
  imageB=imrotate(imageB,theta);


%%%%%%%%%%%%%%%%%%%%remove    damaged    pixels%%%%%%%%%%%%%%%%
%%%%%%%%%%%%%%%%%%%%%%%%%%START%%%%%%%%%%%%%%%%%%%%%%%%%%

  %%%%low damaged pixel line%%%%
  for ipB=1:209

    for jpB=1:2043

      imageA(1707+ipB,40+jpB)=0; % (y,x)
      imageB(1707+ipB,40+jpB)=0;

    end

  end

  %%%%vertical damaged pixel line%%%%
  for ipC=1:310

    for jpC=1:15

      imsubA(1160+ipC,1222+jpC)=0; % (y,x)
      imsubB(1160+ipC,1222+jpC)=0;

    end
```

```matlab
end

 %%%%small damaged spot%%%%
for ipC=1:19

  for jpC=1:12

    imageA(1342+ipC,1562+jpC)=0;  % (y,x)
    imageB(1342+ipC,1562+jpC)=0;

  end

end

  %%%%big damaged spot on pixel line%%%%
for ipC=1:181

  for jpC=1:231

    imageA(1675+ipC,1519+jpC)=0;  % (y,x)
    imageB(1675+ipC,1519+jpC)=0;

  end

end


%%%aerolens upper wall boundary%%%%
for ipE=1:220

  for jpE=1:867

    imageA(480+ipE,111+jpE)=0;
    imageB(480+ipE,111+jpE)=0;


  end

end


%%%%aerolens lower wall boundary%%%%
for ipF=1:210

  for jpF=1:861

    imageA(1200+ipF,111+jpF)=0;
    imageB(1200+ipF,111+jpF)=0;

  end

end
```

```matlab
%%%%%%%%%%%%%%%%%%%%remove   damaged   pixels%%%%%%%%%%%%%%%
%%%%%%%%%%%%%%%%%%%%%%%%%END%%%%%%%%%%%%%%%%%%%%%%%%


  cimageA(:,:) = imcrop(imageA(:,:),rect);    %crops the image rectangular
  cimageB(:,:) = imcrop(imageB(:,:),rect);


  imgA(:,:)=bpass(cimageA(:,:),lnoise1,lobject1);       % Implements a real-space bandpass
filter. See bpass.m for more info.
  imgB(:,:)=bpass(cimageB(:,:),lnoise2,lobject2);


  for ii=1:size_img
    for jj=1:size_img
      if backgroundimage_A(ii,jj) > 1
        imgA(ii,jj)=0;   %remove the noise(background image) from imgA

        imgA(ii,jj-1)=0;    %remove also +/-1 pixels
        imgA(ii,jj+1)=0;
        imgA(ii-1,jj)=0;
        imgA(ii-1,jj-1)=0;
        imgA(ii-1,jj+1)=0;
        imgA(ii+1,jj)=0;
        imgA(ii+1,jj-1)=0;
        imgA(ii+1,jj+1)=0;

%           imgA(ii,jj-2)=0;   %remove also +/-2 pixels
%           imgA(ii,jj+2)=0;
%           imgA(ii-1,jj-2)=0;
%           imgA(ii-1,jj+2)=0;
%           imgA(ii+1,jj-2)=0;
%           imgA(ii+1,jj+2)=0;
%           imgA(ii-2,jj)=0;
%           imgA(ii-2,jj-1)=0;
% %            imgA(ii-2,jj-2)=0;
%           imgA(ii-2,jj+1)=0;
% %            imgA(ii-2,jj+2)=0;
%           imgA(ii+2,jj)=0;
%           imgA(ii+2,jj-1)=0;
% %            imgA(ii+2,jj-2)=0;
%           imgA(ii+2,jj+1)=0;
% %            imgA(ii+2,jj+2)=0;
      end

      if imgA(ii,jj)>1000    %if something is very bright, remove it
        imgA(ii,jj)=0;
        imgA(ii,jj-1)=0;
        imgA(ii,jj+1)=0;
```

```
        imgA(ii-1,jj)=0;
        imgA(ii-1,jj-1)=0;
        imgA(ii-1,jj+1)=0;
        imgA(ii+1,jj)=0;
        imgA(ii+1,jj-1)=0;
        imgA(ii+1,jj+1)=0;
    end



    if backgroundimage_B(ii,jj) > 1
        imgB(ii,jj)=0;    %remove the noise(background image) from imgB

        imgB(ii,jj-1)=0;    %remove also +/-1 pixels
        imgB(ii,jj+1)=0;
        imgB(ii-1,jj)=0;
        imgB(ii-1,jj-1)=0;
        imgB(ii-1,jj+1)=0;
        imgB(ii+1,jj)=0;
        imgB(ii+1,jj-1)=0;
        imgB(ii+1,jj+1)=0;

%          imgB(ii,jj-2)=0;
%          imgB(ii,jj+2)=0;
%          imgB(ii-1,jj-2)=0;
%          imgB(ii-1,jj+2)=0;
%          imgB(ii+1,jj-2)=0;
%          imgB(ii+1,jj+2)=0;
%          imgB(ii-2,jj)=0;
%          imgB(ii-2,jj-1)=0;
% %            imgB(ii-2,jj-2)=0;
%          imgB(ii-2,jj+1)=0;
% %            imgB(ii-2,jj+2)=0;
%          imgB(ii+2,jj)=0;
%          imgB(ii+2,jj-1)=0;
% %            imgB(ii+2,jj-2)=0;
%          imgB(ii+2,jj+1)=0;
% %            imgB(ii+2,jj+2)=0;
    end
    if imgB(ii,jj)>1000    %if something is very bright, remove it
        imgB(ii,jj)=0;
        imgB(ii,jj-1)=0;
        imgB(ii,jj+1)=0;
        imgB(ii-1,jj)=0;
        imgB(ii-1,jj-1)=0;
        imgB(ii-1,jj+1)=0;
        imgB(ii+1,jj)=0;
        imgB(ii+1,jj-1)=0;
        imgB(ii+1,jj+1)=0;
    end
  end
end
```

```matlab
    fobject=pkfnd(imgA(:,:),th1,sz1);
    sfobject=size(fobject(:,:));
    sfobject=sfobject(1);


    for sp=1:sfobject    %in order to be a particle, it has to have at least one layer of nonzero
pixels around its local maxima
        if imgA(fobject(sp,2)-1,fobject(sp,1)) > 0 ...
          & imgA(fobject(sp,2)+1,fobject(sp,1)) > 0 ...
          & imgA(fobject(sp,2),fobject(sp,1)-1) > 0 ...
          & imgA(fobject(sp,2)-1,fobject(sp,1)-1) > 0 ...
          & imgA(fobject(sp,2)+1,fobject(sp,1)-1) > 0 ...
          & imgA(fobject(sp,2),fobject(sp,1)+1) > 0 ...
          & imgA(fobject(sp,2)-1,fobject(sp,1)+1) > 0 ...
          & imgA(fobject(sp,2)+1,fobject(sp,1)+1) > 0 ...    %till here is a radius of 1 non-zero
particles
          & imgA(fobject(sp,2),fobject(sp,1)-2) > 0 ...
          & imgA(fobject(sp,2)-1,fobject(sp,1)-2) > 0 ...
          & imgA(fobject(sp,2)+1,fobject(sp,1)-2) > 0 ...
          & imgA(fobject(sp,2),fobject(sp,1)+2) > 0 ...
          & imgA(fobject(sp,2)-1,fobject(sp,1)+2) > 0 ...
          & imgA(fobject(sp,2)+1,fobject(sp,1)+2) > 0;       %till here is a radius of 2 non-zero
particles


        fobject(sp,:)=fobject(sp,:);


        else
          fobject(sp,:)=0;

        end
    end

    if isempty(fobject)== 0
      nonzero=find(fobject(:,1)~=0);
      fobjectA=fobject(nonzero,:);
    else
      fobjectA=0;
    end




    if fobjectA~=0;
      dlmwrite('lmID_20171201_aerolens_20mbar_1pos.txt',selectedFiles{i},'-
append','delimiter','\t');    %write image name with particles in frameA, even if untrackable
with B
      sfobjectA=size(fobjectA(:,:));
      sfobjectA=sfobjectA(1);
```

```matlab
        fcentroid(:,:)=cntrd(imgA(:,:),fobjectA(:,:),sz1);    %calculates the centroid of bright spots
to sub-pixel accuracy.
        xyzsA(:,:)=horzcat(fcentroid(:,1:2),1*ones([sfobjectA 1]));

    else
        flag=0;

    end

    clear fobject sfobject



    fobject=pkfnd(imgB(:,:),th1,sz1);
    sfobject=size(fobject(:,:));
    sfobject=sfobject(1);

    for sp=1:sfobject    %in order to be a particle, it has to have at least layer of nonzero pixels
around it
        if imgB(fobject(sp,2)-1,fobject(sp,1)) > 0 ...
            & imgB(fobject(sp,2)+1,fobject(sp,1)) > 0 ...
            & imgB(fobject(sp,2),fobject(sp,1)-1) > 0 ...
            & imgB(fobject(sp,2)-1,fobject(sp,1)-1) > 0 ...
            & imgB(fobject(sp,2)+1,fobject(sp,1)-1) > 0 ...
            & imgB(fobject(sp,2),fobject(sp,1)+1) > 0 ...
            & imgB(fobject(sp,2)-1,fobject(sp,1)+1) > 0 ...
            & imgB(fobject(sp,2)+1,fobject(sp,1)+1) > 0 ...    %till here is a radius of 1 non-zero
particles
            & imgB(fobject(sp,2),fobject(sp,1)-2) > 0 ...
            & imgB(fobject(sp,2)-1,fobject(sp,1)-2) > 0 ...
            & imgB(fobject(sp,2)+1,fobject(sp,1)-2) > 0 ...
            & imgB(fobject(sp,2),fobject(sp,1)+2) > 0 ...
            & imgB(fobject(sp,2)-1,fobject(sp,1)+2) > 0 ...
            & imgB(fobject(sp,2)+1,fobject(sp,1)+2) > 0;    %till here is a radius of 2 non-zero
particles


        fobject(sp,:)=fobject(sp,:);


    else
        fobject(sp,:)=0;

    end
    end

    if isempty(fobject)== 0
        nonzero=find(fobject(:,1)~=0);
        fobjectB=fobject(nonzero,:);
    else
        fobjectB=0;
    end
```

```matlab
    if fobjectB(:,:)~=0;

      sfobjectB=size(fobjectB(:,:));
      sfobjectB=sfobjectB(1);

      fcentroid2(:,:)=cntrd(imgB(:,:),fobjectB(:,:),sz2);      %calculates the centroid of bright
spots to sub-pixel accuracy.
      xyzsB(:,:)=horzcat(fcentroid2(:,1:2),2*ones([sfobjectB 1]));

    else
      flag=0;
          %delete(selectedFiles{i},selectedFiles{i+1});
    end

    clear fobject sfobject fobjectA sobjectA fobjectB sobjectB  fcentroid fcentroid2



if flag~=0;    %if the pkfnd has found coordinates of local maxima


      xyzs2(:,:)=vertcat(xyzsA(:,:),xyzsB(:,:));     % Vertical concatenation of matrices xyzsA
and xyzsB.

      trp(:,:)=track(xyzs2(:,:),maxdisp);      %Constructs n-dimensional trajectories from a
scrambled list of particle coordinates determined at discrete times

      clear xyzsA xyzsB xyzs2



      sztrp=size(trp(:,:));
      sztrp=sztrp(1);

      if sztrp>max(trp(:,4));

        for m=2:sztrp

          if trp(m,4)==trp(m-1,4);

            xp(:,m)=(trp(m,1)+trp(m-1,1))/2;
            yp(:,m)=(trp(m,2)+trp(m-1,2))/2;
            vx(:,m)=(trp(m,1)-trp(m-1,1))/dt; %*pixmm/dt;
            vy(:,m)=(trp(m,2)-trp(m-1,2))/dt; %*pixmm/dt;
            magn(:,m)=sqrt(vx(:,m).^2+vy(:,m).^2);

          else

            xp(:,m)=0;
```

```matlab
            end

        end

        xp(:);
        sxp=size(xp(:));
        sxp=sxp(1);

        loc=find(xp(:)~=0);

        if loc~=isempty(loc);%

            vecdat(:,1) = xp(:,loc); %xp(:,loc)*(pixmm/1000);
            vecdat(:,2) = yp(:,loc); %(y-yp(:,loc))*(pixmm/1000);
            vecdat(:,3) = vx(:,loc);
            vecdat(:,4) = vy(:,loc);
            vecdat(:,5) = magn(:,loc);


%           vecscale=0.5;
%           figure('Color',[1 1 1]),
%           quiver(vecdat(:,1),vecdat(:,2),vecdat(:,3),vecdat(:,4),vecscale);
%           xlabel({'x (mm)'});
%           ylabel({'y (mm)'});
%           axis([0 1968 0 1998]);

            k=k+1;

            if k==1

                addvec=vecdat;

            else

                addvec=vertcat(addvec,vecdat);%

            end


        else

            flag=2;
            disp('Warning: Particle Tracking was not possible');
            %dlmwrite('20171201_case01_no_tracking_possible.txt',selectedFiles{i},'-
append','delimiter','\t');
%           delete(selectedFiles{i},selectedFiles{i+1});

        end

    else

        flag=2;
```

```matlab
        disp('Warning: Particle Tracking was not possible');
        %            dlmwrite('20171201_case01_no_tracking_possible.txt',selectedFiles{i},'-
append','delimiter','\t');
%          delete(selectedFiles{i},selectedFiles{i+1});
        %
    end

    if flag~=2;
        dlmwrite('20171201_aerolensCapExit_20mbar.txt',addvec,'\t');
    end

else

    clear xyzsA xyzsB
    disp('Warning: Particles were not found');

    delete(selectedFiles{i},selectedFiles{i+1});        %Delete  images  that  don't  contain
particles


end

  clear trp sztrp vx vy magn xp yp sxp loc vecdat

  clear imageA imageB imgA imgB

end
```

loadpoints_0mm.m


```matlab
clear all
close all


[filename, pathname] = uigetfile( ...
   {'*.txt', 'All Text-Files (*.txt)'; ...
     '*.*','All Files (*.*)'}, ...
   'Select Dimilimted Text File to Load');
if isequal([filename,pathname],[0,0])
   return
else
   File = fullfile(pathname,filename);
   vecdat=dlmread(File);

end


pixmm=8.2616;   %this is the ratio between pixels and mm.
yt=2048*pixmm/1000;
xc=1900*pixmm/1000;    %When investigating further downstream e.g. at 63mm, sum here
+63.
yc=1900*pixmm/1000;
y0=(1024-50)*pixmm./1000;   %The jet's axis can be from here calibrated to the capillary's
centre.
% y0=512*pixmm./1000;
   vecdat(:,1)=-(vecdat(:,1)*pixmm/1000);
   vecdat(:,2)=((vecdat(:,2))*pixmm/1000);
   vecdat(:,3)=-vecdat(:,3)*pixmm;
   vecdat(:,4)=-vecdat(:,4)*pixmm;
   vecdat(:,5)=vecdat(:,5)*pixmm;
   maxvec=min(vecdat(:,1));

   vecdat(:,1)=vecdat(:,1)+xc;            %-disp_pixels+cutpix;
%    vecdat(:,2)=y0-(yc-vecdat(:,2));
vecdat(:,2)=y0-vecdat(:,2)-0.2+0.7;


figure('Color',[1 1 1]),
quiver(vecdat(:,1),vecdat(:,2),vecdat(:,3),vecdat(:,4));
%legend(num2str(vec_magn));
xlabel({'x (mm)'});
ylabel({'y (mm)'});


   [filename, pathname] = uiputfile( ...
     {'*.txt';'*.*'}, ...
     'Save as');
   % If 'Cancel' was selected then return
   if isequal([filename,pathname],[0,0])
```

```matlab
    return
else
    % Construct the full path and save
    filename=[filename];
    File = fullfile(pathname,filename);
    dlmwrite(File,vecdat(:,:),'\t');

end
```

display_coloured_vectors.m

```matlab
clear all
close all

[filename, pathname] = uigetfile( ...
   {'*.txt', 'All Text-Files (*.txt)'; ...
      '*.*','All Files (*.*)'}, ...
   'Select Dimilimted Text File to Load');
if isequal([filename,pathname],[0,0])
   return
else
   File = fullfile(pathname,filename);
   vecdat=dlmread(File);

end

s=size(vecdat);
n=s(1);


%%%%%%%%%%%%%%%%%%%%%%%%%%%%%%%%%%%%%%%%%%%%%%%%%%
%%%

for i=1:size(vecdat)

if abs(vecdat(i,5))>0 & abs(vecdat(i,5))<30

   vecdat1(i,1)=vecdat(i,1);
   vecdat1(i,2)=vecdat(i,2);
   vecdat1(i,3)=vecdat(i,3);
   vecdat1(i,4)=vecdat(i,4);
   vecdat1(i,5)=vecdat(i,5);

else

   vecdat1(i,1)=0;
   vecdat1(i,2)=0;
   vecdat1(i,3)=0;
   vecdat1(i,4)=0;
   vecdat1(i,5)=0;

end

end

   x1=vecdat1(:,1);
   y1=vecdat1(:,2);
   v1=vecdat1(:,3);
   u1=vecdat1(:,4);
   magn1= vecdat1(:,5);
```

114

```matlab
  nonzero1=find(v1~=0);

  x1=vecdat1(nonzero1,1);
  y1=vecdat1(nonzero1,2);
  v1=vecdat1(nonzero1,3);
  u1=vecdat1(nonzero1,4);
  magn1=vecdat1(nonzero1,5);
%%%%%%%%%%%%%%%%%%%%%%%%%%%%%%%%%%%%%%%%%%%%%%%%
%%%


for i=1:size(vecdat)

if abs(vecdat(i,5))>30 & abs(vecdat(i,5))<100

  vecdat2(i,1)=vecdat(i,1);
  vecdat2(i,2)=vecdat(i,2);
  vecdat2(i,3)=vecdat(i,3);
  vecdat2(i,4)=vecdat(i,4);
  vecdat2(i,5)=vecdat(i,5);

else

  vecdat2(i,1)=0;
  vecdat2(i,2)=0;
  vecdat2(i,3)=0;
  vecdat2(i,4)=0;
  vecdat2(i,5)=0;

end

end

  x2=vecdat2(:,1);
  y2=vecdat2(:,2);
  v2=vecdat2(:,3);
  u2=vecdat2(:,4);
  magn2= vecdat2(:,5);

  nonzero2=find(v2~=0);

  x2=vecdat2(nonzero2,1);
  y2=vecdat2(nonzero2,2);
  v2=vecdat2(nonzero2,3);
  u2=vecdat2(nonzero2,4);
  magn2=vecdat2(nonzero2,5);


%%%%%%%%%%%%%%%%%%%%%%%%%%%%%%%%%%%%%%%%%%%%%%%%
%%%

for i=1:size(vecdat)
```

```
if abs(vecdat(i,5))>100 & abs(vecdat(i,5))<200

    vecdat3(i,1)=vecdat(i,1);
    vecdat3(i,2)=vecdat(i,2);
    vecdat3(i,3)=vecdat(i,3);
    vecdat3(i,4)=vecdat(i,4);
    vecdat3(i,5)=vecdat(i,5);

else

    vecdat3(i,1)=0;
    vecdat3(i,2)=0;
    vecdat3(i,3)=0;
    vecdat3(i,4)=0;
    vecdat3(i,5)=0;

end

end

    x3=vecdat3(:,1);
    y3=vecdat3(:,2);
    v3=vecdat3(:,3);
    u3=vecdat3(:,4);
    magn3= vecdat3(:,5);

    nonzero3=find(v3~=0);

    x3=vecdat3(nonzero3,1);
    y3=vecdat3(nonzero3,2);
    v3=vecdat3(nonzero3,3);
    u3=vecdat3(nonzero3,4);
    magn3=vecdat3(nonzero3,5);

%%%%%%%%%%%%%%%%%%%%%%%%%%%%%%%%%%%%%%%%%%%%%%%%
%%%

for i=1:size(vecdat)

if abs(vecdat(i,5))>200 & abs(vecdat(i,5))<260

    vecdat4(i,1)=vecdat(i,1);
    vecdat4(i,2)=vecdat(i,2);
    vecdat4(i,3)=vecdat(i,3);
    vecdat4(i,4)=vecdat(i,4);
    vecdat4(i,5)=vecdat(i,5);

else

    vecdat4(i,1)=0;
    vecdat4(i,2)=0;
```

```matlab
   vecdat4(i,3)=0;
   vecdat4(i,4)=0;
   vecdat4(i,5)=0;

end

end

   x4=vecdat4(:,1);
   y4=vecdat4(:,2);
   v4=vecdat4(:,3);
   u4=vecdat4(:,4);
   magn4= vecdat4(:,5);

   nonzero4=find(v4~=0);

   x4=vecdat4(nonzero4,1);
   y4=vecdat4(nonzero4,2);
   v4=vecdat4(nonzero4,3);
   u4=vecdat4(nonzero4,4);
   magn4=vecdat4(nonzero4,5);

%%%%%%%%%%%%%%%%%%%%%%%%%%%%%%%%%%%%%%%%%%%%%%
%%%

for i=1:size(vecdat)

if abs(vecdat(i,5))>260 & abs(vecdat(i,5))<340

   vecdat5(i,1)=vecdat(i,1);
   vecdat5(i,2)=vecdat(i,2);
   vecdat5(i,3)=vecdat(i,3);
   vecdat5(i,4)=vecdat(i,4);
   vecdat5(i,5)=vecdat(i,5);

else

   vecdat5(i,1)=0;
   vecdat5(i,2)=0;
   vecdat5(i,3)=0;
   vecdat5(i,4)=0;
   vecdat5(i,5)=0;

end

end

   x5=vecdat5(:,1);
   y5=vecdat5(:,2);
   v5=vecdat5(:,3);
   u5=vecdat5(:,4);
   magn5= vecdat5(:,5);
```

```matlab
  nonzero5=find(v5~=0);

  x5=vecdat5(nonzero5,1);
  y5=vecdat5(nonzero5,2);
  v5=vecdat5(nonzero5,3);
  u5=vecdat5(nonzero5,4);
  magn5=vecdat5(nonzero5,5);
```

%%

```matlab
for i=1:size(vecdat)

if abs(vecdat(i,5))>340 & abs(vecdat(i,5))<400

  vecdat6(i,1)=vecdat(i,1);
  vecdat6(i,2)=vecdat(i,2);
  vecdat6(i,3)=vecdat(i,3);
  vecdat6(i,4)=vecdat(i,4);
  vecdat6(i,5)=vecdat(i,5);

else

  vecdat6(i,1)=0;
  vecdat6(i,2)=0;
  vecdat6(i,3)=0;
  vecdat6(i,4)=0;
  vecdat6(i,5)=0;

end

end

  x6=vecdat6(:,1);
  y6=vecdat6(:,2);
  v6=vecdat6(:,3);
  u6=vecdat6(:,4);
  magn6= vecdat6(:,5);

  nonzero6=find(v6~=0);

  x6=vecdat6(nonzero6,1);
  y6=vecdat6(nonzero6,2);
  v6=vecdat6(nonzero6,3);
  u6=vecdat6(nonzero6,4);
  magn6=vecdat6(nonzero6,5);
```

%%

```matlab
for i=1:size(vecdat)

if abs(vecdat(i,5))>400 & abs(vecdat(i,5))<480

    vecdat7(i,1)=vecdat(i,1);
    vecdat7(i,2)=vecdat(i,2);
    vecdat7(i,3)=vecdat(i,3);
    vecdat7(i,4)=vecdat(i,4);
    vecdat7(i,5)=vecdat(i,5);

else

    vecdat7(i,1)=0;
    vecdat7(i,2)=0;
    vecdat7(i,3)=0;
    vecdat7(i,4)=0;
    vecdat7(i,5)=0;

end

end

    x7=vecdat7(:,1);
    y7=vecdat7(:,2);
    v7=vecdat7(:,3);
    u7=vecdat7(:,4);
    magn7= vecdat7(:,5);

    nonzero7=find(v7~=0);

    x7=vecdat7(nonzero7,1);
    y7=vecdat7(nonzero7,2);
    v7=vecdat7(nonzero7,3);
    u7=vecdat7(nonzero7,4);
    magn7=vecdat7(nonzero7,5);


%%%%%%%%%%%%%%%%%%%%%%%%%%%%%%%%%%%%%%%%%%%%%%%%%%%%
%%%

for i=1:size(vecdat)

if abs(vecdat(i,5))>480 & abs(vecdat(i,5))<540

    vecdat8(i,1)=vecdat(i,1);
    vecdat8(i,2)=vecdat(i,2);
    vecdat8(i,3)=vecdat(i,3);
    vecdat8(i,4)=vecdat(i,4);
    vecdat8(i,5)=vecdat(i,5);

else
```

```matlab
    vecdat8(i,1)=0;
    vecdat8(i,2)=0;
    vecdat8(i,3)=0;
    vecdat8(i,4)=0;
    vecdat8(i,5)=0;

end

end

  x8=vecdat8(:,1);
  y8=vecdat8(:,2);
  v8=vecdat8(:,3);
  u8=vecdat8(:,4);
  magn8= vecdat8(:,5);

  nonzero8=find(v8~=0);

  x8=vecdat8(nonzero8,1);
  y8=vecdat8(nonzero8,2);
  v8=vecdat8(nonzero8,3);
  u8=vecdat8(nonzero8,4);
  magn8=vecdat8(nonzero8,5);


%%%%%%%%%%%%%%%%%%%%%%%%%%%%%%%%%%%%%%%%%%%%%%%%
%%

for i=1:size(vecdat)

if abs(vecdat(i,5))>540 & abs(vecdat(i,5))<580

  vecdat9(i,1)=vecdat(i,1);
  vecdat9(i,2)=vecdat(i,2);
  vecdat9(i,3)=vecdat(i,3);
  vecdat9(i,4)=vecdat(i,4);
  vecdat9(i,5)=vecdat(i,5);

else

  vecdat9(i,1)=0;
  vecdat9(i,2)=0;
  vecdat9(i,3)=0;
  vecdat9(i,4)=0;
  vecdat9(i,5)=0;

end

end

  x9=vecdat9(:,1);
  y9=vecdat9(:,2);
```

```matlab
    v9=vecdat9(:,3);
    u9=vecdat9(:,4);
    magn9= vecdat9(:,5);

    nonzero9=find(v9~=0);

    x9=vecdat9(nonzero9,1);
    y9=vecdat9(nonzero9,2);
    v9=vecdat9(nonzero9,3);
    u9=vecdat9(nonzero9,4);
    magn9=vecdat9(nonzero9,5);
%
%
%
%%%%%%%%%%%%%%%%%%%%%%%%%%%%%%%%%%%%%%%%%%%%
%%%
%
%    for i=1:size(vecdat)
%
% if abs(vecdat(i,5))>580 & abs(vecdat(i,5))<620
%
%    vecdat10(i,1)=vecdat(i,1);
%    vecdat10(i,2)=vecdat(i,2);
%    vecdat10(i,3)=vecdat(i,3);
%    vecdat10(i,4)=vecdat(i,4);
%    vecdat10(i,5)=vecdat(i,5);
%
% else
%
%    vecdat10(i,1)=0;
%    vecdat10(i,2)=0;
%    vecdat10(i,3)=0;
%    vecdat10(i,4)=0;
%    vecdat10(i,5)=0;
%
% end
%
% end
%
%    x10=vecdat10(:,1);
%    y10=vecdat10(:,2);
%    v10=vecdat10(:,3);
%    u10=vecdat10(:,4);
%    magn10= vecdat10(:,5);
%
%    nonzero10=find(v10~=0);
%
%    x10=vecdat10(nonzero10,1);
%    y10=vecdat10(nonzero10,2);
%    v10=vecdat10(nonzero10,3);
%    u10=vecdat10(nonzero10,4);
%    magn10=vecdat10(nonzero10,5);
```

```matlab
sqx=[10.0:0.1:10.0+100];
sqy=[2.5:0.1:3.8];


figure1 = figure('Color',[1 1 1]);

% Create axes
axes1 = axes('Parent',figure1,...
    'FontWeight','bold',...
    'FontSize',12,...
    'DataAspectRatio',[1 1 1]);

val=0.5;

hold on

quiver(x1,y1,v1,u1,0.2,'Color',[0 0 1]);

quiver(x2,y2,v2,u2,0.2,'Color',[0.2 0.6 1]);

quiver(x3,y3,v3,u3,0.2,'Color',[0.2 0.8 1]);

quiver(x4,y4,v4,u4,0.3,'Color',[0.2 1 1]);

quiver(x5,y5,v5,u5,1,'Color',[0 1 0]);

quiver(x6,y6,v6,u6,0.6,'Color',[0.6 1 0]);

quiver(x7,y7,v7,u7,0.7,'Color',[1 1 0]);

quiver(x8,y8,v8,u8,0.8,'Color',[1 0.7 0]);

quiver(x9,y9,v9,u9,val,'Color',[1 0 0]);
%
% quiver(x10,y10,v10,u10,val,'Color',[1 0 1]);

% plot(sqx,2.5,'-k');
% plot (10.0,sqy,'-k');
% plot(sqx,3.8,'-k');
% plot(sqx,-2.5,'-k');
% plot(sqx,-3.8,'-k');
% plot (10.0,-sqy,'-k');

axis equal;

% quiver(x8,y8,v8,u8,'Color',[1 0 0],'AutoScaleFactor',8*step);

h=legend('0-30m/s','30-100m/s','100-200m/s', '200-260m/s',...
    '260-340m/s', '340-400m/s','400-480m/s','480-540m/s','540-580m/s' );
  set(h,'Location','NorthWest','Orientation','horizontal');
```

```matlab
xlabel({'x (mm)'});
ylabel({'y (mm)'});

axis([0 20 -8 8]);
set(gca,'XTick',[0:2:20]);
set(gca,'YTick',[-8:1:8]);
hold off

vecdatt=sortrows(vecdat,3);
```

Appendix B

Insight 3G™ Software User Guide.

Configure the Capturing Settings

First, the Sychronizer must be turned on (Figure B.1), the Camera connected and the Laser Power Supplies turned on. Otherwise, an Error Message will be displayed when starting the software.

Figure B.1: Photograph of the Synchronizer, when turned on.

Afterwards, the Insight 3G™ Insight Software can be initialized. When the window is displayed, will be directed to the "Exp Tree" tab by default, where all the runs are presented on the left, trough a TreeView visualization.

When clicking on the "+" icon on any of the runs presented on the TreeView, the contained folders will be displayed. Inside the "Raw Data" the images captured during the experiment can be found.

This is really useful when something in the images needs to be examined, e.g. a specific particle, the noise from the capillary reflection, etc.

To start a new run, click "New Run" on the top left of the window (Figure B.2).
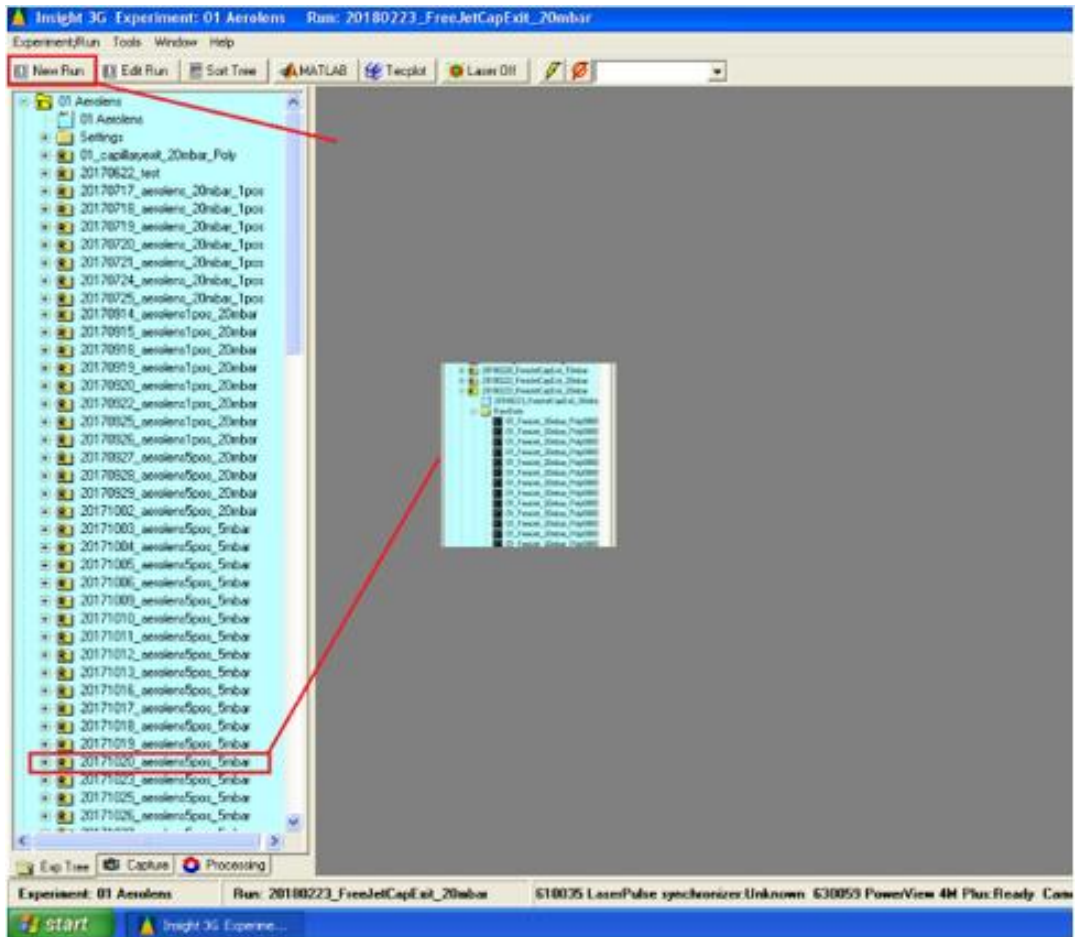
Figure B.2: Main window of the Insight 3G^{TM} software. All the previous runs are displayed on the left side.

When the new run is created, click on the "Capture" tab at the bottom of the window, where the main capturing settings are configured.

From the scroll-down list displayed next to "Capture", three options can be chosen: the Single, the Continuous and the Sequence.

The Continuous mode is very useful, as no images are saved on the disk. This is used when calibrating the laser, setting the camera focus, etc.

The Sequence mode is the one used when running experiments, where images are captured and saved on the hard disk. When Sequence mode is selected, the icon on the right can be clicked and a "Sequence Setup" window will pop up. The "Number of Captures" is the number of pair of images that will be captured at this Capture round. When the number of images is reached, the laser stops. The "Start Number" is the number from which the name of the image will start. For example, if the Number of Captures is 100 and the Start

Number is 23, then the name of the first captured image will be 23 and the name of the last one will be 122.

The laser has 3 power options to select: High, Medium and Low. Even though all of them have default values, the values can be modified through the "Laser Energy Setup" pop-up window, in order to manually change the laser power.
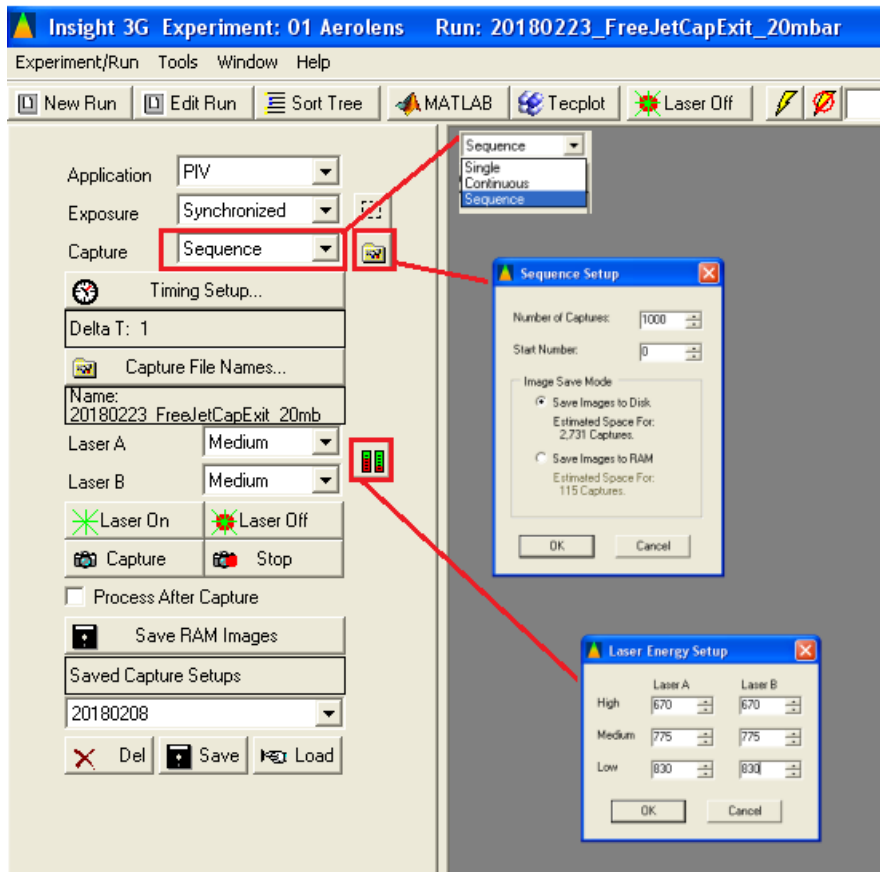

Figure B.3: Configuration of the capturing settings before starting an experiment.

The Timing Setup should be configured as shown in the Figure B.4 below:
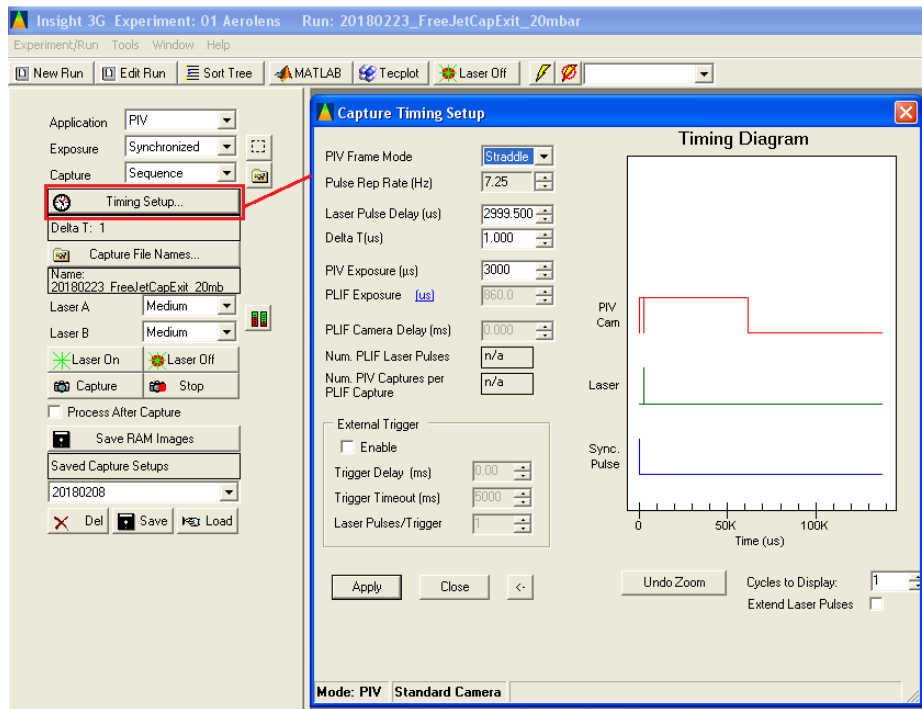
Figure B.4: Configuration of the Timing Setup.

In order to start the laser, first the two start buttons should be pushed on the Remote Controller. The top one starts the Flashlamp and the second the Q-Switch.

Figure B.5: Photograph of the Remote Controller, when the Flashlamp and the Q-switch are both turned on.

When both leds are on, then either the "Laser On" or the "Capture" button on the display should be clicked. The "Laser On" will start the laser, but not the camera, and is mostly used when calibrating the laser. On the other hand, the "Capture" button starts both the Laser and the Camera, and that needs to be clicked in order to capture images.

When the number of images is reached, the laser stops, and both the "Stop" buttons on the remote box should be pushed and the "Laser Off", "Stop" buttons on the display should be clicked.

Image Generator

When a new image needs to be generated, which is a result of many images summed together, as described in section 4.2, first select the images that will be summed, right click, and then select "Open". Then click on the "Analysis" tab.

The software has many tools that can be selected by clicking the "Setup" icon on the "Pre-processing" section. The one for generating the image is the "Image Generator". Through the "Output Setup" button, the name of the generated image can be changed. When ready, click on the "Start" button. The generated image will be saved on the "Analysis" folder of the current Run.
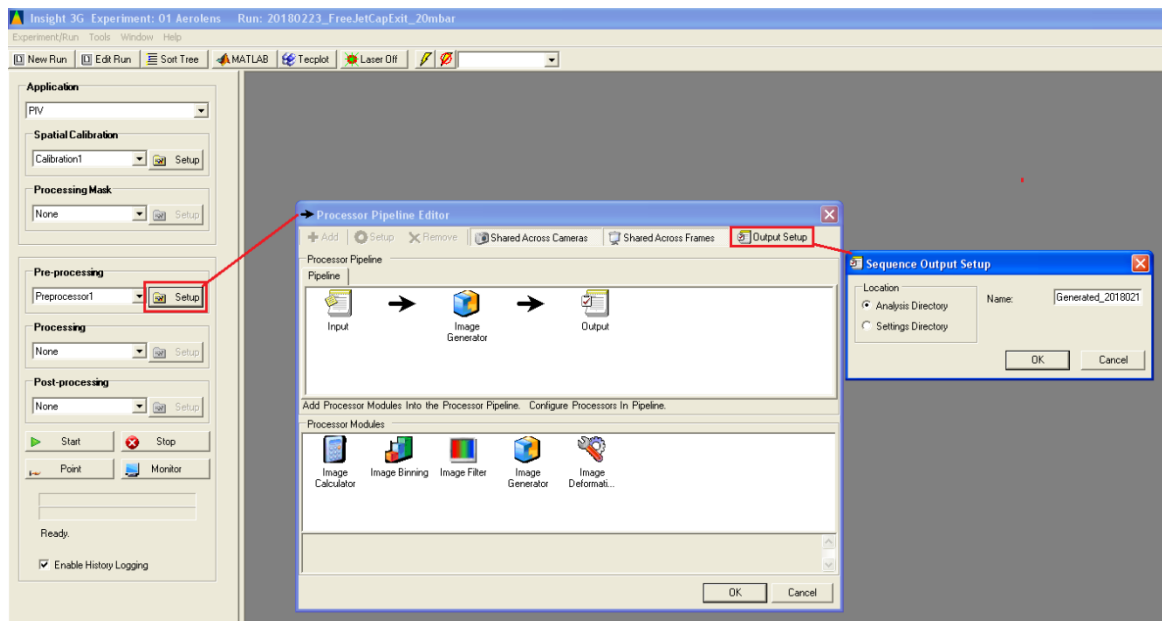

Figure B.6: Procedure for generating a new image using existing ones.

Appendix C

Instructions for using the DMA and CPC.

Introduction to the Hardware

The Electrostatic Classifier used to configure the parameters of the Differential Mobility Analyzer (DMA) is presented in the Figure C.1 below.
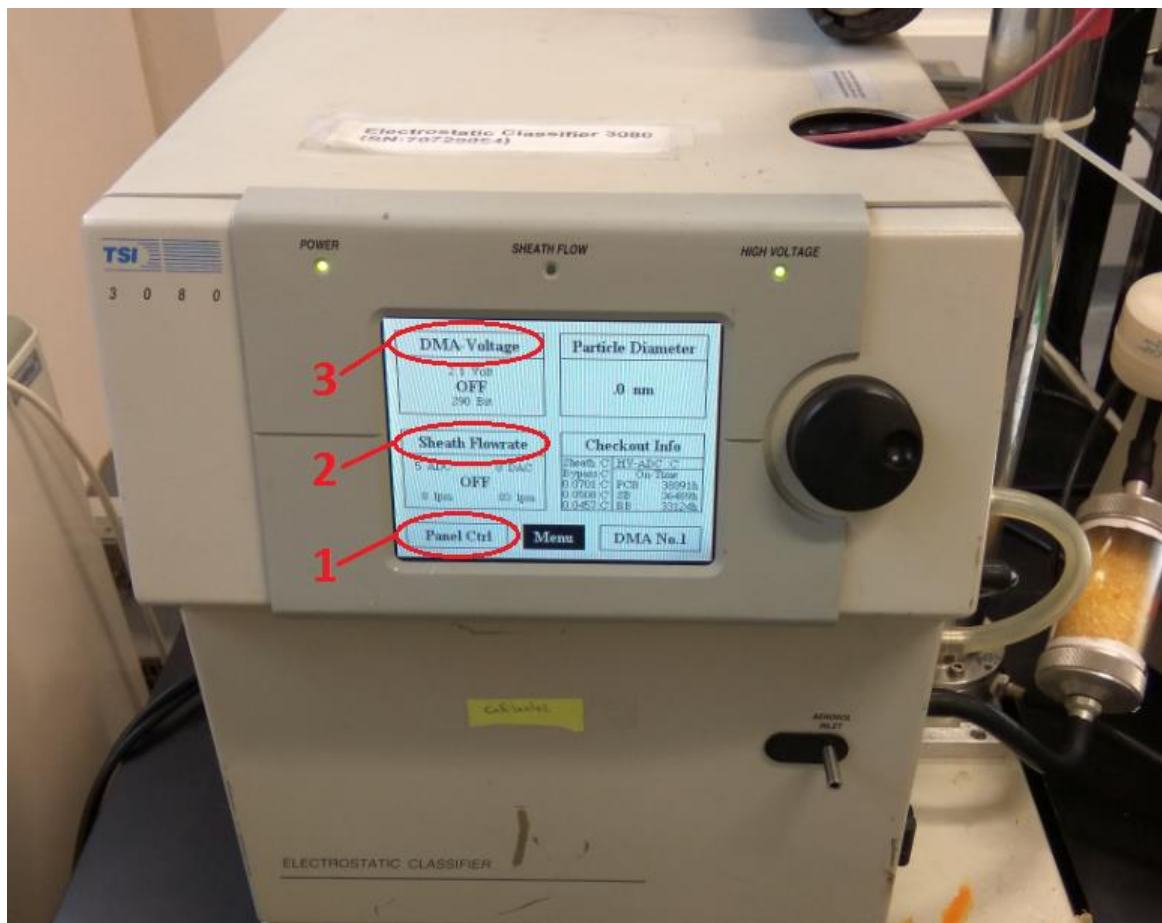

Figure C.1: Photograph of the Differential Mobility Analyzer. The main parameters for configuration (Panel Ctrl, Sheath Flowrate, DMA Voltage) are shown.

1) Two modes are available: the "Analog Ctrl" and the "Panel Ctrl". In the "Analog Ctrl" mode, the DMA receives commands from the CPC and the DMA Voltage is set automatically. This is the mode for investigating size distributions and particle

concentration of the spark source. In the "Panel Ctrl" mode, the DMA voltage should be set to a specific value. This is the mode to select the particle size in the exit of the DMA.

2) The Sheath Flowrate goes from 0 to 15 lpm. When the flowrate is reached, the led in the middle ("SHEATH FLOW") will be green. If 15 lpm cannot be reached, set to 14.5 lpm.

3) The DMA Voltage should be set to a specific value when the DMA works on "Panel Ctrl" mode. Starts from 10 V and thus particles sizes that need smaller voltage value cannot be selected.

Turning off procedure: Set DMA Voltage and Sheath Flowrate to OFF before turning off the device.

The Condensation Particle Counter (CPC) is presented on the following Figure C.2.
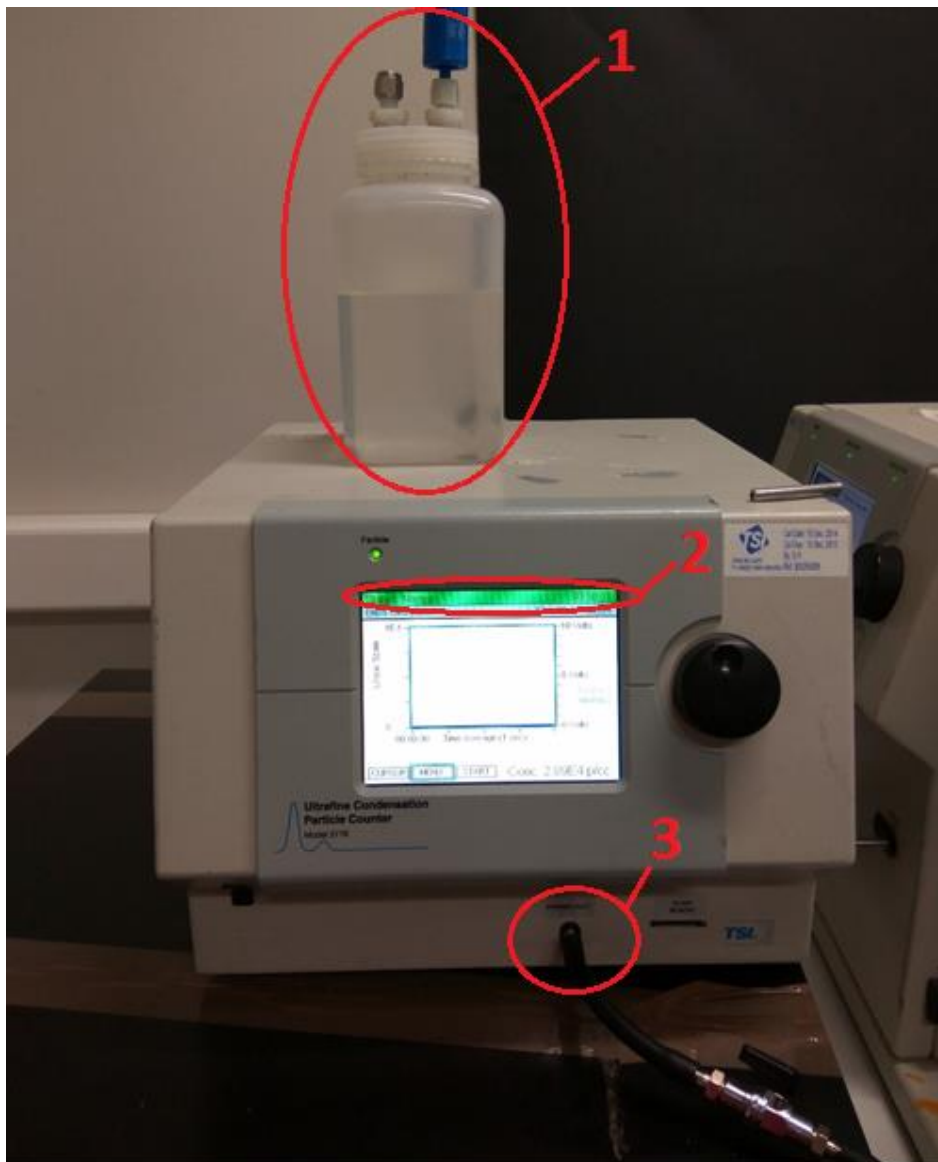

Figure C.2: Photograph of the Condensation Particle Counter (CPC).

1) The Butanol should be placed higher than the CPC device.
2) When is green, the device is ready to use.
3) This is the inlet of the CPC.

   WARNING!

   The inlet flow of the CPC should **never** be less than the flow that it is supposed to get. For example, if it is set on the 1.5 lpm mode, then inlet flow should be at least 1.5 lpm.

Turning on/off procedure: Turn **on** the flow to CPC **BEFORE** turning on the CPC. Turn **off** the flow to CPC **AFTER** turning off the CPC.

Laptop is used only when DMA works on "Analog Ctrl" mode. The "Aerosol Instrument Manager" software is used.
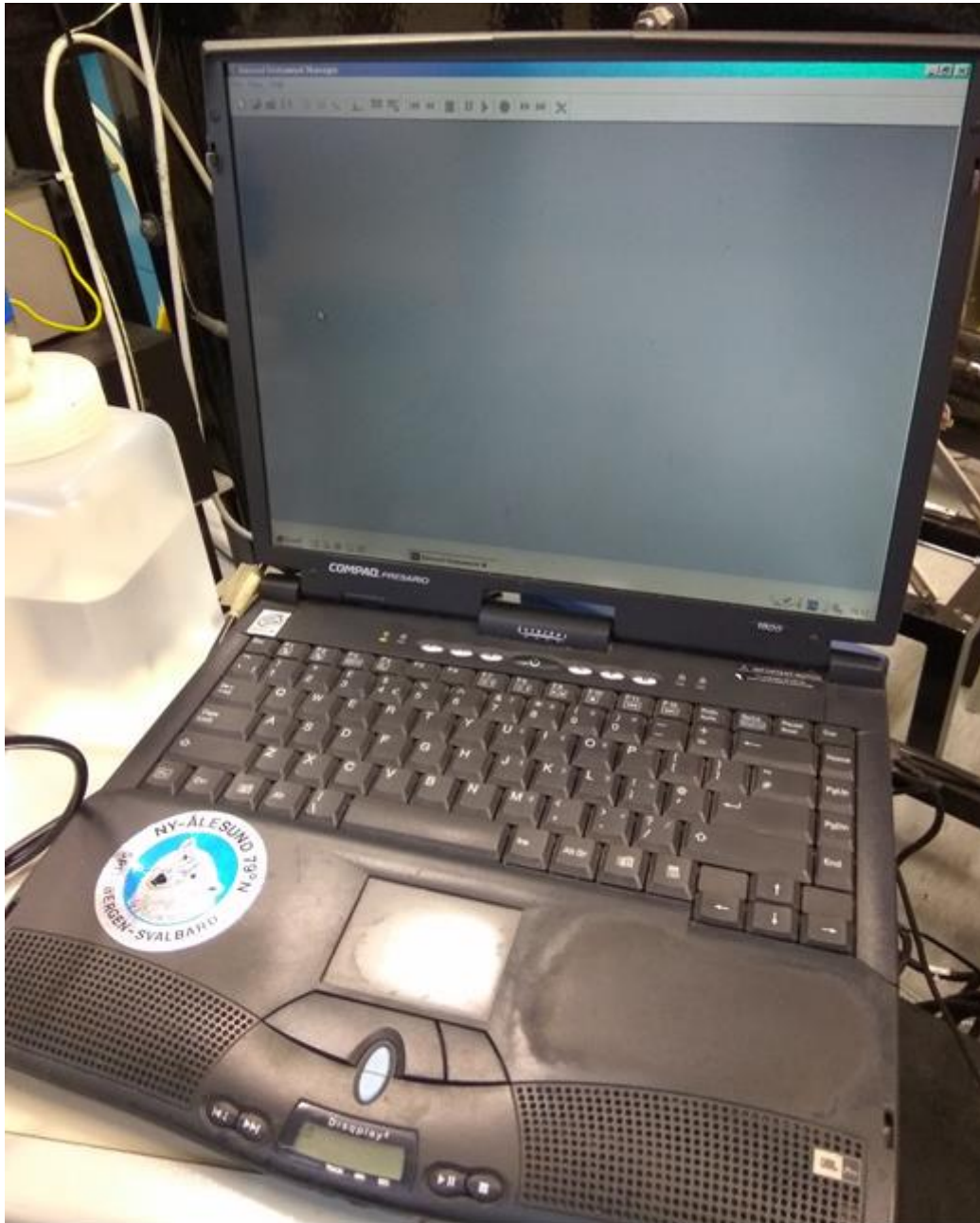

Figure C.3: Photograph of the laptop used for the collection of the particle size distribution.

"Analog Ctrl" mode

Configure the DMA:

First of all the DMA should be set on the "Analog Ctrl" mode.

Typically, the Sheath Flow is 10 or 5 times the CPC flow e.g. if the 0.3 mode is chosen in the CPC, then the flow is set to 3.0 lpm. Thus, the value of the Sheath Flow can be selected according to the needs of the experiment, but it is important to remember to change the default values in the software as well.

The exit of the DMA should be connected to the CPC inlet. A filter must be used to ensure that the flow in the CPC is always adequate.

Configure the CPC:

First of all navigate by turning the shaft to the "Inlet Flow Mode". By pushing the shaft, choose one of the two modes available: the 0.3 mode and the 1.5 mode.

When the Sheath Flow is lowered, the minimum particle diameter that can be detected gets higher (it will be shown on the laptop when setting the properties). That's why the 0.3 mode has the disadvantage that it can measure particles with minimum diameter 13 nm. The appropriate CPC flow/Sheath flow ratio can be chosen according to the needs. For example, the CPC flow can be set at 1.5 lpm and the Sheath Flow at 7.5 lpm without any problem, but at 1.5 lpm the particle concentration could be too high for the CPC to be measured correctly.

If the particle concentrations are high, there is a great chance that the CPC will output an error warning. This is the main reason that an additional chamber was used to dilute the particle concentrations. Knowing that the capillary flow is ~1lpm, 10 lpm were also used in the additional chamber, in order to achieve a 1/10 dilution.

Configure the Laptop:

Hardware Settings:

1) In the "CPC Model and Flow Rate" tab, the "3776 low" is chosen for the 0.3 mode and the "3776 high" for the 1.5 mode.
2) In the "DMA Flow Rate (lpm)" tab, the ratio between the "Sheath" and "Aerosol" should be 10/1 in order to achieve a "strict" size selection from the DMA e.g. 10 nm ± 2 nm. If the Sheath Flow is lower e.g. 7 lpm, then the distribution will be broader and the number concentrations higher. The "Sheath" is the Sheath Flow that is set on the DMA and here 14.5 lpm was chosen, because the CPC had difficulty reaching the 15 lpm. The "Aerosol" is the flow that can be pumped through the capillary, which is ~1 lpm.

3) The "Size Range Bounds" (Diameter) is where the drawback of the 0.3 mode was shown (that the minimum detectable particle diameter is 13 nm) after clicking the "Set to Max Range" button.
4) The Scan Time is how much time will be needed for a full scan. Set it to 3'.
5) The "Length", "Inner Radius" and "Outer Radius" should be set as shown in the following image.
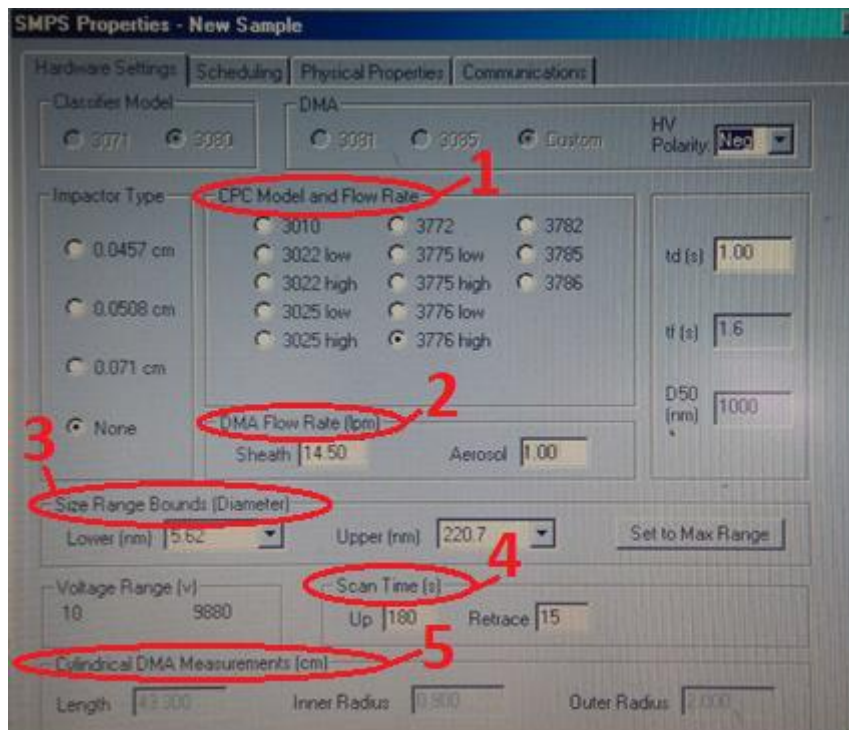
Figure C.4: Configuration of the Hardware Settings of the "Aerosol Instrument Manager" software.

Scheduling:

The scheduling time is set to 5 min, which means that it will take a new sample every 5 minutes.
In the Hardware Settings the Scan Time was set to 3 minutes, which means that 2 minutes remain before going to the next sample. This remained time is used by the CPC to "clean" itself.
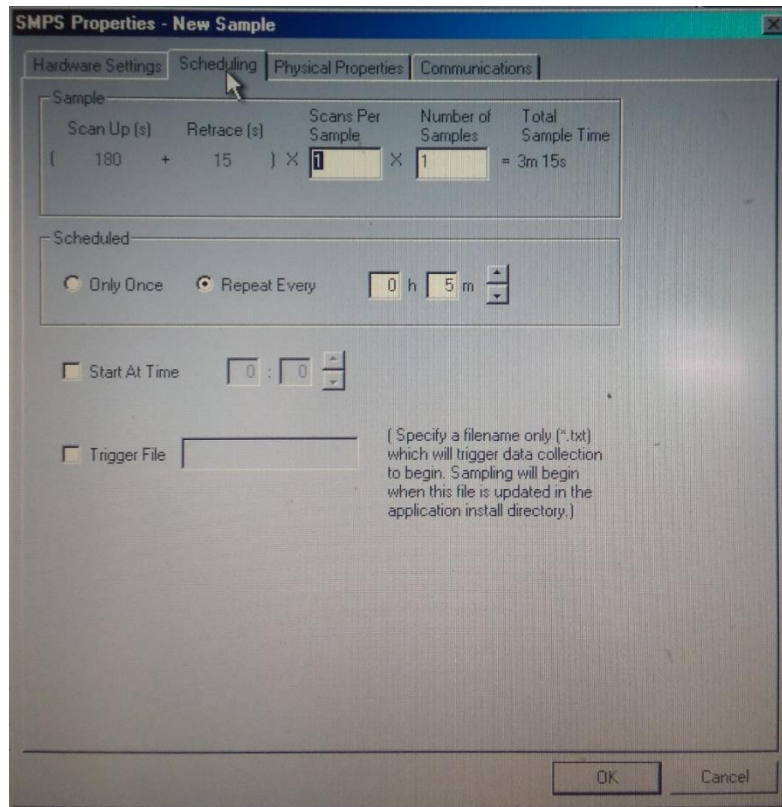
Figure C.5: Configuration of the Scheduling parameters of the "Aerosol Instrument Manager" software.

Physical properties:
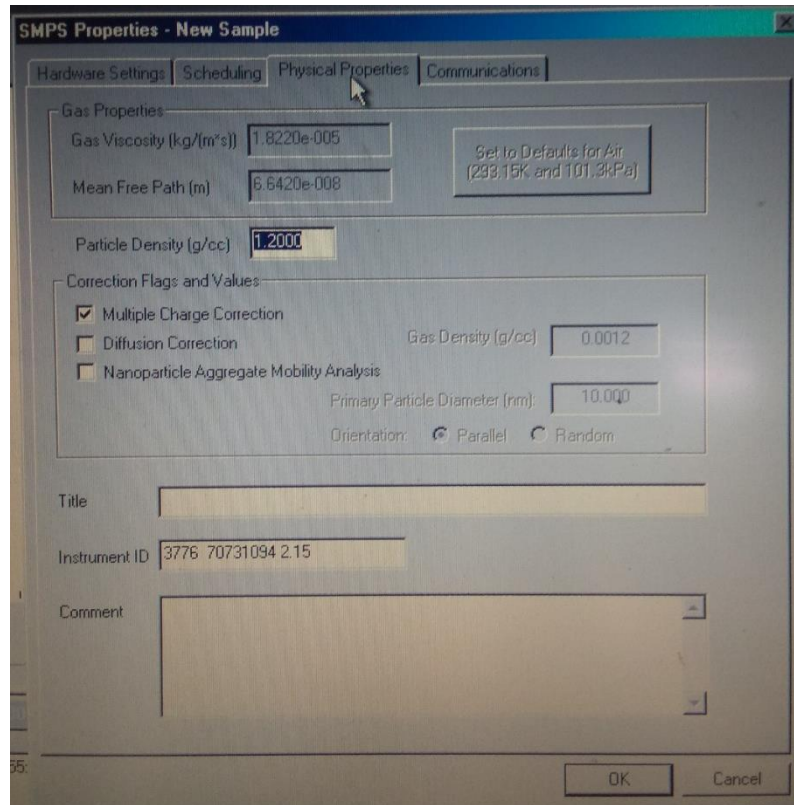
Figure C.6: Configuration of the Physical Properties parameters of the "Aerosol Instrument Manager" software.

Communications:
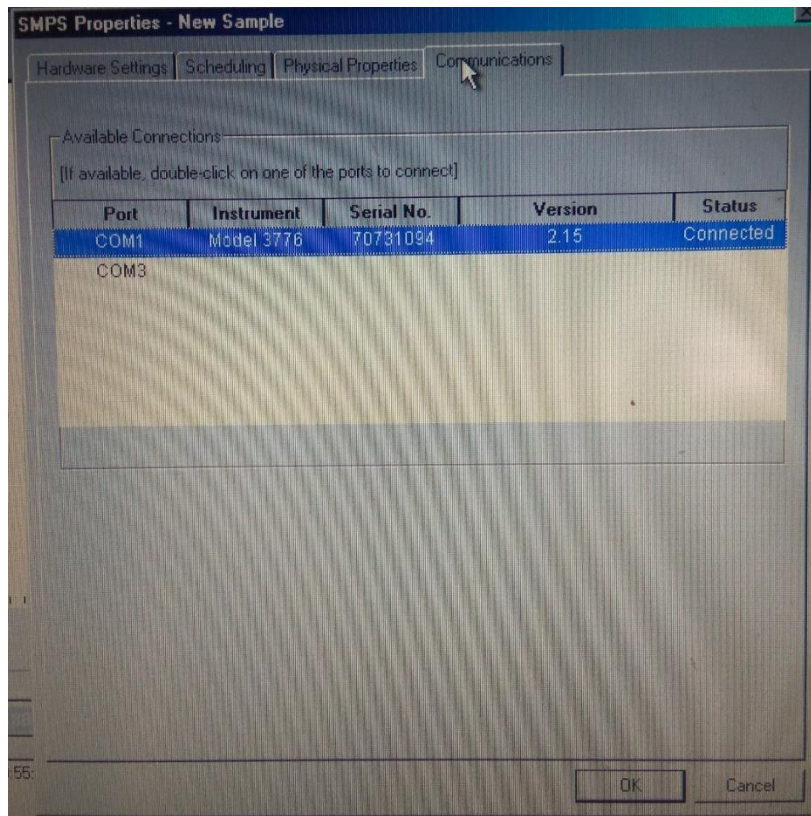
Figure C.7: Configuration of the Communication parameters of the "Aerosol Instrument Manager" software.

"Panel Ctrl" mode

Configuring the DMA:

First of all the DMA should be set on the "Panel Ctrl" mode.

Typically, the Sheath Flow is 10 or 5 times the flow that is pumped through the capillary. The latter will give broader distribution and higher concentration and thus more particles will enter the vacuum chamber. Thus, the value of the Sheath Flow can be selected according to the needs of the experiment.

The DMA Voltage should be set to a specific value, which corresponds to a specific particle size. The voltage can be found through the "Aerosol Instrument Manager" and how this is achieved will be explained below.

The exit of the DMA can be either connected to the capillary and continue run the PIV experiments or to the inlet of the CPC and thus check the concentration of the particles of this specific size.

Find the voltage value for a specific particle size:

Three things are vital for the determination of the voltage that the DMA should be set:

- The Sheath Flow that the DMA will have during the experiments.

- The Flow that is pumped through the capillary (Aerosol).

- The desirable particle size for the PIV experiments.

Caution! If any of these values change, the voltage should be recalculated!

Open the "Aerosol Instrument Manager" and go to Hardware Settings. Input everything like would do in the "Analog Ctrl" mode and the appropriate Sheath Flow and Aerosol Values.

Change the Lower and Upper values to the desirable size and the corresponding voltage value will be shown below at the "Voltage Range" as shown below.

1) Set manually the desirable particle size e.g. 9.8 – 10.2 nm.
2) The voltage value that the DMA should be set, is shown here.

For example, for a Sheath Flow = 10 lpm and Aerosol = 1 lpm, the voltages for 10 nm and 50 nm would be:

(9.31-10nm)   ->   20-23V (mean = 21.5V)

(48.7-50nm)   ->   494-528V (mean = 511V)

Caution! If the voltage value = "<10", that means that this particle size cannot be selected, because DMA voltage cannot go lower than 10V.
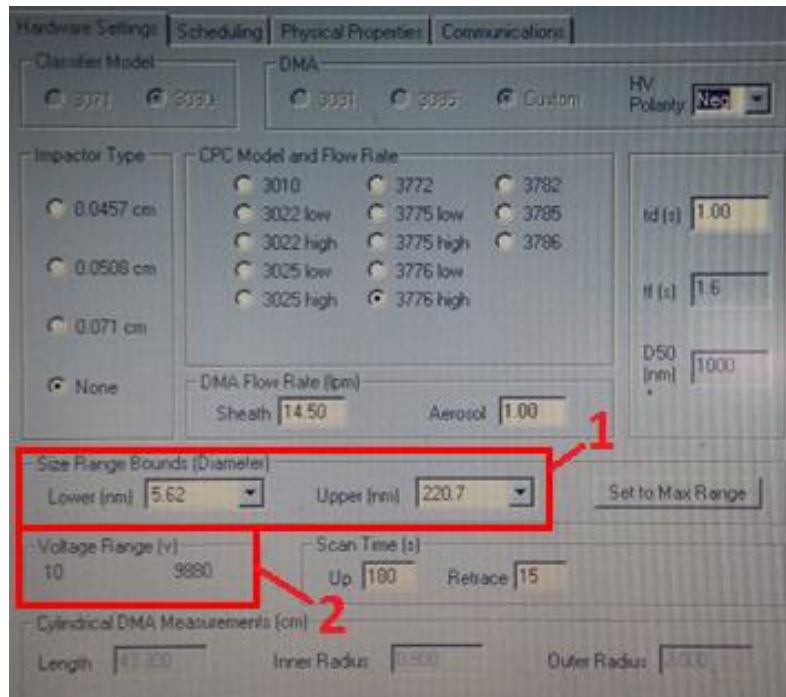
Figure C.8: Procedure for finding the appropriate voltage value to set the DMA for a desired particle size.

For example, in the following tables is presented the voltage at which the DMA should be set for a sheath flow rate of 10 lpm and 5 lpm respectively.

Table 3: The voltage values for 10 nm, 50 nm and 100 nm particle size respectively, when running on a 10 lpm sheath flow rate.

Particle size (nm)	Voltage (V)
10	21.5
50	511
100	1773.5

Table 4: The voltage values for 10 nm, 50 nm and 100 nm particle size respectively, when running on a 5 lpm sheath flow rate.

Particle size (nm)	Voltage (V)
10	10.5
50	255.5
100	886.5